MODELING AND EXPERIMENTAL DESIGN OF NOVEL GAS PURIFICATION AND SEPARATION SYSTEMS

A Dissertation

by

ELVA LORENA LUGO ROMERO

Submitted to the Office of Graduate and Professional Studies of
Texas A&M University
in partial fulfillment of the requirements for the degree of

DOCTOR OF PHILOSOPHY

Chair of Committee,	Benjamin A. Wilhite
Committee Members,	Andrea Strzelec
	Jodie Lutkenhaus
	Perla Balbuena
Head of Department,	M. Nazmul Karim

May 2016

Major Subject: Chemical Engineering

ABSTRACT

The purpose of this work is to address the current challenges of reaction-assisted gas purification systems and gas separation membranes via segregated structuring of multiple reaction, separation, and/or material functionalities in a single unit. Initial focus is on the challenges faced by packed-bed membrane reactors (PBMR) such as film corrosion and competitive adsorption. Firstly, a novel multifunctional reactor design employing a composite catalytic-permselective membrane is introduced. In this design, a permselective film is integrated with a porous catalytic layer for converting CO and H_2O into CO_2 and H_2 via the water-gas shift reaction. This sequentially structured integration of the catalytic and separation functionalities has proven capable of replacing PBMRs while improving film utilization and enhancing the reaction product yield.

Next, the production of high-purity H_2 via sorption-enhanced reforming process (SERP) is presented. SERPs combine CO_2-adsorption with catalytic reaction in a fixed-bed admixture of adsorbent and catalyst particles. The removal of CO_2 from the bulk fluid enhances H_2 yield, purifies H_2 product, and captures CO_2 for controlled disposal. However, bed-scale dilution of CO_2 partial pressure limits sorption rates, while intraparticle diffusional limitations restrict catalyst utilization. These challenges can be addressed using a multifunctional catalyst design coupling adsorptive and catalytic functionalities at the particle scale to yield synergetic enhancement of reaction and adsorption rates. This work presents a side-by-side comparison of the two leading

multifunctional catalyst designs reported in the literature for SERPs: the core-shell design and the uniform-distributed design.

Finally, attention is given to the characterization of Layer-by-Layer (LbL) polymeric films for gas separation and gas barrier applications. The LbL technique allows the integration of multiple distinct material and/or structural properties to achieve novel membranes with better separation and barrier performance than any of the individual constituent materials. Initially, a highly flexible polymer-clay coating with extremely low H_2 and He permeabilities is presented. This barrier coating would allow size and weight reduction for He/H_2 storage and transportation equipment. Then, an all-polymer film for CO_2/N_2 separation is introduced. The use of membranes to selectively remove CO_2 from mixtures with N_2 is of interest for the application in flue gas rectification.

DEDICATION

To my family

ACKNOWLEDGMENTS

First, I would like to thank my parents and my nanny for all their love and support. This entire journey would not have been possible without them. I would also like to thank my brothers and sister for the love and happiness they bring into my life.

I would also like to thank my graduate advisor, Dr. Benjamin A. Wilhite, for his guidance, support and ultimately for granting me the amazing opportunity of pursuing my Ph.D. under his supervision. It is an honor to be part of his group. I am also grateful to my committee members, Dr. Andrea Strzelec, Dr. Jodie Lutkenhaus, and Dr. Perla Balbuena for their guidance and support throughout the course of this research.

Thanks also go to my friends and colleagues for making my time at Texas A&M University a great experience. I want to extend my gratitude to Dr. Daejin Kim and Dr. Aravind Suresh for providing training and guidance for conducting experiments. I would like to acknowledge Stuart Powell for his help with experiments. I would also like to thank other members of Dr. Wilhite's group for supporting me during the course of my Ph.D.: Dr. Bhanu Kumcharaman, Shalini Damodharan, Haomaio Zhang, Xiahong Cui, Holly Butcher and Srikanth PVK.

I'm also truly thankful to Ms. Towanna Arnold for all her help and patience as the graduate program specialist. Towanna was never too busy to help and always cared about assisting in any way she could.

NOMENCLATURE

â	ratio of membrane surface area to fluid volume, m^{-1}
A_C	cross-sectional area for flow, m^2
A_{mem}	membrane surface area, m^2
B_0	fluid permeability coefficient, m^2
c	molar concentration, mol m^{-3}
C_p	heat capacity, J mol^{-1} K^{-1}
Da	Damköhler number, dimensionless
D_i	gas diffusivity coefficient, m^2 s^{-1}
D_i^{eff}	effective diffusivity of species *i*, m^2 s^{-1}
D_{ij}	binary diffusivity of solute *i* in solvent *j*, m^2 s^{-1}
$D_{i,k}$	Knudsen diffusivity of species *i*, m^2 s^{-1}
D_i^{mix}	molecular diffusivity of species *i*, m^2 s^{-1}
d_p	particle dimeter, m
D_{PL}	product layer diffusivity, m^2 s
E_a	activation energy, J/mol
f	tortuosity factor, dimensionless
F_i	molar flow rate of species *i*, mol s^{-1}
F_{press}	pressure scale-up factor, dimensionless
h_f	heat transfer coefficient at gas-solid interface, W m^{-2} K^{-1}
k_i	effective thermal conductivity of species *i*, W $m^{-1}K^{-1}$

k_f	forward rate constant, mol m^{-3} s^{-1} Pa^{-2}
k_{gs}	mass transfer coefficient at gas-solid interface, m s^{-1}
K_{eq}	reaction equilibrium constant, dimensionless
K_i	adsorption coefficient of species *i* on adsorption sites on membrane surface, dimensionless
k_S	kinetic constant for surface reaction, m^4 $kmol^{-1}$ h^{-1}
L	reactor / membrane system flow length, m
M_i	molecular weight of species *i*, kg mol^{-1}
N_{Ca}	mol per unit volume of adsorbent particle, mol m^{-3}
N_i	molar flux of species *i*, mol m^{-2} s^{-1}
Nu	Nusselt number, dimensionless
P	total pressure, Pa
Pe	Peclet number, dimensionless
p_i	partial pressure of species *i*, Pa
P_i	permeability of species *i*, Barrer or mol m^{-1} s^{-1} Pa^{-1}
Pr	Prandtl number, dimensionless
Q_i	flux of species *i* through the permselective layer, mol m^{-2} s^{-1}
Q_r	heat conductivity flux, J m^{-2} s^{-1}
r_i	reaction rate of species *i*, mol m^{-3} s^{-1}
r_T	heat source term, J m^{-3} s^{-1}
R	universal gas constant, J mol^{-1} K^{-1}
Re	Reynolds number, dimensionless

r_p	catalyst pore diameter, m
Sh	Sherwood number, dimensionless
S_i	gas solubility coefficient, cm^3(STP) cm^{-3} atm^{-1}
$S_{i/j}$	apparent permselectivity of species *i* over species *j*, dimensionless
t	time, s
t_m	membrane film thickness, m
t_{Pd}	palladium permselective film thickness, m
t_{poly}	polymer permselective film thickness, m
t_c	catalyst layer thickness, m
T	temperature, K
u	velocity, m s^{-1}
V_i	molar volume, m^3 mol^{-1}
V_{cat}	catalyst volume, m^3
V_d	downstream volume, m^3
x	axis of diffusion, m
X_c	polymer crystallinity, dimensionless
X_i	fractional conversion of species *i*, dimensionless
x_i	mole fraction of species *i*, dimensionless
z	axis of gas flow, m
Z	molar volume ratio, V_{CaCO3}/V_{CaO}, dimensionless
$\%R_i$	percent of recovery of species *i*, dimensionless

Greek Symbols

$\alpha_{i/j}$	intrinsic permselectivity of species *i* to species *j*, dimensionless
α	adsorbent-to-catalyst volume ratio, dimensionless
β	Prater temperature, dimensionless
δ	average grain diameter, m
ΔH_{rxn}	heat of reaction, J mol^{-1}
Φ	normalized Thiele Modulus, dimensionless
ϕ	volume fraction, dimensionless
ε	porosity of catalytic bed, dimensionless
ϵ	particle porosity, dimensionless
η	effectiveness, dimensionless
μ	geometric factor, dimensionless
μ_i	dynamic viscosity of species *i*, Pa s
ξ	ratio of initial rate of desired permeate through the permselective film to WGS reaction, dimensionless
ρ	density, g m^{-3}
σ_i	Lennard Jones parameter, Å
σ_0	grain surface area per unit particle volume, m^{-1}
τ	particle tortuosity, dimensionless
θ	residence time, s
θ_i	surface coverage factor of species *i*, dimensionless
ν_i	atomic diffusional volume of species *i*, dimensionless

ζ	ratio of desired permeate transport across the permselective film to desired permeate transport across the catalytic layer, dimensionless
Ω	Lennard Jones parameter, dimensionless

Subscripts

CO	carbon monoxide
CO_2	carbon dioxide
DEC	methane decomposition
H_2	hydrogen
H_2O	steam
MSR	methane steam reforming
in	initial/inlet condition
out	effluent/outlet condition
WGS	water-gas shift
0	initial

Superscript

cat	catalyst
CaO	calcium oxide
$CaCO_3$	calcium carbonate
CCP	composite catalytic-permselective membrane
F	feed volume

GPM	gas purification membrane
mix	bulk mixture
PBMR	packed-bed membrane reactor
Pd	palladium film
Poly	polymer film
S	sweep volume
sor	adsorbent

TABLE OF CONTENTS

Page

LIST OF FIGURES

Page

LIST OF TABLES

Page

CHAPTER I

INTRODUCTION

Nonuniform distribution of catalytic functionality in a single unit is a well-established approach to optimize overall process performance by exploiting the interaction between chemical reactions and transport processes [1-3]. In 1983, Verykios [4] showed that higher reactor yield and selectivity, along with improved reactor stability can be achieved by a fixed-bed reactor with nonuniformly distributed catalyst particles. Wei and Becker [5, 6] studied the effect of four different catalyst distributions for bimolecular Langmuir-Hinshelwood kinetics. In three of their designs, the catalyst was segregated in only one-third of the pellet volume: outer, middle, and inner (Figure 1). In the fourth design, the catalyst was uniformly distributed within the pellet. Their findings demonstrated that the outer distribution was favored for large Thiele Modulus[1] (Φ) values (diffusion control regime) while the inner distribution was best for small Thiele Modulus values (kinetic control regime). For intermediate values of the Thiele Modulus, the middle distribution had the best performance. More recently, Dietrich et al. [7] studied the effects of functionality distribution for a bifunctional catalyst for two test systems: the Claus process and the water-gas shift reaction. Seven different cases were considered; starting with the highest degree of integration (a uniform mixture of adsorbent and catalyst) and then volume fractions were gradually segregated until core-shell designs were obtained (Figure 2). Their results showed that multifunctional catalysts can be used to eliminate

[1] The Thiele Modulus is a dimensionless group that represents the ratio of reaction rate to diffusion rate.

mass transfer limitations and improve the utilization of particle's functionalities. Additionally, in a structured multifunctional pellet unused catalyst can be replaced by adsorbent material to increase adsorption capacity. In the case of negligible mass transfer limitations between the different functionalities, the benefits of using multifunctional catalysts must be evaluated to justify the more difficult fabrication procedures [7].

Most of the work dealing with nonuniform catalysts consists of theoretical studies, although some experimental studies have recently appeared [8-11]. Most of the experimental investigations have looked into efficient ways of manufacturing these nonuniform catalysts by use of controlled impregnation techniques [1]. However, these studies have been limited to patterning a single functionality as opposed to patterning multiple functionalities in a single particle.

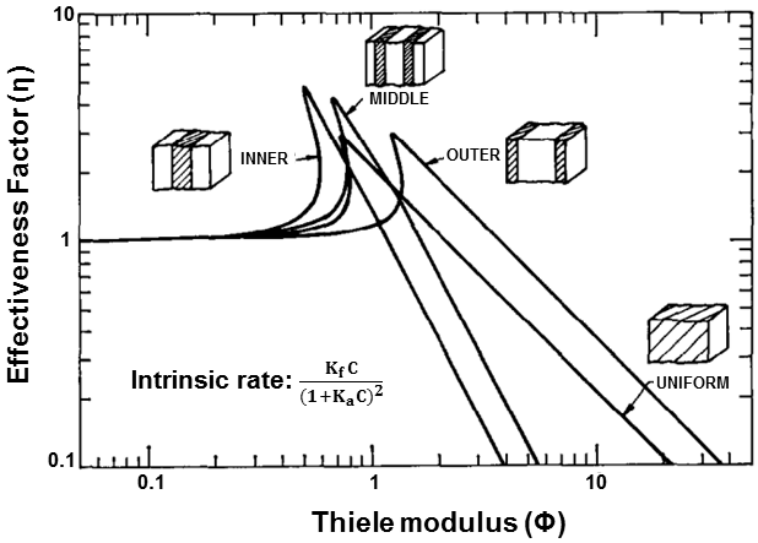

Figure 1. Isothermal effectiveness factor (η) for bimolecular Langmuir-Hinshelwood kinetics in nonuniformly distributed flat plate catalyst (K_aC=20) [5].

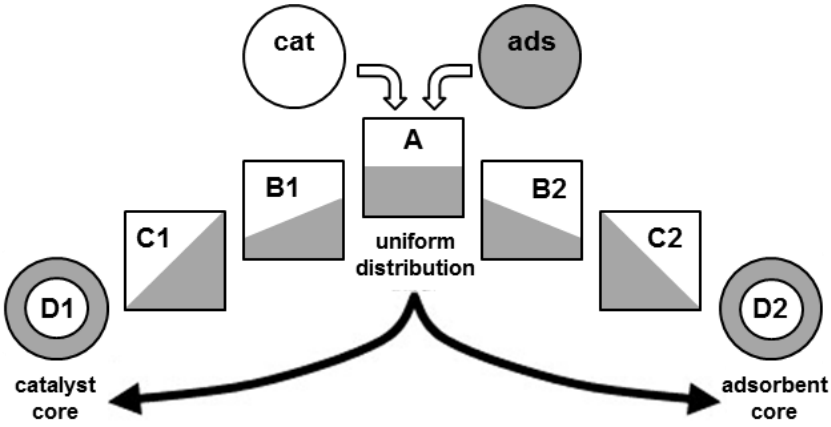

Figure 2. Structure variants considered in the optimization of particle's catalyst distribution [7].

This work's central hypothesis is that sequentially structured patterning of multiple distinct reaction and separation functionalities in a single unit (e.g., membrane, catalyst, etc.) may be used to manipulate local driving forces for product removal to significantly enhance both catalyst utilization and product removal rate. This hypothesis is tested for applications related to hydrogen (H_2) production, as this gas has emerged as a promising emission-free energy carrier. In addition, hydrogen is an important feedstock for the manufacture of key commodity chemicals, such as ammonia and methanol [12, 13]. The hypothesis is demonstrated in two different systems: 1) a composite catalytic-permselective membrane for water-gas shift reaction coupled with hydrogen or carbon dioxide (CO_2) removal (Chapter II) and 2) a multifunctional catalyst for sorption-enhanced water-gas shift and sorption-enhanced methane steam reforming (Chapter III).

Chapter IV and V extend this hypothesis to polymeric membrane designs integrating multiple distinct material and/or structural properties via the Layer-by-Layer (LbL) technique to achieve novel gas separation and gas barrier membranes with better

separation and barrier performance than any of the individual constituent materials. Using the LbL technique, thin film structure can be finely tuned to allow certain gases to permeate more easily, creating a gas separation film. Additionally, this technique also allows the elongation of the gas diffusion pathway and the formation of strong interactions between the polymer film constituents, which results in a reduction in gas permeability, and, therefore, an improvement in gas barrier properties. This work focuses on separation and barrier applications of interest for the development of a hydrogen-based energy industry. Chapter IV presents the experimental investigation of Helium (He) and hydrogen barrier coatings that would allow size and weight reduction for He/H_2 storage and transportation equipment. Additionally, these barrier coatings would allow the extension of process equipment lifetime by reducing the risk of equipment failure owing to H_2 embrittlement. Chapter V investigates the performance of a LbL thin film for CO_2 separation from gaseous mixtures. CO_2-permselective films could be employed to selectively remove CO_2 from reformate mixture, removing in this way equilibrium limitations of hydrogen-production reactions. Additionally, CO_2-permselective membranes are of interest for the application in flue gas rectification and natural gas purification.

1.1 WHY HYDROGEN?

Hydrogen is an important commodity chemical in the petrochemical and petroleum refining industries [12, 13]. In addition to its industrial uses, hydrogen has gathered considerable attention as a possible energy alternative to relieve environmental problems arising from the use of fossil fuels [14, 15]. Hydrogen can be converted to electrical power

via H_2-driven fuel cells, a leading candidate for next-generation power systems [16, 17]. Hydrogen is a colorless, odorless, non-toxic, and highly flammable gas. It is the most abundant element in the universe, constituting roughly 75% of its mass [18]. However, hydrogen gas is never found by itself; it is only available in a bonded form and must be liberated from other compounds such as hydrocarbons, water, or biomass [19, 20]. Hydrogen extraction from hydrocarbon fuels is the most common method for hydrogen production today. This method requires multiple chemical processes such as hydrocarbon reforming and hydrogen purification, which results in significant system volume and weight. Therefore, the challenge remains to develop integrated systems capable of extracting pure hydrogen from hydrocarbon sources in a compact and efficient process.

1.2 INDUSTRIAL USES OF HYDROGEN

Hydrogen is a key commodity material used in several industries. It is the fundamental building block for the manufacture of two of the most important chemical products made industrially, ammonia (NH_3) and methanol (CH_3OH). Hydrogen is also crucial for the petroleum refining industry and the electronics and metallurgical industries. Figure 3 presents a breakdown of global hydrogen consumption by industry.

Globally, more than 50 million metric tons of hydrogen are produced every year [21] and approximately 10-11 million metric tons are produced in the U.S. [22]. The ammonia production industry consumes approximately 54% of all the hydrogen produced in the world [23]. The petroleum refining and chemical industry accounts for approximately 35% of global hydrogen consumption [13, 19] while the metallurgical, food

and electronics industries account for the remaining 11%. A brief introduction to the hydrogen usage and requirements by each industry is presented below.

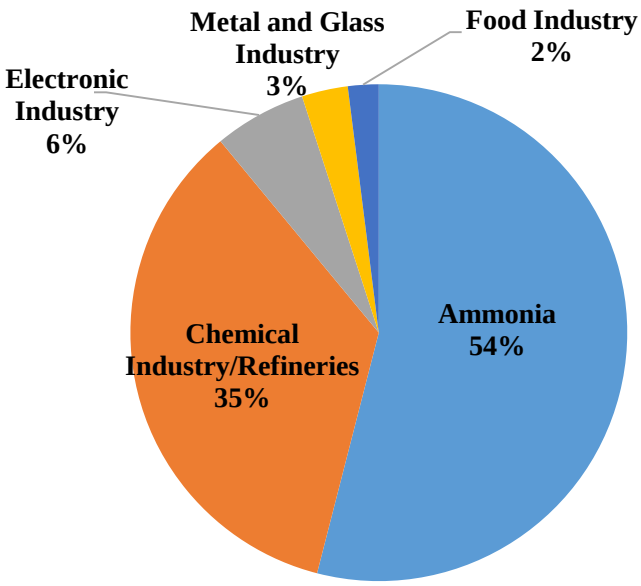

Figure 3. Global hydrogen consumption by industry [23].

1.2.1 Ammonia Industry

Anhydrous ammonia is a key chemical for the fertilizer industry and is also used in the production of munition [24] and fine chemical products. The manufacture of nitrogen-containing fertilizers is by far the most important use of ammonia, using approximately 86% of the ammonia produced in the world [25]. Ammonia is produced by reacting nitrogen (N_2) and hydrogen (Equation 1) via the catalytic Haber-Bosch process at pressures of 200 bar to 350 bar and temperatures of 300 °C to 500 °C [26]. This reaction is exothermic and, therefore, a cooling system is typically installed to control the temperature in the reactor and maintain a reasonable equilibrium constant.

$N_2 + 3H_2 \rightarrow 2\ NH_3 \quad \Delta H_{rxn} = -92.4\ kJ\ mol^{-1}$ (1)

The nitrogen molecule is very unreactive due to a strong triple bond; for this reason, the Haber-Bosch process relies on catalysts that accelerate the cleavage of this bond. The catalysts used are based on iron promoted with K_2O, CaO, or Al_2O_3 [27]. Due to the nature of the catalysts, only very low levels of oxygen-containing compounds, such as carbon dioxide, carbon monoxide (CO), and steam (H_2O), can be tolerated in the feed gas. Therefore, the hydrogen and nitrogen gas streams must be purified before being fed into the process [26].

1.2.2 Petroleum Refining Industry

The increasing demand of hydrogen by the petroleum industry has been driven by growing energy demands and increasing concerns regarding the environmental impact of fuel production. In the refining industry, hydrogen is used for the catalytic upgrading of petroleum distillates to transportation and logistics fuels (hydrocracking) and for the removal of sulfur and nitrogen compounds from sour crudes (hydrotreating) [28, 29].

The hydrocracking process was brought to the U.S. by Esso Research and Engineering Co. in the early 1930s for use in the upgrading of petroleum products and feedstocks [30]. The hydrocracking mechanism is that of catalytic cracking with hydrogenation superimposed. Catalytic cracking is the cleavage of a carbon-carbon single bond while hydrogenation is the addition of hydrogen to a carbon-carbon double bond. In the hydrocracking process, cracking and hydrogenation of heavy hydrocarbons take place simultaneously to produce more valuable products with higher H/C ratios and low boiling points, such as gasoline, diesel, and jet fuel [31, 32]. This process is used for feedstocks

that cannot be processed using conventional catalytic cracking [33] and it can also be used to improve gasoline octane number [31]. The hydrocracking process is typically carried out at temperatures between 290 °C and 400 °C and at pressures between 8,275 kPa and 15,200 kPa. Preparation of the feed stream is important in order to prevent catalyst poisoning and prevent competitive chemisorption of CO on active catalyst sites [30].

In the hydrotreating process, hydrogen is used to hydrogenate sulfur and nitrogen impurities and remove them as hydrogen sulfide (H_2S) and NH_3. Other components such as oxygen, halides, and trace metals can also be removed [30]. The demand for hydrotreating processes is expected to increase due to stricter legislation for sulfur content in fuels and the rising volumes of sour crudes populating the market [28, 29, 34, 35]. Hydrotreating can be applied to a wide range of feedstock including naphtha and reduced crudes. Typical hydrotreating reactions are presented in Table 1.

Hydrotreating reactions are usually carried out at temperatures between 270 °C and 430 °C and pressures between 700 kPa and 20,000 kPa. In this process, the hydrocarbon stream is mixed with a H_2-rich stream and fed into a fixed-bed reactor loaded with a metal-oxide catalyst. In the reactor, hydrogen reacts with impurities to produce either H_2S, NH_3, or free metals [30, 36].

Table 1. Hydrotreating reactions and their chemistries [30].

Reaction	Chemistry
Hydrodesulfurization	$RSH + H_2 \rightarrow RH + H_2S$
	$R_2S + 2H_2 \rightarrow 2RH + H_2S$
	$(RS)_2 + 3H_2 \rightarrow 2RH + 2H_2S$
Hydrodenitrogenation	$R_3N + 3H_2 \rightarrow 3RH + NH_3$
Hydrogedeoxygenation	$R_2O + 2H_2 \rightarrow H_2O + 2RH$
Hydrodemetalation	$RM + 0.5H_2 + A \rightarrow RH + MA$
Hydrodehalogenation	$RX + H_2 \rightarrow RH + HX$

R = alkyl group; M = metal, X = halogen, A = metal attracting material

The most important hydrotreating reactions are hydrodesulfurization and hydrodenitrogenation; however, other reactions can occur simultaneously depending on the operating conditions. The ease of the hydrodesulfurization process will depend on the type of compound, with low-boiling compounds being more easily desulfurized than high-boiling compounds. Hydrodenitrogenation, on the other hand, is a more complicated process that requires more severe conditions. A more detailed review on hydrotreating reactions can be found in the following references [30, 36].

1.2.3 Other Industries

In the metallurgical industry, hydrogen is the used in the Sherritt-Gordon process to convert and precipitate nickel, copper or cobalt from a salt solution. In the reduction stage, hydrogen removes the sulfate present in solution and precipitates the metal [37]. In the electronic industry, hydrogen is employed to reduce silicon tetrachloride ($SiCl_4$) and trichlorosilane ($SiHCl_3$) to silicon (Si) for the growth of epitaxial silicon [13, 38]. Other industrial uses of hydrogen include iron ore processing, oil and fat hydrogenation, and methanol production.

1.3 HYDROGEN AS AN ENERGY CARRIER

Hydrogen has been recognized for its potential as a universal fuel, derivable from both renewable (biomass, water) and non-renewable (petroleum, natural gas, coal) resources [14, 15, 39]. Hydrogen has the highest combustion energy per unit mass relative to any other fuel (see Table 2) [40, 41] and is considered an ideal candidate for locally generating clean, efficient, and sustainable energy. When supplied to a proton-exchange membrane fuel cell (PEMFC), the hydrogen's chemical energy is transformed into electric energy with water being the only emission at the point of use (when reacted with pure O_2).

Table 2. Summary of energy densities of hydrocarbon fuels [41].

Fuels	W h^{-1} kg^{-1}	W h^{-1}
Hydrogen (STP)	39,000	3
Liquid Hydrogen	39,000	2600
Methanol	5,530	4370
Ethanol	7440	5885
Propane	12,870	6320
n-butane	12,700	7280
Iso-octane	12,320	8504
Diesel	12,400	8700
Gasoline	9,700	12,200

Low-temperature PEMFCs are a leading candidate for future power generation systems, due to their portability, high-energy density, and near-ambient operating temperatures (60 ºC - 90 ºC) [42, 43]. PEMFCs are capable of achieving significant improvements in fuel efficiencies compared to existing internal combustion engines, without locally producing any emissions associated with hydrocarbon fuel's combustion (e.g., nitrogen oxides (NO_x), sulfur oxides (SO_x), particulates) [44-46]. The anode

catalysts currently employed in PEMFCs are very susceptible to poisoning by CO (at concentrations > 10 ppm) [44, 47, 48] and, therefore, purification of reformate mixture prior to use in PEMFCs is required.

1.4 HYDROGEN GENERATION

Hydrogen can be produced via methane steam reforming, coal gasification, oil partial oxidation, or water electrolysis. It can also be produced using less efficient technologies such as photobiological processes and solar electrolysis. Currently, the worldwide hydrogen production mostly relies on processes that extract hydrogen from hydrocarbon feedstocks (Figure 4). Approximately 96% of hydrogen production involves the use of fossil fuels, and only about 4% involves the use of renewable resources such as water [49, 50]. A brief description of hydrogen generation through water electrolysis and hydrocarbon reforming is given below.

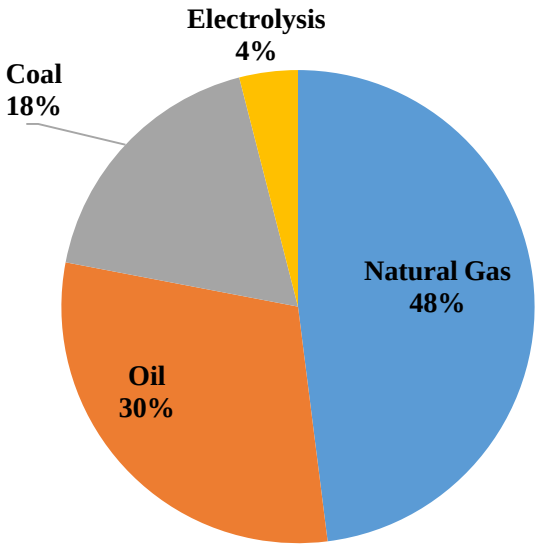

Figure 4. Feedstocks used in the global production of hydrogen [49].

1.4.1 Water Electrolysis

Water electrolysis is an option for the production of hydrogen from renewable resources. The history of water electrolysis started in 1800, when Carlisle and Nicholson discovered the ability of electrolytic water splitting [51]. Water electrolysis is the process in which water is decomposed into hydrogen and oxygen by passing an electric current through it in the presence of electrolytes. This reaction takes place in a system called an electrolyzer which consists of an anode and a cathode separated by a membrane that allows the passage of only ions and electrons (Figure 5) [51-53]. The positively charged hydrogen ions (H^+) migrate to the negatively charged cathode, where a reduction reaction takes place to form hydrogen atoms that then combine into H_2 molecules. The oxygen molecules, on the other hand, are formed at the positively charged anode.

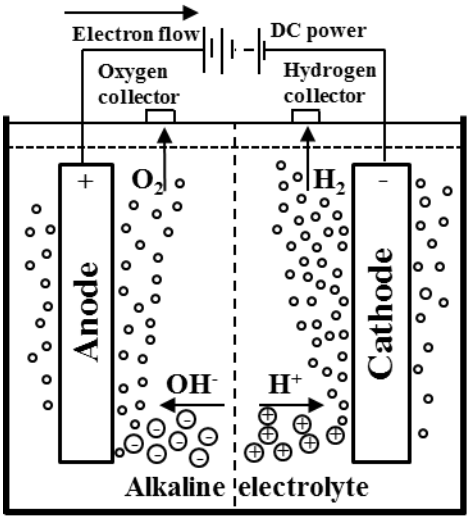

Figure 5. Basic schematic of a water electrolysis system [52].

Water electrolysis is capable of producing large quantities of hydrogen without emitting the undesirable byproducts of hydrocarbon fuel reforming such as CO, CO_2, NO_x,

and SO_x. This process emits CO_2 only when the necessary electricity is generated in power plants that use hydrocarbon fuels [49] though a process using electricity derived from solar or wind energy could eliminate these emissions [54]. Water electrolysis is currently used for only 4% of global hydrogen production due to its excessive energy consumption and relatively large investment [51, 55]. New processes such as high-pressure and high-temperature electrolysis are being investigated for large-scale production to improve process' energy efficiency.

1.4.2 Hydrocarbon Reforming

Steam reforming of hydrocarbons (Equation 2) is one of the most important and frequently used processes of hydrogen production [15, 28, 29, 48, 49]. Today, 90% - 95% of the hydrogen produced in the U.S. comes from the reforming of methane (CH_4) [56]. Methane steam reforming (MSR) (Equation 3) is a highly endothermic catalytic process, as it requires the cleavage of C-H and O-H bonds. The MSR process is carried out in the temperature range of 700 °C - 1,000 °C and at pressures up to 3.5 MPa [49]. There are many catalysts suggested in the literature for this reaction; but the best performing catalysts include Co/ZnO, Rh/Al_2O_3, ZnO, $RhCeO_3$, and Ni/La_2O_3-Al_2O_3 [15].

$$C_nH_m + n\ H_2O \leftrightarrow (n + m/2)\ H_2 + n\ CO \quad (2)$$

$$CH_4 + H_2O \leftrightarrow 3\ H_2 + CO \qquad \Delta H_{rxn} = 206\ kJ\ mol^{-1} \quad (3)$$

$$CO + H_2O \leftrightarrow H_2 + CO_2 \qquad \Delta H_{rxn} = -41\ kJ\ mol^{-1} \quad (4)$$

Methane steam reforming typically produces a reformate mixture containing 70 - 72 mol% H_2, 6 - 8 mol% CH_4, 10 - 14 mol% CO_2, and 8 - 10 mol% CO on a dry basis. Carbon monoxide is a significant poison to several catalytic processes employed in fuel

production; therefore, the reformate mixture needs further purification prior to use. Carbon monoxide may be further reacted with steam via the water-gas shift (WGS) reaction (Equation 4) to increase H_2 yields and reduce CO content.

The WGS is an exothermic equilibrium-limited reaction and, therefore, is kinetically favored at high temperatures and thermodynamically favored at low temperatures. The WGS reaction is normally carried out in a two-stage process. Initially, a high-temperature WGS reactor, operating in the temperature range of 310 °C to 450 °C, is used to take advantage of the high reaction rates. Then, a low-temperature WGS reactor, operating in the temperature range of 200 °C to 250 °C, is employed to remove equilibrium limitations on CO conversion. A copper-based catalyst and an iron-based catalyst are used for the low- and high-temperature stages, respectively [57]. The WGS reaction produces a mixture containing ~2000ppm CO on a dry basis. Further reduction in carbon monoxide content and other impurities in the reformate stream is achieved using H_2 purification technologies capable of producing high-purity H_2 suitable for use in industrial and portable applications [58]. A summary of H_2 purity requirements in various applications is presented in Table 3. A basic schematic of the three-step process (i.e., CH_4 reforming, water-gas shift, and H_2 purification) is presented in Figure 6.

Table 3. Summary of H_2 purity requirements in various applications [59, 60].

Purpose	Hydrogen purity (%)
Semiconductor	99.999999
PE fuel cell	99.99
Hydrodesulfurization	90
Hydrocracking	70-80
Fuel gas	54-60

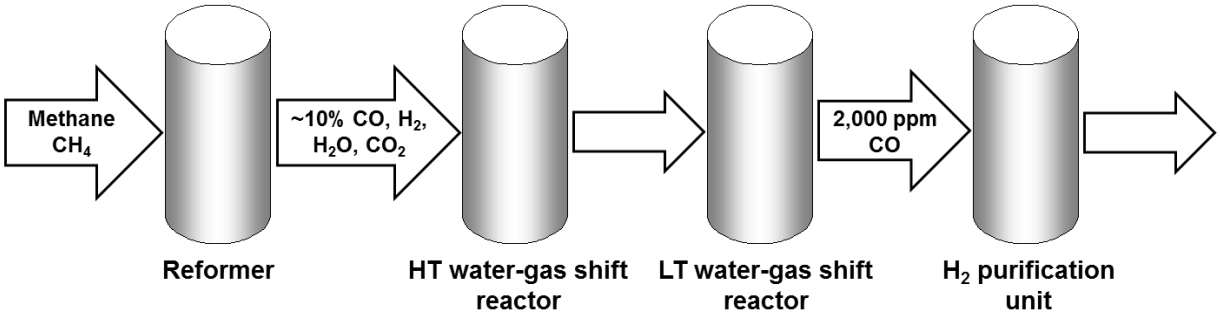

Figure 6. Methane steam reforming and water-gas shift reaction process.

1.5 HYDROGEN SEPARATION

The most common hydrogen purification technologies include pressure swing adsorption (PSA), cryogenic distillation, and membrane separation [61, 62]. PSA is a well-established unsteady-state process capable of producing H_2 to any desired level of purity (up to 99.99%) [63, 64]. In this process, a high-pressure gas stream flows through a column packed with a solid adsorbent that selectively remove some components from the gas mixture. The resulting gas stream is enriched in the gas component that interacts less strongly with the solid adsorbent. Once an adsorbent bed is saturated, it must be taken offline to replace or regenerate the spent adsorbent, and a new bed with fresh adsorbent is put in operation. In the regeneration step, the adsorbed components are desorbed from the adsorbent by lowering pressure inside the column to near-ambient conditions [65]. This process typically requires multiple beds of adsorbent material to ensure continuous operation. A schematic of a two-bed PSA system is shown in Figure 7.

Cryogenic distillation is a widely used method for the separation of gaseous mixtures. This technology is analogous to ordinary distillation, as it relies on the difference

in boiling temperatures of the feed components to perform the separation. However, this process is carried out at relatively low temperatures [66]. Cryogenic distillation is capable of producing hydrogen with moderate purity (≤95%), but it consumes a considerable amount of energy [67]. Additionally, in the case of a feed stream that contains significant amounts of CO and CO_2 (such as a reformate mixture), an additional methane wash column is required to remove these gases [67].

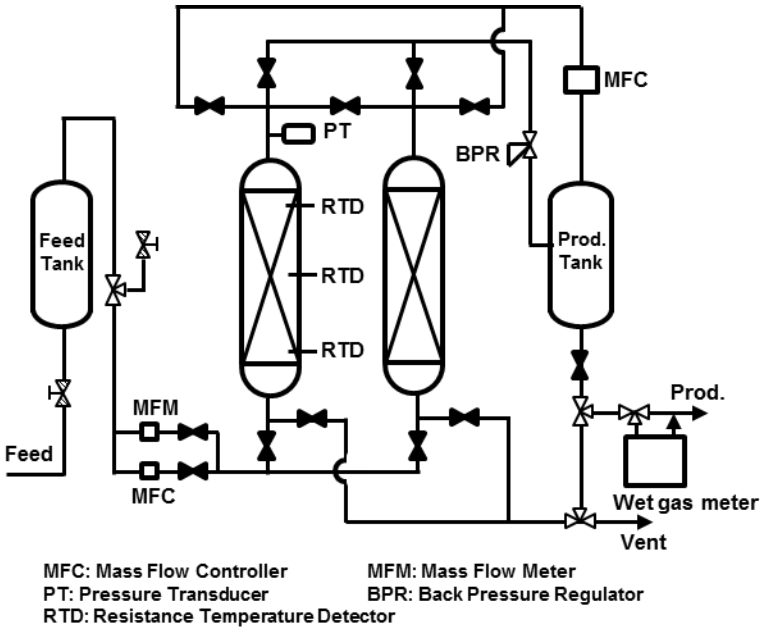

Figure 7. Schematic diagram of a two-bed PSA system [68].

1.6 MEMBRANE SEPARATION

Although PSA and cryogenic distillation are commercially well-established technologies, they suffer from high-energy demands. Gas purification via permselective membranes has attracted significant attention over the past decades owing to the advantages of low capital costs, low-energy consumption, continuous and easy operation,

low footprint, and high capacities [69-71]. Additionally, membrane systems allow for gas separation to be performed in remote locations due to the absence of moving parts [71]. Figure 8 presents a basic schematic of a membrane purification system, consisting of retentate/feed and permeate/sweep volumes.

Membrane purification takes advantage of the difference in individual species' permeation rates through a permselective material. Membrane performance is measured in terms of permeability and selectivity towards the desired permeate. The permeability coefficient (P_i) is the product of the gas flux and membrane thickness divided by the driving force. Its value must be experimentally determined, and it is commonly reported in units of Barrers [72]. A Barrer is a unit for gas separation, and it is defined as:

1 Barrer = 3.348 x 10^{-19} kmol m / (m^2 s Pa).

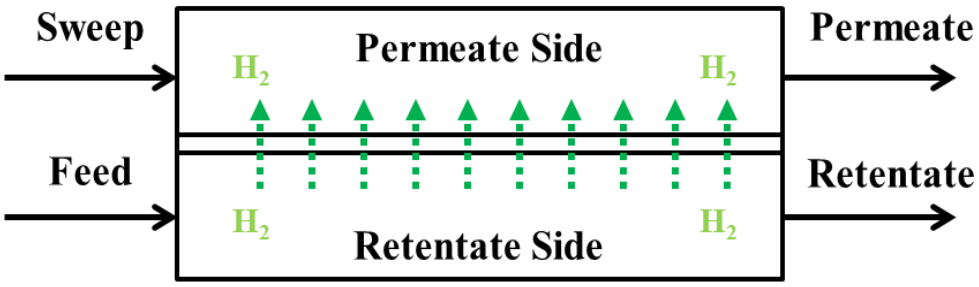

Figure 8. Schematic of a basic membrane purification processes.

The permeability coefficient, P_i, is defined as:

$$P_i = \frac{Q_i \, t_m}{p_2 - p_1} \tag{5}$$

where Q_i is the flux of gas through the membrane, t_m is the membrane thickness, and p_2 and p_1 are the upstream and downstream partial pressures of gas *i*, respectively. The

membrane selectivity is used to assess the separating capacity of a membrane for two (or more) species. The selectivity factor $\alpha_{i/j}$ of two components *i* and *j* in a mixture is defined as:

$$\alpha_{i/j} = \frac{y_i/y_j}{x_i/x_j} \quad (6)$$

where y_i and y_j are the fractions of components *i* and *j* in the permeate side, and x_i and x_j are the fractions in the retentate side. A selectivity factor of unity corresponds to equal permeation rates of species *i* or *j* across the membrane. When the permeate pressure is much lower than the retentate pressure, the selectivity can be written as the ratio of pure gas permeabilities, Equation 7. This selectivity is called the ideal membrane selectivity.

$$\alpha_{i/j,ideal} = \frac{P_i}{P_j} \quad (7)$$

Hydrogen permselective membranes made of molecular sieving carbon, ceramic, metallic and polymer materials have been reported in the literature [59, 67]. In this dissertation, two kinds of hydrogen permselective membranes are reviewed: palladium membranes and polymer membranes.

1.6.1 Palladium Membranes

Palladium (Pd) and its alloys have been extensively investigated for H_2 separation due to their high permeability and high selectivity [59, 73-75]. Dense palladium films possess the unique property of allowing only monatomic hydrogen to dissolve into and diffuse through their crystal lattice at temperatures above 300 °C. Palladium rejects large molecules such as CO, CO_2, O_2, N_2, etc., resulting in very high H_2 selectivities. Hydrogen selectivities in excess of 1000:1 have been reported in the literature [76-78].

Hydrogen transport through palladium membranes has been extensively studied, and it is assumed that it follows the solution-diffusion mechanism. Figure 9 presents a schematic of this process. Hydrogen diffusion from the high-pressure side (retentate) to the low-pressure side (permeate) takes place as follows: [72, 79-81].

1) Diffusion of molecular hydrogen to the membrane surface
2) Dissociative chemisorption of molecular hydrogen on the membrane surface forms atomic hydrogen
3) Diffusion of atomic hydrogen through the membrane matrix
4) Association of atomic hydrogen on the membrane surface
5) Diffusion of molecular hydrogen from the membrane surface to the gas phase

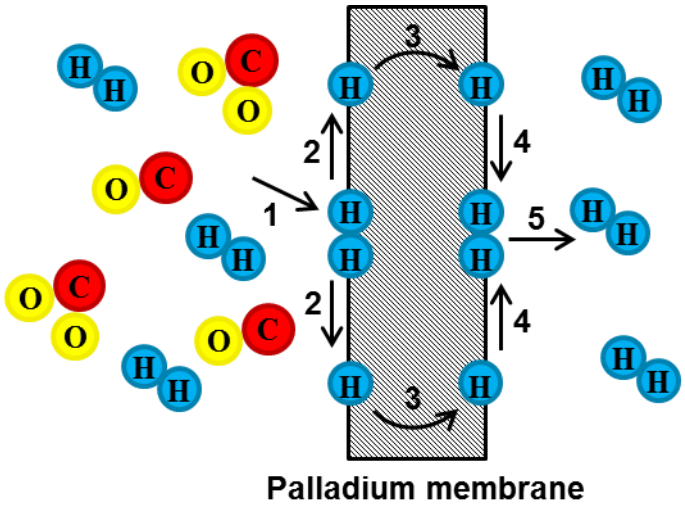

Figure 9. Mechanism of H_2 diffusion through dense palladium membranes [72].

Hydrogen flux through palladium films is described using the following equation:

$$Q_{H_2} = \frac{P_{H_2}}{t_m}\left(p^n_{H_2,ret} - p^n_{H_2,per}\right) \quad (8)$$

where Q_{H_2} is the hydrogen flux through the permselective layer, P_{H_2} is the hydrogen permeability, t_m is the palladium membrane thickness, $p_{H_{2,ret}}$ and $p_{H_{2,per}}$ is the partial pressure of H_2 at the high-pressure side (retentate) and the low-pressure side (permeate), respectively, and n is the partial pressure exponent.

This equation shows that the driving force of hydrogen permeation is the difference in partial pressures across the membrane and that as the membrane thickness increases the permeate hydrogen flux decreases. The partial pressure exponent (n) is experimentally determined and depends on what transport step (Figure 9) is the rate-controlling step. Values between 0.5 and 1 have been reported for this parameter [72, 79]. Sievert's law states that when the diffusion of atomic hydrogen through the membrane matrix (Step 3) is the rate-determining step, the expected value of n is 0.5 since the diffusion rate is related to the concentration of hydrogen atoms on both sides of the membrane, and this concentration is proportional to the square root of the hydrogen partial pressure [82, 83]. When the rate controlling step is the dissociative chemisorption of molecular hydrogen on the membrane surface (Step 2), or the association of atomic hydrogen on the membrane surface (Step 4), or diffusion of molecular hydrogen from or to the membrane surface (Steps 1 and 5), the value of n is 1 because these mechanisms are linearly proportional to the molecular hydrogen concentration [79].

A variety of techniques have been employed for the deposition of Pd and Pd alloy membranes. The most commonly used methods include electroless plating (ELP), chemical vapor deposition (CVD), electrodeposition (EPD), and physical vapor deposition (PVD). The major drawbacks of all these powerful methods are the small defect-free area

of the prepared membranes and/or the high cost of the necessary equipment. A more detailed review of these techniques can be found in the following references [79, 84-89].

Although palladium films have ideal transport properties for hydrogen separation, Pd membranes are limited by high material costs (~23 USD/g). Additionally, these membranes are prone to corrosion/poisoning by hydrocarbon and sulfur compounds, embrittlement, and degradation [59, 67, 73, 81]. Hydrocarbon poisoning can be mitigated by operating at high temperatures to minimize competitive adsorption effects. Sulfur poisoning is a problem when treating feedstocks derived from coal. Sulfur poisoning along with embrittlement and degradation of these membranes can be alleviated by alloying Pd with metals such as Ag, Cu, Fe, Ni, Au, and Ru [81, 90-92], but this usually comes at the cost of a decrease in hydrogen permeability and selectivity.

1.6.2 Polymer Membranes

Polymer membranes are thin films that selectively remove one or more components from a gas mixture. Polymeric membranes are divided into two major classes: porous and nonporous membranes. Gas transport through porous membranes can occur via various mechanisms including Knudsen diffusion, surface diffusion, and molecular sieving (Figure 10) [93]. These mechanisms are largely dependent on the size of the diffusing molecule and the morphology of the polymer membrane. For example, if the membrane pores are relatively large (0.1 - 10 μm), gas permeation is governed by convective flow, and no separation occurs. When membrane pores are smaller than the mean free path of the gas molecules (20 nm - 0.1 μm), gas permeation is controlled by Knudsen diffusion. Finally, if the membrane pores are very small (< 20 nm), gases

permeate through the membrane by molecular sieving [94]. Most commercial gas separation membranes are based on the nonporous polymer membranes [94], so porous membranes will not be further reviewed in this dissertation.

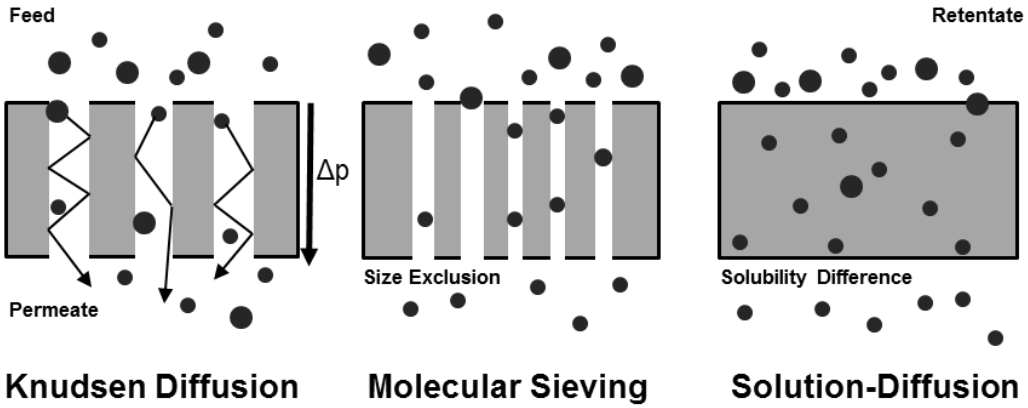

Figure 10. Schematic of different possible mechanisms for gas transport through polymer membranes [95].

Transport in nonporous/dense polymeric membranes is based on the solution-diffusion mechanism [96]. In this mechanism, gaseous molecules are adsorbed on the membrane surface, dissolved into the bulk of the polymer material (solution), transported across the membrane (diffusion), and then desorbed from the membrane surface at the permeate side (Figure 11) [97]. Separation is achieved because of differences in the rate at which the gas components diffuse through the membrane matrix and the amount of material that dissolves in the polymer [98-100]. One key property of dense polymer membranes is their ability to separate permeants of similar size if their solubility in the polymer material differs significantly [95].

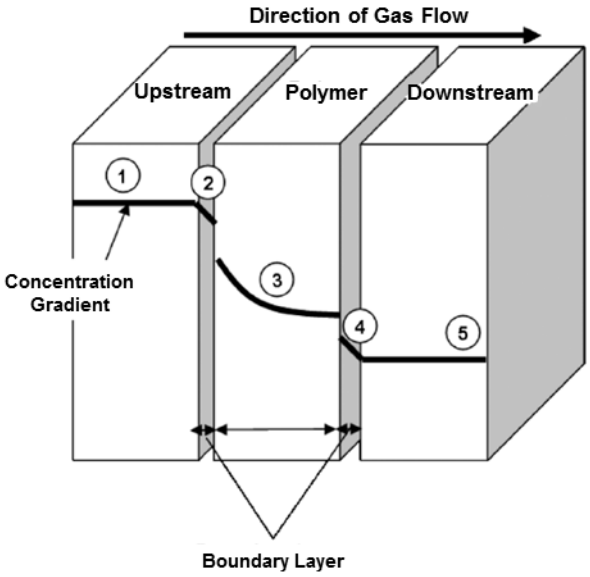

Figure 11. Gas permeation according to the solution-diffusion mechanism [101].

In 1866, Graham proposed a simple equation representing the solution-diffusion mechanism of gases through a polymer membrane [102]. He stated that the permeability coefficient of polymer materials can be represented as the product of a solubility (S) and diffusivity (D) coefficients as shown in Equation 9 [103]:

$$P_i = S_i D_i \quad (9)$$

The solubility coefficient is a thermodynamic term that depends on the gas condensability (characterized by gas critical temperature) and the gas-polymer interactions [97]. The diffusivity coefficient, on the other hand, is a kinetic term that depends on the ability of molecules to move through the surrounding environment. Large penetrants (e.g., CH_4, C_2H_6) typically have lower diffusivity coefficients and are usually more condensable, while small penetrants (e.g., H_2, He) typically have high diffusivities but are usually less condensable [101].

Dense polymer films can be further separated into glassy and rubbery membranes depending on whether the polymer membrane is above or below its glass transition temperature (T_g) [94]. In the case of rubbery membranes, high gas permeabilities are observed as polymer segmental mobility creates a transient free-volume that allows gas diffusion through the polymer to occur more easily, but it is usually at the expense of lower selectivities [104]. In glassy polymer membranes, chain mobility is limited resulting in low to medium gas permeabilities but high selectivities. For rubbery membranes, the solubility usually governs over diffusivity, so gas permeability is favored for large penetrant sizes, while for glassy membranes, the diffusivity coefficient is dominant over the solubility term; therefore, gas permeability increases with decreasing penetrant size [105, 106].

Polymer membranes represent a low-cost alternative to palladium membranes for H_2 purification [60, 100, 107]. Polymer membranes have a good ability to stand high-pressure drops [67] and have good scalability, but suffer from low mechanical strength, low selectivity, high sensitivity to swelling, and are prone to degradation/corrosion by CO and sulfur components [59, 67]. Research to date has focused on modifying polymer's chemical structure to prepare novel polymers with high permeability, high selectivity, and high chemical resistant [60, 107]. Both high permeabilities and high selectivities are desirable for increasing process throughput and product purity [95]. The main obstacle encountered by polymer membranes is the inverse relationship between selectivity and permeability [108]. This trade-off translates to an upper bound concept introduced by Robeson in 1991 and revisited in 2008 [108, 109]. This proposed upper bound gives

insight into the maximum selectivity that can be obtained for a given permeability [59]. Figure 12 shows this concept of the upper bound for several polymer membrane materials involved in CO_2/N_2 separations. A theoretical model that describes the upper bound behavior of polymer films was developed by Freeman [110] based on the assumption of a homogeneous polymer structure chemistry.

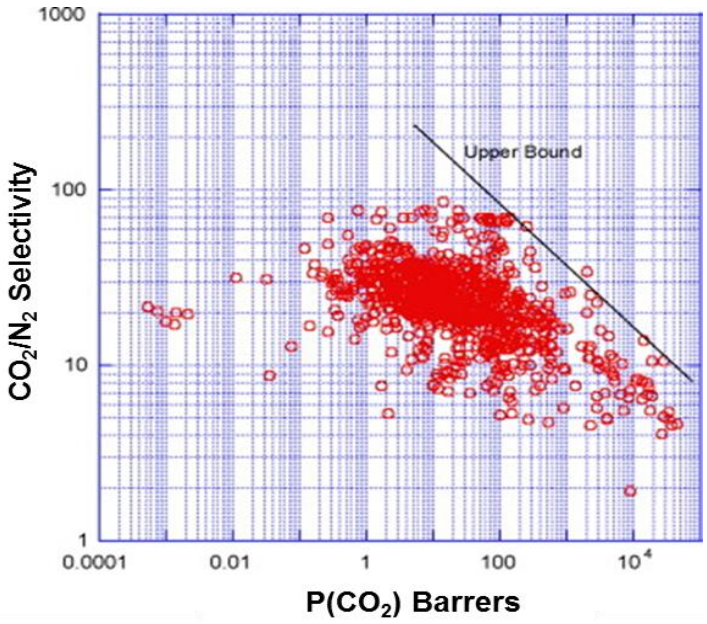

Figure 12. Upper bound correlation for CO_2/N_2 separation [109].

Several techniques have been employed for the deposition of polymer membranes. The two most common film fabrication methods are melt-pressing and solvent-casting [111, 112]. Melt-pressing requires the application of heat to melt a polymer powder, and then a film is prepared by pressing the hot polymer under high pressure. On the other hand, solvent-casting requires the dissolution of a polymer material in a volatile solvent. The resulting solution is cast on a leveled plate by using a casting knife, and the solvent is

allowed to evaporate, leaving the polymer film behind. Solvent-casting is a widely used method to prepare films and is often preferred over melt-pressing [113].

Another film fabrication technique that has gathered interest in the last two decades is the Layer-by-Layer (LbL) method. LbL is an assembly technique that produces thin films (typically < 1 μm thick) by alternately dipping a substrate into different polymer solutions with a specific interaction (e.g., ionic interactions or hydrogen bonding) (Figure 13) [114-117]. The attraction of these materials will allow the formation of a multilayer structure (Figure 14). The advantage of this method is the precise tailorability of film's morphology through adjustment of concentration [118], pH (ionic strength) [119, 120], temperature [121], molecular weight [122], and deposition time [123] of the individual polymer solutions. Additional advantages of the LbL technique include 1) simple and self-healing process that is typically performed at ambient conditions, and 2) it uses low-cost and eco-friendly raw materials.

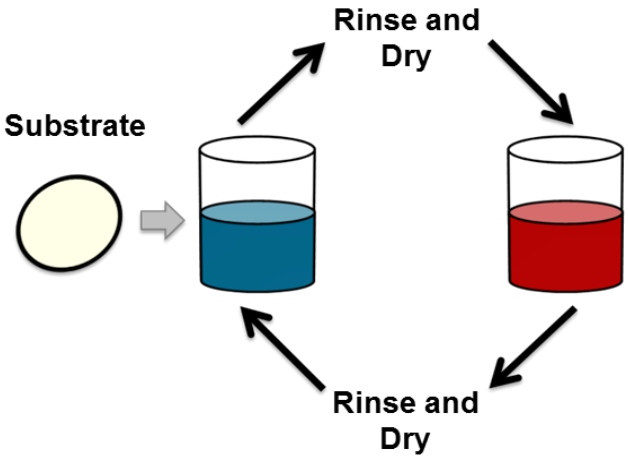

Figure 13. Layer-by-Layer deposition process.

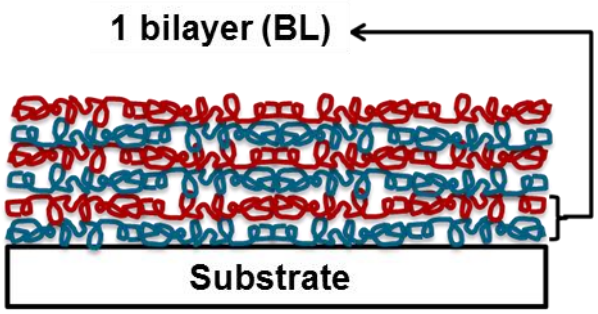

Figure 14. Layer-by-Layer deposition on a substrate.

This method of depositing thin films has been studied for a wide range of applications including gas separation [124], gas barrier [125, 126], anti-reflection and antimicrobial coatings [127-129], degradable encapsulation [130], and biomedical applications [131]. Part of this dissertation is dedicated to investigating the gas barrier and gas separation properties of thin films fabricated using the LbL method. The hypothesis is that by altering the composition, number, and order of polymer layers, a limitless opportunity for new film's functionalities is opened.

1.6.2.1 LbL Gas Barriers Membranes

Gas barrier films have found broad application in a variety of packaging applications for the food and pharmaceutical [132], flexible electronics [133], and fuel cell [134] industries. These films often require a combination of low permeability, optical transparency, mechanical strength, and flexibility [135]. The absence of metallic material is also important for recyclability and microwavability [136].

In this dissertation, a highly flexible, transparent LbL polymer-clay film with low H_2 and He permeabilities is presented in Chapter IV. Commercial H_2 and He barriers include metallized films [137], SiO_x coatings [138] and polymer composites [139]. While

these materials offer good barrier properties, they often suffer from poor substrate adhesion, undesirable optical quality, complex fabrication procedures, and limited flexibility [140]. The simplicity of the LbL technique, as compared to current gas barrier film fabrication methods, makes it an attractive alternative. Additionally, LbL nanocomposites prepared with polymers and clay nanoplatelets have proven capable of addressing the current challenges of commercial barrier films while still proving the desired optical and mechanical properties [141-144].

Uniformly mixing of polymer and clay nanoplatelets does not always result in the fabrication of a nanocomposite, but rather in the agglomeration of large stacked platelets. This agglomeration is a result of the weak interactions between polymer and inorganic components, which translates to poor barrier properties relative to a fully exfoliated nanocomposite [145]. Previous work on nanoclay-based composites have suggested three types of morphologies in polymer-clay nanocomposites (Figure 15) [146]: 1) stacked or phase separated, 2) intercalated, and 3) exfoliated. Film fabrication conditions such as temperature [147], solution concentration [145], and interfacial interactions between polymer and inorganic component [148] will control the extent of clay exfoliation in the final film. The LbL technique can be used to produce thin films with exfoliated clay structures (or nanobrick wall structures) that provide extremely low gas permeabilities. These nanobrick wall thin films have demonstrated undetectable oxygen transmission rate (OTR^2<0.005 cm^3 m^{-2} day^{-1} atm^{-1}) others of magnitude lower than the rivals metallized films [149].

[2] Oxygen Transmission Rate

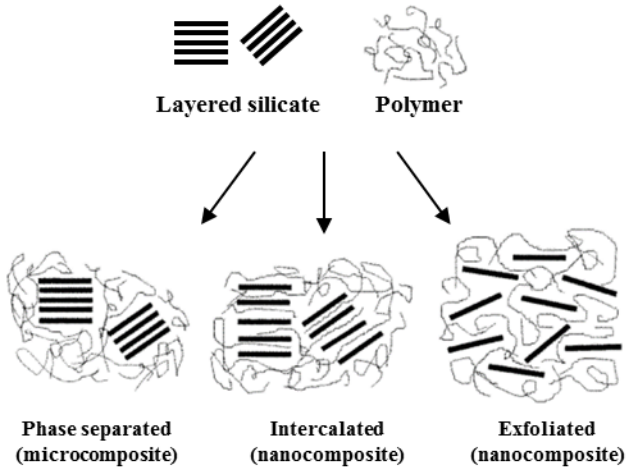

Figure 15. Schematic of the different types of morphologies generated based on the interactions between layered silicate and polymer matrices [145, 146].

Gas transport through nanocomposites can be described by the solution-diffusion mechanism. The gas solubility in the composite is given by [150]:

$$S = S_0 (1- \phi) \quad (10)$$

where S_0 is the gas solubility coefficient of the neat polymer and ϕ is the volume fraction of clay in the matrix. Equation 10 assumes that the clay nanoplatelets do not have any effect on the surrounding polymer matrix and that the polymer solubility does not depend on the morphology of the phases [150]. For estimating the diffusion coefficient, it is assumed that the clay nanoplatelets act as impermeable gas barriers and force penetrant to follow an elongated, or tortuous, pathway to diffuse across the polymer-clay nanocomposite. The gas diffusivity can be described as:

$$D = D_0 f \quad (11)$$

where D_0 is the diffusivity coefficient of the pure polymer matrix and f is the tortuosity factor, that accounts for that reduction in diffusivity due to the elongated pathway [150]. Combining Equations 9, 10, and 11 gives

$$P = S_0 (1- \phi) D_0 f = P_0 (1- \phi) f \quad (12)$$

where P_0 is the penetrant permeability coefficient in the neat polymer.

A more elaborated tortuous path model was proposed by Cussler in 1988 [151]. Cussler's model states that the relationship between the gas permeability of a filled polymer matrix and neat polymer is:

$$P = \frac{P_0}{1+\frac{\mu\alpha^2\phi^2}{(1-\phi)}} \quad (13)$$

where α is the clay aspect ratio and μ is a geometric factor representing the shape of the clay nanoplatelets. Cussler's model can be used to describe gas diffusion phenomena for both dilute ($\alpha\phi \ll 1$) and semi-dilute ($\alpha\phi \gg 1$) regimes [152, 153].When the platelets are in a regularly oriented array, $\mu = 1$, and when the platelets are in a randomly oriented array, $\mu = 4/9$. These possible geometries of platelets in the composite are shown in Figure 16.

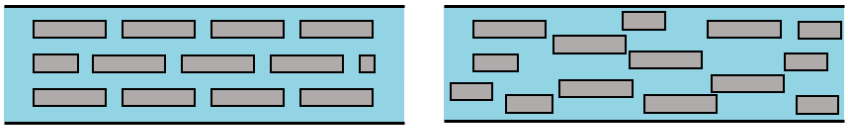

Figure 16. Geometries of regular and random arrays for platelet-filled polymers [150].

1.6.2.2 LbL Gas Separation Membranes

For gas separation membranes high permeability and selectivity are always desired. Gas separation films must be defect-free as small gas molecules can diffuse

through any defect [143]. The LbL technique allows the formation of defect-free thin films with unique structures and transport properties. Stroeve et al. [144] reported an assembly of 100 polymer layers of poly(allylamine) (a polycation) and poly(styrenesulfonate) (a polyanion) deposited on solid dimethyl silicone membranes. Results indicated reduced gas permeability but higher CO_2/N_2 selectivity (~24) than the bare substrate at moderately high temperatures (50 °C). Leväsalmi and McCarthy [154] reported an increased selectivity for H_2/N_2 and H_2/O_2 by depositing 20 to 200 polymer layers of poly(allylamine hydrochloride) and poly(sodium styrene sulfonate) onto surface-oxidized poly(4-methyl-1-pentene) substrate. Gas permeabilities of these membranes decreased as the number of layers increased due to the dense structure of the polyelectrolytes in the layers. Sullivan and Bruening [155] deposited poly(amic acid) salts and poly(allylamine hydrochloride) membranes on porous alumina supports. After the LbL films were deposited, heat-induced imidization was used to convert the poly(amic acid) to the corresponding polyimide. The newly formed polyimide membranes exhibited gas selectivities comparable to conventional polyimides membranes (O_2/N_2 6.9 and CO_2/N_2 68). Kim et al. [124] reported an ion-paired polyethylenimine (PEI)/ poly(acrylic acid) (PAA) thin film with outstanding H_2/N_2 and H_2/CO_2 selectivities owing to a unique ionically crosslinked structure achieved by using the LbL technique.

In this work, a highly selective LbL film for the separation of CO_2 from flue gas is presented. CO_2 emissions associated with flue gas have a significant impact on climate change. Although it is impossible to stop the effects of climate change, it is possible to mitigate them. One option is the reduction of CO_2 emissions from flue gases using CO_2-

permselective membranes to isolate CO_2 for controlled disposal. In this work, a thin film of poly(ethylene oxide) (PEO) and poly(methacrylic acid) (PMAA) fabricated via LbL assembly showed CO_2/N_2 selectivities up to 141 (the highest CO_2/N_2 selectivity reported for homogeneous polymer materials). Details of material properties and permeability measurements are be presented in Chapter V.

1.7 MULTIFUNCTIONAL REACTORS

Multifunctional reactors integrate chemical reactions with physical operations (e.g., membrane separation, gas adsorption, distillation) in one device to create synergetic effects, which enhance the performance of the reaction and/or the physical process. This strategy of combining multiple physical and/or chemical operations in a single integrated unit is known as process intensification [156].

The MSR and the WGS are equilibrium-limited reactions; therefore, require additional capital cost associated with multi-staged beds to maximize H_2 yield [157]. Due to the equilibrium-limited nature of these reactions, they are ideal candidates for investigating the performance of multifunctional reactors. Hydrogen recovery from reformate mixtures may be enhanced by coupling H_2 or CO_2 separation with the MSR/WGS reaction in a single unit. By continuously removing one of the reaction products, equilibrium limitations on CO conversion may be eliminated in accordance with LeChatelier's Principle [158-160]. Additionally, overall system size and complexity could be reduced. The coupling of chemical reaction with gas separation processes can be achieved in several ways. Two of the most studied designs include the membrane reactor

design and the sorption-enhanced reforming process. A brief description of these two designs is given below.

1.7.1 Membrane Reactor

Membrane reactors have been widely investigated over the years, as they allow a parallel integration of membrane separation technology and chemical reaction [158, 161-163]. Membrane reactors are classified depending on the location of the catalyst in the reactor. The most common membrane reactor configurations include the packed-bed membrane reactor (PBMR), the catalytic membrane reactor (CMR) and the packed-bed catalytic membrane reactor (PBCMR). In this dissertation attention will be given solely to the PBMR configuration. A more detailed review of the CMR and PBCMR configurations can be found in the following reference [164].

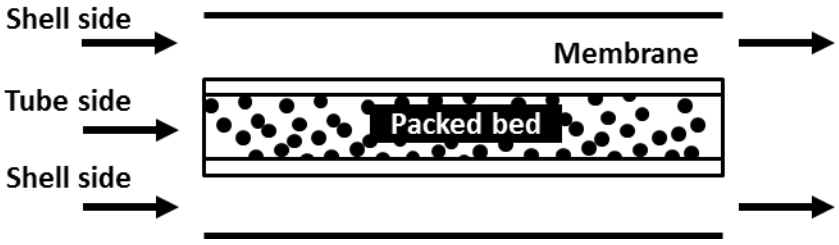

Figure 17. Basic schematic of a packed-bed membrane reactor configuration [164].

In the PBMR configuration, shown in Figure 17, the permselective membrane is deposited on the inner tube of a shell and tube design, and catalyst particles may be packed inside or outside the membrane tube such that reaction and separation occur in parallel. The permeate volume is held at a lower pressure than the retentate volume to maintain enough driving force for gas permeation to occur. Several studies have reported the use of

PBMRs for coupling the WGS reaction with either H_2-permselective Pd membranes [158, 163] or CO_2-permselective polymeric membranes [160, 165] to produce high-purity hydrogen from reformate mixtures.

While the PBMR configuration enables gas purification to enhance catalytic reaction rates, the permselective film remains directly exposed to contaminants (e.g., CO and H_2O). To address this limitation, an alternative approach to coupling catalytic reaction with gas purification has been developed wherein a sufficiently thick catalyst layer is washcoated over the retentate surface of the permselective film, such that undesired contaminants are catalytically destroyed before reaching the permselective surface (Figure 18) [166-168]. Likewise, catalytic production of desired permeating species in close proximity to the permselective surface further enhances gas permeation rates. This composite catalytic-permselective (CCP) membrane design was first demonstrated for preventing corrosion of ultra-thin (200 nm) Pd films by methanol in a miniaturized membrane reformer [169].

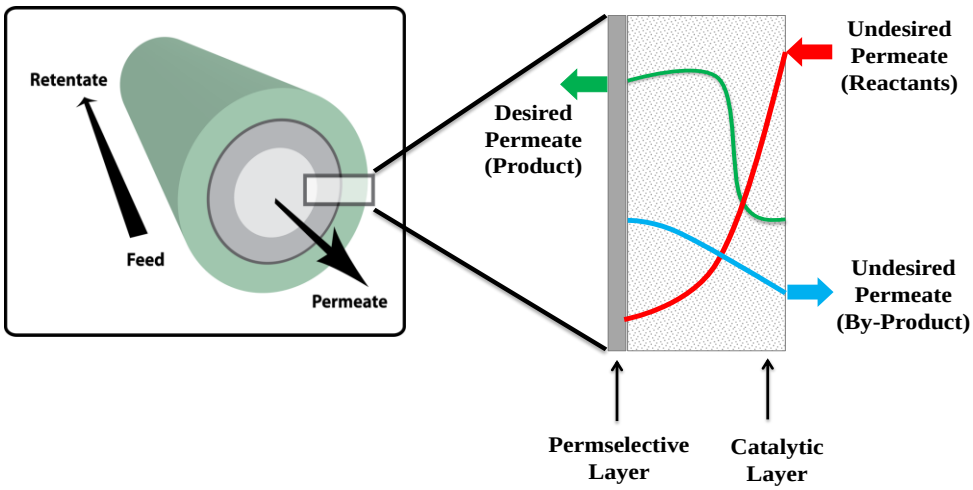

Figure 18. Illustration of composite catalytic-permselective membrane design. The inset shows a schematic concentration profile of desired and undesired species within the catalytic layer [168].

In this dissertation, a study comparing the performance of the composite catalytic-permselective against the packed-bed membrane reactor and a gas purification membrane system is presented. Comparison is made for the case of coupling water-gas shift reaction with 1) an infinitely H_2-permselective Pd film accounting for surface inhibition by CO and 2) a moderately CO_2-permselective polymeric film operating in the absence of surface inhibition. Results from this work will determine under which set of conditions each design is favored.

1.7.2 Sorption-Enhanced Reforming Reactor

Hydrogen recovery from reformate mixtures can also be enhanced by coupling CO_2 adsorption with methane steam reforming or water-gas shift reaction in a process known as sorption-enhanced reforming process (SERP) [170]. This process is analogous to a membrane reactor since product removal is coupled with chemical reaction, in a single unit, to overcome reaction equilibrium limitations. In SERP, CO_2 is removed from the

gaseous phase by a solid adsorbent causing the reaction equilibrium to shift toward the product side. SERPs have received significant attention over the past two decades owing to a growing demand for high-purity H_2 and rising costs associated with CO_2 emissions [171, 172].

As mentioned in Section 1.5, the MSR-WGS reformate stream requires further purification to achieve the H_2 purities required by many refinery operations [29, 48, 173]. Purification processes based upon the selective removal of H_2 typically result in rejection losses, which translate to H_2 waste. Additionally, these processes do not offer a direct means to capture CO_2 for appropriate utilization or disposal. Process intensification via SERP addresses these challenges by isolating CO_2 from the reacting fluid using a solid adsorbent, thereby removing equilibrium limitation on H_2 yield while simultaneously purifying the product stream.

The selected adsorbent must be capable of CO_2 sorption at the conditions of the reactions (473 K - 1023 K). Calcium oxide (CaO) adsorbents are ideal candidates for CO_2 adsorption processes because they are inexpensive and abundant. Sorption of CO_2 occurs via reversible exothermic reaction of CO_2 and CaO (Equation 14) that yields to calcium carbonate ($CaCO_3$) in the solid phase [174-176]. Inspection of the equilibrium CO_2 pressure over CaO indicates that H_2 purification via CO_2 sorption using CaO-based adsorbents is compatible with MSR and WGS operating conditions [173].

$$\mathrm{CaO(s)} + \mathrm{CO_2(g)} \rightarrow \mathrm{CaCO_3(s)} \qquad \Delta \mathrm{H}^0_{\mathrm{rxn}} = -178\ \mathrm{kJ/mol} \tag{14}$$

The majority of reports on sorption-enhanced methane steam reforming (SEMSR) and sorption-enhanced water-gas shift (SEWGS) have focused upon a two-pellet design,

where the sorptive and catalytic properties are distinguished into separate pellets [170, 177-179]. Han and Harrison [180] provided the first experimental demonstration of SEWGS process over a natural dolomite (CaO-MgO) adsorbent bed. Their results demonstrated that equilibrium for SEWGS process can be obtained at 15 atm, in the temperature range of 500 °C to 600°C and with space velocities as high as 3400 h^{-1} (STP). Total concentrations of CO and CO_2 of ~300ppm (dry basis) in the reactor product were achieved. Hufton et al. [181] reported H_2 production through SEMSR over a K_2CO_3 treated hydrotalcite (HTC) adsorbent, with an outlet stream hydrogen purity of approximately 96% and with CO and CO_2 content below 50 ppm. Balasubramanian et al. [182] showed that a gas stream with H_2 content up to 95% (dry basis) could be produced via SEMSR using a NiO/Al_2O_3 catalyst with a CaO-based adsorbent operating at 15 bar and 650 °C. Ortiz and Harrison [183] demonstrated high-purity H_2 production via SEMSR using a packed-bed reactor containing a NiO/Al_2O_3 catalyst bed mixed with a 2.7:1 adsorbent to catalyst ratio at 15 bar, 650 °C, and a 6:1 H_2O:CH_4 mixture.

While the SEMSR and SEWGS configurations enable gas purification to enhance catalytic reaction rates, bed-scale dilution of CO_2 partial pressures limits sorption rates, while intraparticle diffusional limitations hinder catalyst effectiveness [184]. To address these limitations, multifunctional catalysts combining sorptive and catalytic properties at the particle scale have recently garnered interest. In this dissertation, a study comparing the performance of two multifunctional catalyst designs proposed for SERP processes (i.e., the core-shell design and the uniform-distributed design) is presented. The results

from this work will help to determine under a specific set of operating conditions which design option is favored.

1.8 OBJECTIVES OF THIS RESEARCH

With the world's expanding energy demands, the increasing concerns regarding the environmental impact of fuel production and the need for greater energy diversity, a solution is needed for a universal, emission-free fuel. Hydrogen has emerged as a promising energy alternative. This research work aims to improve enhanced H_2 recovery from hydrocarbon resources. The central hypothesis is that optimal patterning of reaction and separation may be used to manipulate local driving forces for H_2 or CO_2 removal to significantly enhance catalyst utilization and product removal rate. This concept is demonstrated in two different designs: 1) a composite catalytic-permselective membrane for WGS reaction coupled with H_2 or CO_2 removal (Chapter II) and 2) a multifunctional catalyst for SEWGS and SEMSR (Chapter III).

Chapter II outlines a new approach for integrating chemical reaction with selective product removal in a composite catalytic-permselective membrane design by employing a sequentially structured integration of the catalytic and separation functionalities. In this unique design, the catalytic layer is coated on top of the permselective material, such that undesired contaminants are catalytically destroyed before reaching the permselective surface. Likewise, catalytic production of desired permeating species in close proximity to the permselective surface further enhances gas permeation rates. This novel design represents a significant departure from membrane reactors current state-of-the-art

approach, which employs a packed-bed membrane reactor configuration that relies on parallel coupling of the reaction and separation functionalities.

Chapter III presents a new approach to coupling reaction with gas adsorption in the unsteady-state sorption-enhanced reforming process. Patterning of sorptive and catalytic functionalities at the particle level exploits diffusional limitations within the catalyst to enhance the driving force for CO_2 adsorption, improving sorption rates. Similarly, in-situ removal of CO_2 within the particle is expected to reduce equilibrium limitations upon catalytic reaction, resulting in significant enhancement of catalyst utilization. These multifunctional designs are expected to achieve a superior performance than the conventional two-pellet approach, in which the adsorbent and catalyst functionalities are separated into different particles.

Chapter IV and V of this dissertation are dedicated to the investigation of novel LbL polymer membranes for gas separation and gas barrier applications. The LbL technique allows the sequentially structured integration of distinct material and/or structural properties to achieve new films with better functionalities. Chapter IV presents a study of thin LbL films that have extremely low permeability to small gases such as H_2 and He. A quadlayer assembly, consisting of PEI, PAA, and montmorillonite (MMT) clay was deposited on a polystyrene substrate via LbL assembly to create the barrier films. Cross-sectional TEM images were used to observe the clay's exfoliated structure while increasing the number of quadlayers. Gas barrier properties as a function of the number of quadlayers deposited were investigated. These barrier coatings would allow size and weight reduction for He/H_2 storage and transportation equipment. These coatings would

also allow the extension of process equipment lifetime by reducing the risk of equipment failure due to H_2 embrittlement.

Chapter V presents the experimental investigation of a highly selective LbL for the separation of CO_2 and N_2 gases. In this work, a thin film of PEO and PMAA fabricated via LbL assembly showed CO_2/N_2 selectivities up to 141 (the highest CO_2/N_2 selectivity reported for homogeneous polymer materials). Surface and cross-sectional SEM images were taken to confirm film's uniformity over the substrate. These CO_2-permselective films could be employed to selectively remove CO_2 from flue gas mixture, reducing in this way greenhouse gas emissions. A summary of this work findings and recommended future work is presented in Chapter VI.

CHAPTER II

COMPOSITE CATALYTIC PERMSELECTIVE MEMBRANE*

2.1 INTRODUCTION

Packed-bed membrane reactors (PBMRs) have been widely investigated over the years for simultaneous H_2 production and purification. The most common types of permselective materials used in these reactors include palladium (Pd) membranes and polymer membranes. These permselective materials offer excellent permeability and selectivity properties; however, they are prone to corrosion and degradation by contaminants such as CO. While the PBMR configuration enables gas purification to enhance catalytic reaction rates, the permselective film remains directly exposed to contaminants. The composite catalytic-permselective (CCP) membrane design, introduced in Section 1.7.1, has been reported to overcome the above-mentioned problem of the PBMR design and enhance the separation performance [169]. The addition of a porous catalytic layer on top of the permselective membrane modifies the gas composition at the membrane surface by reducing the undesired permeate content, resulting in an enhancement of desired product permeance and selectivity [167, 169].

One-dimensional modeling of a CCP membrane coupling reversible water-gas shift (WGS) reaction with an infinitely H_2-permselective Pd film predicted up to an 80% reduction in CO partial pressure at the catalyst-membrane interface relative to the bulk

* Reprinted with permission from "Composite Catalytic-Permselective Membranes: Modeling Analysis for H_2 Purification Assisted by Water-Gas-Shift Reaction" by Elva Lugo and Benjamin Wilhite, 2012. Chemical Engineering Journal, 207-208, pp. 552–563, Copyright 2012 by Elsevier B.V.

fluid CO partial pressure [168]. Equivalent increases in H_2 partial pressure at the Pd surface corresponded to a predicted enhancement of H_2 permeation rates of ~5%. All simulations were performed under inlet conditions and neglecting any inhibitory effects of CO upon H_2 permeability. Analysis of an equivalent CCP membrane coupling WGS reaction with a moderately CO_2-permselective polymeric film predicted similar enhancements in the initial rate of CO_2 permeation alongside a two order of magnitude improvement in initial CO_2:CO separation [168]. Kim et al. [167] experimentally demonstrated the composite catalytic-permselective membrane concept using a 27-μm electroless-plated dense palladium film in contact with a 500-μm catalyst layer active for WGS reaction. Their results confirmed the enhancement of H_2 permeation through dense palladium films via integration with WGS reaction in a CCP membrane design, as previously predicted by one-dimensional analysis.

This work details two-dimensional modeling analysis of a CCP membrane design for coupling water-gas shift reaction with 1) an infinitely H_2-permselective Pd film accounting for surface inhibition by CO, and 2) a moderately CO_2-permselective polymeric film operating in the absence of surface inhibition. The former case enables a direct comparison of the anti-inhibitory/anti-corrosion benefits of the CCP system against equivalent gas purification membrane (GPM) and packed-bed membrane reactor designs. The latter case enables a direct comparison of the CCP system against equivalent GPM and PBMR designs in terms of improving the effective permselectivity of the membrane. In both cases, two-dimensional analysis accounts for changing gas compositions along the entire axial length of a counter-current membrane system.

2.2 DEVELOPMENT OF CCP, PBMR, AND GPM MODELS

Two-dimensional models are developed for comparing the performance of the CCP membrane design against GPM and PBMR configurations. All three reactor configurations (CCP, GPM, and PBMR) are described using isothermal models based upon the geometry of the micromembrane system employed by Wilhite et al. to first demonstrate the CCP concept [168]. This geometry facilitates the use of isothermal, Cartesian reactor models with identical relevant dimensions and membrane surface area to catalyst volume ratios. Details of each model development are provided below.

The composite catalytic-permselective membrane (Figure 19a and 19b) is modeled as an isothermal two-dimensional Cartesian catalyst volume, with Fickian diffusion of individual species described using effective diffusivities and catalytic reaction described using the rate expression developed by Mizssey et al. [185]. The resulting model equation describes diffusion and reaction along the axis of gas flow (z) and the axis of diffusion (x):

$$\frac{D_i^{eff}}{RT}\left(\frac{\partial^2 p_i^{cat}}{\partial x^2}+\frac{\partial^2 p_i^{cat}}{\partial z^2}\right)= r_i \qquad (15)$$

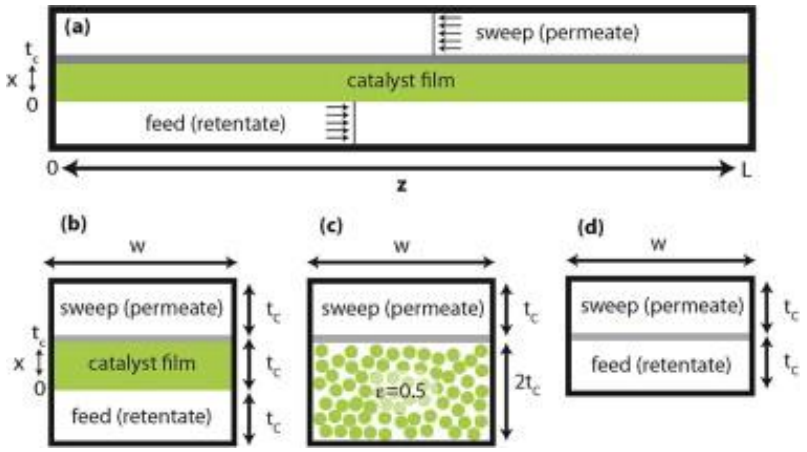

Figure 19. Schematic presents the three reactor configurations compared in this study. (a) z-axis cross-section; (b) x-axis cross-section of CCP membrane; (c) equivalent PBMR model, x-axis cross-section; and (d) equivalent GPM model, x-axis cross-section [166].

The Fickian diffusion model neglects convective transport within the porous catalyst, justified by the mole-neutral nature of the water-gas shift reaction and assuming a combination of sufficiently low local permeation rates through the permselective film and overall catalytic film permeances such that negligible gas convection arises from a drop in total pressure at the permselective film surface. Uniform temperature within the catalyst film is justified by determination of the Prater number[3] (representing the maximum temperature in the catalyst) associated with initial feed composition [159].

$$\beta = \frac{(-\Delta H_{wgs}) D_{CO}^{eff} \frac{p_{CO,0}^{F}}{RT_0}}{k_e T_0} = 3 \times 10^{-3} \quad (16)$$

Effective diffusivities are assumed to be isotropic and are estimated from a combination of Knudsen and multicomponent Maxwell-Stefan diffusivities via Bosanquet approximation,

[3] The Prater number represents the maximum rise in temperature within the catalyst at inlet conditions.

$$D_{ij}^{eff} = \frac{1}{\frac{1}{D_{i,mix}^{eff}} + \frac{1}{D_{i,K}^{eff}}} \qquad \text{where} \quad D_{i,k}^{eff} = 97 \frac{\epsilon}{\tau} \overline{r_p} \left[\frac{T}{M_i}\right]^{\frac{1}{2}} \quad \text{and} \quad D_{i,mix}^{eff} = \frac{1}{\sum_{i \neq j} \left(\frac{x_j}{D_{ij}(1-x_i)}\right)} \tag{17}$$

Binary diffusion coefficients are estimated using the method of Fuller, Schettler and Giddings method [186] accounting for catalyst tortuosity and porosity as:

$$D_{ij}^{eff} = \frac{\epsilon}{\tau} \frac{1 \times 10^{-7} \, T^{1.75} \left(\frac{1}{M_i} + \frac{1}{M_i}\right)^{\frac{1}{2}}}{P \left({v_i}^{1/3} + {v_j}^{1/3}\right)^2} \tag{18}$$

where empirical values for diffusion volume (v) are employed for CO (18.9), CO_2 (26.9), H_2 (7.07), H_2O (12.7), and N_2 (17.9). A catalyst porosity of 50% is assumed, with nominal pore diameter of 10 nm and tortuosity of 2, based upon correlations by Neurock et al. [187].

Zero-flux boundary conditions are assumed at both entrance and exit regions of the catalyst volume. Robin-type boundary conditions [159] are employed for equating species-specific diffusive fluxes normal to the catalyst surface, to the rate of mass supplied at the feed volume interface (x = 0) and the permselective film flux at catalyst-permselective film interface (x = t_c), respectively.

$$\frac{D_i^{eff}}{RT_0} \frac{\partial p_i^{cat}}{\partial z} = 0 \qquad \text{at} \qquad z = 0, L \tag{19}$$

$$\frac{D_i^{eff}}{R_g T_0} \frac{\partial p_i^{cat}}{\partial x} = k_{gs}\left(p_i^F - p_i^{cat}\right) \qquad \text{at} \qquad x = 0 \tag{20}$$

and

$$\frac{D_i^{eff}}{RT_0} \frac{\partial p_i^{cat}}{\partial x} = Q_i^{Pd,Poly} \qquad \text{at} \qquad x = t_c \tag{21}$$

The former boundary condition employs a mass transfer coefficient corresponding to negligible fluid-phase resistance to interphase mass transfer, such that mass transfer

resistances only occur within the catalytic film itself. The latter boundary condition employs either a Sievert's Law or first-order permeation model to describe the molar flux of species *i* through either an infinitely H_2-permselective dense Pd film or a moderately CO_2-permselective polymeric film. The above boundary conditions for the catalyst film are coupled to a pair of one-dimensional fluid-phase models describing the feed (retentate) and sweep (permeate) volumes, assuming countercurrent operation and ideal plug-flow:

$$\frac{1}{A_C^F}\frac{dF_i^F}{\partial z} = -k_{gs}\hat{a}^F\left(p_i^F - p_i^{cat}\right) \qquad \text{and} \qquad -\frac{1}{A_C^S}\frac{dF_i^S}{\partial z} = \hat{a}^S Q_i^{Pd,Poly} \tag{22}$$

An inlet flow composition of 9 mol% CO, 28 mol% H_2, 15 mol% H_2O, 3 mol% CO_2, balance with nitrogen is assumed for the feed stream in all simulations, assuming the feed gas is typical of a diesel or equivalent hydrocarbon reformate. The sweep gas is assumed to be comprised of pure nitrogen in all simulations.

A one-dimensional isothermal PBMR model (Figure 19c) is developed in order to provide a direct comparison between CCP and PBMR performance both in terms of gas purification and reaction conversion. The feed and sweep volumes are modeled assuming plug-flow, with catalytic reaction described using a pseudo-homogeneous model and assuming negligible mass transfer resistance to reaction both internal and external to the catalyst.

$$\frac{1}{A_C^F}\frac{dF_i^F}{\partial z} = r_i(1-\varepsilon_{bed}) - \hat{a}^F\varepsilon_{bed}Q_i^{Pd,Poly} \qquad \text{and} \qquad -\frac{1}{A_C^S}\frac{dF_i^S}{\partial z} = \hat{a}^S\varepsilon_{bed}Q_i^{Pd,Poly} \tag{23}$$

These simplifying assumptions ensure a stringent basis of comparison between the conventional PBMR and proposed CCP designs, as the presence of finite mass transfer resistances within the PBMR system may be expected to favor the CCP design. The

present assumption of uniform temperature is selected to facilitate a first system-level comparison of the CCP design while establishing the necessary basis for future non-isothermal and adiabatic designs. Additionally, negligible mass transfer resistance between the fluid-phase and the permselective film is assumed to ensure consistency with the CCP model described above. Feed and sweep inlet gas compositions are identical to those used for the CCP model.

Lastly, the performance of the CCP membrane is compared to a reference case of an un-modified permselective film for gas purification (Figure 19d). As in the two previous models, isothermal plug-flow is assumed in both feed and sweep volumes while inlet gas compositions are identical to those described for the CCP model.

$$\frac{1}{A_C^F}\frac{dF_i^F}{\partial z} = -\hat{a}^F Q_i^{Pd,Poly} \qquad \text{and} \qquad -\frac{1}{A_C^S}\frac{dF_i^S}{\partial z} = \hat{a}^S Q_i^{Pd,Poly} \tag{24}$$

In all three model cases, uniform temperature is assumed in both feed and sweep volumes. Likewise, negligible fluid-phase pressure drop is assumed with feed and sweep pressures of 3 atm and 1 atm employed for all simulations. These assumptions, combined with the use of Fickian diffusion models in the catalyst layer, allow analysis of the influence of reaction-diffusion phenomena upon permselective film performance for the CCP membrane, and comparison of CCP membrane performance against equivalent PBMR and non-reactive membrane designs, in the absence of secondary effects. As summarized in Table 4, geometries and packed-bed void fractions are selected such that all three models share identical feed and sweep flow volumes to facilitate simulations at identical residence times; dimensions are likewise selected to enable simulations at identical membrane surface areas. Feed molar flowrates are varied over an appropriate

span of values such that desired permeate (H_2 or CO_2) recoveries between 10% and 90% are achieved, maintaining identical sweep and feed total molar flowrates.

Table 4. Comparison of dimensions for CCP, PBMR, and GPM model. Selection of packed-bed void fraction (ε_{bed}) of 50% results in identical feed and catalyst volumes between all models.

	CCP	PBMR	GPM
Feed volume	$(t_C)(w)(L)$	$(\varepsilon_{bed})(2t_C)(w)(L)$	$(t_C)(w)(L)$
Active catalyst volume	$(t_C)(w)(L)$	$(1-\varepsilon_{bed})(2t_C)(w)(L)$	n/a
Membrane surface area	(w)(L)	(w)(L)	(w)(L)

2.2.1 Water-Gas Shift Rate Expression and Permeability Models

Both CCP membrane and PBMR models employ the power-law rate expression developed by Mizsey for the case of the water-gas shift reaction over a 5% CuO-Al_2O_3 catalyst [185],

$$r_{WGS} = \rho_{cat} k_f \left(p_{CO} p_{H_2O} - p_{CO_2} p_{H_2} K_{eq}^{-1}\right) \tag{25}$$

where

$$k_f = 2.25 \times 10^{-3} \exp\left[\frac{-50{,}000}{RT_0}\right] \quad \text{and} \quad K_{eq} = 9.543 \times 10^{-3} \exp\left[\frac{-39{,}876}{RT_0}\right] \tag{26}$$

In both models, a catalyst density of 2.4×10^6 g m^{-3} is assumed [188]. All three models (CCP, PBMR, and GPM) are compared for the case of 1) an infinitely H_2-permselective dense Pd film and 2) a moderately CO_2-permselective polymeric film. For the former case, the modified Sievert's Law model developed by Harold and Israni [189] is employed, assuming infinite permselectivity towards H_2:

$$Q_{H_2}^{Pd} = \left(\frac{P_{H_2}^{Pd}}{t_{Pd}}\right)\left(\theta_{H_2}\sqrt{p_{H_2}^{cat}} - \sqrt{p_{H_2}^{s}}\right), \quad \text{and} \quad Q_{i \neq H_2}^{Pd} = 0 \tag{27}$$

where surface coverage factor, θ_{H_2}, represents the competitive adsorption of reformate species on the feed-side Pd surface,

$$\theta_{H_2} = \frac{1+\sqrt{K_{H_2} p_{H_2}}}{1+\sqrt{K_{H_2} p_{H_2}}+\sqrt{K_{CO} p_{CO}}+K_{H_2O} p_{H_2O}+K_{CO_2} p_{CO_2}} \quad (28)$$

with values of K_{CO} = 1.56 x 10^{-4} Pa^{-1}, K_{H_2O} = 5.44 x 10^{-7} Pa^{-1}, K_{H_2} = 5.56 x 10^{-6} Pa^{-1} and K_{CO_2} = 1.73 x 10^{-7} Pa^{-1} at T = 723.15 K taken from Harold and Israni [189]. Assuming a feed composition of 9% CO, 28% H_2, 15% H_2O and 3% CO_2, the above model predicts a minimum value of θ_{H_2} = 0.447 corresponding to inlet conditions. A Pd permeability of 2.1 × 10^{-9} mol m^{-1} s^{-1} $Pa^{-0.5}$ is assumed, based upon experimental values reported by Kim et al. [190].

A first-order permeation model is employed for the latter case of a moderately CO_2-permselective polymeric membrane, following empirical models demonstrated for amine-based polymer films [165]:

$$Q_i^{Poly} = \frac{1}{\alpha_{CO_2/i}} \left(\frac{P_{co_2}^{Poly}}{t_{Poly}} \right) \left(p_i^{cat} - p_i^{S} \right), \quad (29)$$

where $\alpha_{CO_2/H_2} = 50$, $\alpha_{CO_2/CO} = 100$, $\alpha_{CO_2/N_2} = \alpha_{CO_2/H_2O} = \infty$. The permeability of the polymeric film is assumed to be 1.34 × 10^{-12} mol m^{-1} s^{-1} Pa^{-1}, based upon literature values [165].

2.3 DESIGN OF SIMULATIONS

The geometry of each model (CCP, PBMR, and GPM) is defined in terms of the thickness of the catalyst film employed in the CCP membrane design, t_c. The thickness of the catalyst film is dictated by a design criterion identified previously by Wilhite [168],

specifically that the Thiele Modulus (Φ) associated with reaction-diffusion within the catalyst film must be equal to 7.6. This criterion ensures 99.9% of the maximum possible modification of gas composition at the surface of the permselective film via catalytic reaction. Employing the general definition of the Thiele Modulus with normalizations for second-order kinetics [191] and reversible reaction [192], the following specific design criterion for the present study is obtained:

$$\Phi = t_c \sqrt{\frac{3}{2}} \sqrt{\frac{1+K_{eq}(T_0)}{K_{eq}(T_0)}} \sqrt{\frac{rate_0^{cat}(T_0,P_0) R\, T_0}{D_{CO}^{eff} p_0^{CO}}} = 7.6 \tag{30}$$

Comparison of the CCP and PBMR designs is performed over a range of dimensionless ratios of initial rate of desired permeate (either H_2 or CO_2) transport through the permselective film to initial water-gas shift reaction rate, defined as:

$$\xi = \frac{A_{mem}}{V_{cat}} \frac{Q_i^{Pd,Poly}(p_{i,in}^F, T_0)}{r_{CO}(p_{i,in}^F, T_0)} \qquad \text{where i = } H_2 \text{ or } CO_2 \tag{31}$$

based upon the analysis of packed-bed membrane reactors by Harold et al. [193]. Thus, ξ represents a measure of whether catalytic reaction (ξ > 1) or permeation through the membrane (ξ < 1) is the limiting phenomena within the system. Analysis by Wilhite [168] also identified the dimensionless ratio of desired permeate transport through the permselective film, evaluated under inlet conditions (i.e., prior to catalytic reaction),

$$\zeta = \frac{R\, T_0\, t_c\, Q_i^{Pd,Poly}(p_{i,in}^F, T_0)}{D_i^{eff} p_{i,in}^F} \tag{32}$$

The variable ζ thus quantifies the reduction in membrane permeance, independent of reaction contributions, resulting from the addition of the catalyst layer. As ζ increases, transport resistances associated with the catalyst film relative to that of the underlying

permselective film contribute to a reduction in net permeation rates. Permselective film thicknesses were selected such that performance of CCP, PBMR, and GPM designs are compared over a range of feed and sweep residence times at values of ξ of 0.01-1, corresponding to values of ζ both greater than and less than unity (Table 5). The membrane residence time, or characteristic time for convective transport, can be normalized by the characteristic time for permeation across the membrane to obtain a membrane Peclet number[4] (following the analysis of Moon and Park [194]) that represents the size of the membrane system:

$$\mathrm{Pe} = \frac{\sigma\, \hat{a}^{F} R\, T_0\, Q_i^{Pd,Poly}\left(p_{i,in}^{F}, T_0\right)}{p_{i,in}^{F}} = \mathrm{Da}\, \xi \tag{33}$$

which is related to the dimensionless size of the reactor, or Damköhler number[5], by the ratio of initial permeation to reaction rate (ξ).

Table 5. Model dimensions and corresponding dimensionless design parameters employed in both studies.

	Case I: Pd permselective film				Case II: polymeric permselective film			
t_C (m)	$4.8\text{x}10^{-4}$				$1.2\text{x}10^{-2}$			
Φ	7.6				7.6			
Length (m)	0.15				0.15			
Width (m)	0.001				0.01			
t_{mem} (m)	$8.2\text{x}10^{-5}$	$8.5\text{x}10^{-6}$	$2.8\text{x}10^{-6}$	$8.6\text{x}10^{-7}$	$2.8\text{x}10^{-4}$	$3.0\text{x}10^{-5}$	$8.2\text{x}10^{-6}$	$3.0\text{x}10^{-6}$
ξ	0.01	0.1	0.33	1	0.01	0.1	0.28	1
ζ	0.033	0.3	1	3	0.036	0.36	1	3.6

[4] The Peclet number (Pe) is a dimensionless number representing the ratio of the rate of convection to the rate of diffusion.

[5] The Damköhler number (Da) is a dimensionless number representing the ratio of reaction rate to diffusion/transport rate.

2.4 SIMULATION ANALYSIS

Performance of each design (CCP, PBMR, and GPM) is measured in terms of gas purification metrics appropriate for either selective H_2 removal via Pd permselective film or CO_2 removal via polymeric permselective films. For the case of designs employing an infinitely H_2-permselective Pd film, system performance is measured in terms of H_2 recovery and overall H_2 flux through the membrane, defined as:

$$\%R_{H_2}^{Pd} = \frac{F_{H_2,out}^{S}}{F_{H_2,out}^{F}+F_{H_2,out}^{S}} \qquad \text{and} \qquad Q_{H_2}^{Pd} = \frac{F_{H_2,out}^{S}+F_{H_2,in}^{S}}{A_{mem}} \tag{34}$$

For the case of a moderately CO_2-permselective polymeric film, performance is measured in terms of permeate CO_2 recovery, retentate H_2 recovery, and apparent CO_2/CO and CO_2/H_2 permselectivities.

$$\%R_{CO_2}^{Poly} = \frac{F_{co_2,out}^{S}}{F_{co_2,out}^{F}+F_{co_2,out}^{S}} \quad \text{and} \quad \%R_{H_2}^{Pd} = \frac{F_{H_2,out}^{S}}{F_{H_2,out}^{F}+F_{H_2,out}^{S}} \quad \text{and}$$

$$\alpha_{CO_2/CO}^{Poly} = \frac{p_{CO_2,out}^{S}/p_{CO,out}^{S}}{p_{CO_2,in}^{F}/p_{CO,in}^{F}} \quad \text{and } \alpha_{CO_2/H_2}^{Poly} = \frac{p_{CO_2,out}^{S}/p_{H_2,out}^{S}}{p_{CO_2,in}^{F}/p_{H_2,in}^{F}} \tag{35}$$

Additionally, the CCP and PBMR designs are compared in terms of CO conversion via water-gas shift reaction both for the case of Pd and polymeric permselective films,

$$X_{CO}^{CCP,PBMR} = \frac{F_{CO,in}^{F}-F_{CO,out}^{F}-F_{CO,out}^{S}}{F_{CO,in}^{F}} \tag{36}$$

2.5 NUMERICAL METHODS

Two- and one-dimensional models were implemented using the commercial Finite Element Method (FEM) software COMSOL Multiphysics® version 3.5, equipped with the Chemical Engineering Module. All fluid and catalyst volumes were described employing

coefficient form Partial Differential Equation (PDE) modules. For the two-dimensional CCP design simulation, finite element meshes of approximately 13,000 triangular elements were employed, resulting in ~10^5 degrees of freedom. Further mesh refinement resulted in <0.1% variation in simulation results, validating the accuracy of the mesh. For one-dimensional models, finite element meshes of approximately 2×10^2 points were employed, resulting in ~4×10^3 degrees of freedom. Solutions were obtained using the prepackaged stationary Direct UMFPACK solver (v4.2) written by Timothy A. Davis, with a relative error tolerance 10^{-6} and a maximum number of iterations of 25 [195].

2.6 RESULTS AND DISCUSSION

2.6.1 Case Study I: Infinitely H_2-permselective Pd Film

Simulations were first carried out for the case of H_2 purification from diesel reformate (9 mol% CO, 3 mol% CO_2, 28 mol% H_2, 15 mol% H_2O) assuming an infinitely H_2-permselective Pd film employed in all three configurations (GPM, PBMR, CCP) and accounting for film inhibition via competitive adsorption by CO contaminant. Figure 20 presents a comparison of overall H_2 recovery predicted for each configuration as a function of the membrane Peclet number for the cases of ξ = 0.01, 0.1, 0.3, 1, corresponding to ζ = 0.03, 0.3, 1, 3 respectively. For all values of ξ and ζ investigated, higher H_2 recoveries are predicted for the GPM design as compared to the PBMR design, which may be explained in terms of a difference in H_2 residence times. In both configurations, H_2 present at the reformate inlet experiences identical convective residence time for permeation across the Pd membrane. However, for the latter design one

must also account for recovery of H_2 produced within the membrane reactor by the catalytic reaction; under conditions where intrinsic reaction rates are larger than permeation rates (i.e., $\xi < 1$ in present analysis), H_2 produced via water-gas shift reaction along the length of the reactor experiences significantly shorter convective residence time for gas permeation, resulting in a reduced overall H_2 recovery.

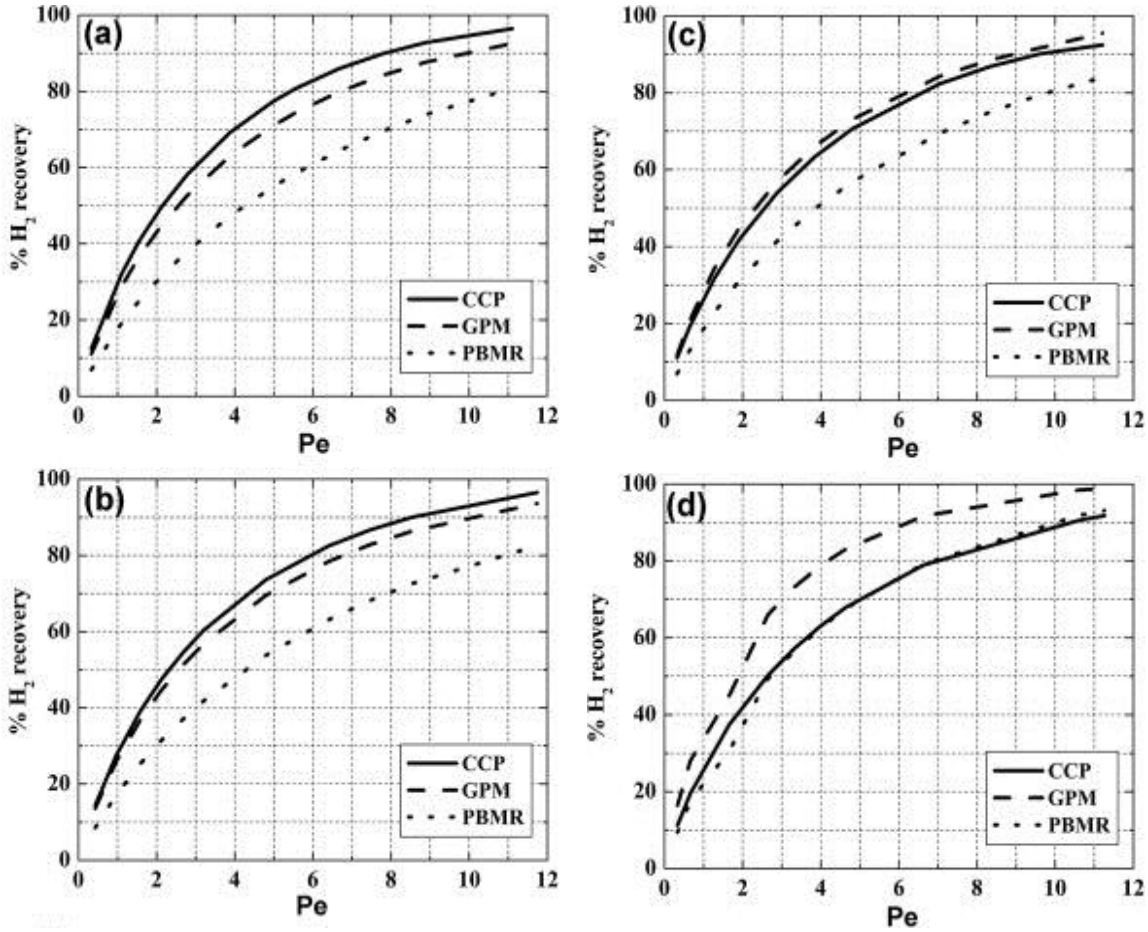

Figure 20. Comparison of $\%H_2$ recovery vs. membrane Peclet number for an infinitely H_2-permselective Pd film employed in a CCP membrane design against equivalent GPM and PBMR designs. (a) $\xi = 0.01$, $\zeta = 0.033$; (b) $\xi = 0.1$, $\zeta = 0.3$; (c) $\xi = 0.33$, $\zeta = 1$; and (d) $\xi = 1$, $\zeta = 3$.

As discussed in Section 2.1, the primary advantage of the CCP design over an untreated permselective film (or GPM design) is the alleviation of film contamination by species consumed by the catalytic film (e.g., methanol or CO). In the present analysis, the catalytic conversion of CO to CO_2 results in a significant reduction in Pd surface inhibition via competitive CO adsorption. This is reflected in the comparison of CCP and GPM H_2 recoveries for the case of $\zeta < 1$, i.e., under conditions corresponding to a high rate of H_2 permeation through the catalyst film relative to that through the Pd film (Figure 20a and b). Under conditions wherein H_2 diffusional resistances within the catalyst film are comparable to resistances within the Pd film ($\zeta > 1$), H_2 recovery achievable by the Pd membrane is reduced upon addition of the catalytic layer (i.e., GPM design outperforms the CCP design).

Comparison of the two catalytic membrane reactor designs (CCP vs. PBMR) indicates a significant improvement in H_2 recovery by introducing the catalyst as a protective washcoating overtop the Pd film (Figure 20a - c). In both cases, WGS reaction reduces CO content along the axial length of the reactor, contributing to increased rates of H_2 permeation via reduction of Pd surface inhibition. For the case of $\xi = 0.01$, corresponding to a rapid initial rate of WGS reaction relative to H_2 permeation, significant inhibition of the Pd film via CO is limited to a narrow inlet region for both cases. Comparison of CCP and PBMR H_2 recoveries under these conditions (Figure 20a) nevertheless indicates considerably higher H_2 recoveries for the former case. This enhancement can be explained in terms of the effective residence time of H_2 produced by WGS reaction within the two membrane reactors. In the CCP design, additional H_2 is

produced by the catalytic reaction within the membrane itself, such that effective residence times for H_2 produced by WGS reaction in the CCP design reflect a combination of convective residence time associated with the feed/retentate fluid and diffusional residence time within the catalytic film. Results in Figure 20c and d indicate that the CCP design achieves greater H_2 recoveries than the PBMR design even under conditions where the catalyst film contributes significant additional resistance to H_2 permeation through the membrane ($\zeta = 1$, Figure 20c), as long as the rate of WGS reaction remains the dominant phenomenon ($\xi < 1$). For the case of identical rates of reaction and H_2 permeation ($\xi = 1$, Figure 20d) corresponding to significant H_2 transport resistance within the CCP membrane ($\zeta = 3$), equivalent H_2 recoveries are predicted for the CCP and PBMR designs.

Simulation results for all three configurations over the range of $\xi = (0.01, 0.1, 0.33, 1)$ and $\zeta = (0.033, 0.3, 1, 3)$ are also compared in terms of overall H_2 flux through the Pd film as a function of driving force for permeation in Figure 21. In all cases studied, the GPM design achieves greater H_2 permeation rates than the PBMR design under equivalent driving force, owing to the disparity in effective residence time for H_2 discussed above. Simulations demonstrate that while $\xi < 1$, the CCP design is capable of achieving higher H_2 flux than the PBMR design at identical driving forces. Likewise, the present analysis indicates that while $\zeta < 1$, the CCP design results in higher H_2 flux through the Pd film as compared to an uncoated Pd film (i.e., GPM design).

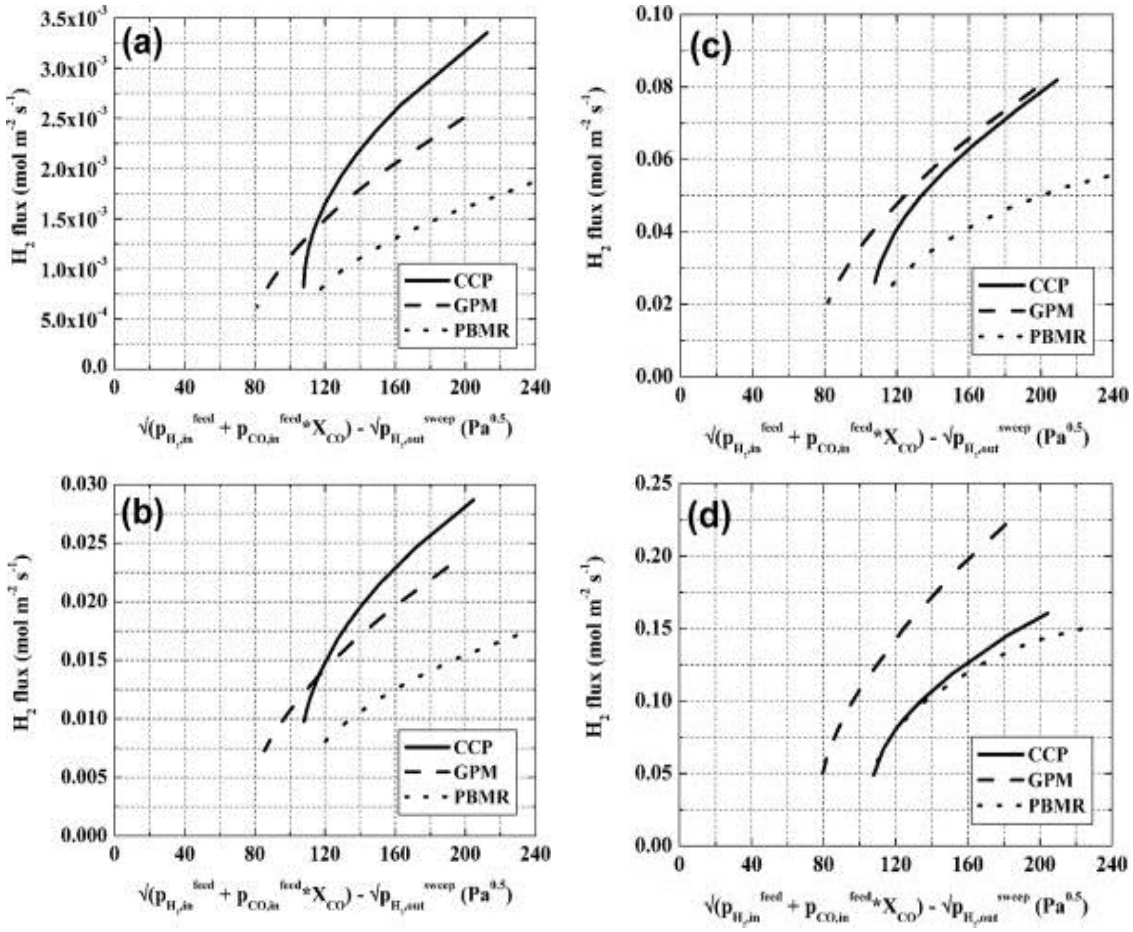

Figure 21. Comparison of H_2 flux vs. driving force for an infinitely H_2-permselective Pd film employed in a CCP membrane design against equivalent GPM and PBMR designs. (a) $\xi = 0.01$, $\zeta = 0.033$; (b) $\xi = 0.1$, $\zeta = 0.3$; (c) $\xi = 0.33$, $\zeta = 1$; and (d) $\xi = 1$, $\zeta = 3$.

Comparison of predicted CO conversions (Figure 22) between the two membrane reactor configurations (CCP and PBMR) reflect the enhanced rate of H_2 permeation discussed above and presented in Figure 20 and Figure 21. For the case of $\xi = 0.01$ (Figure 22a), the CCP design achieves higher CO conversion than the PBMR over the entire span of membrane Peclet numbers studied. This enhancement in WGS reaction rate results from the enhanced rate of product (H_2) removal by the membrane, i.e., Le Chatelier's Principle. As the diffusional resistance to H_2 permeation contributed by the catalytic layer increases

relative to the H_2 permeability of the underlying Pd film in the CCP design (i.e., increasing ζ), higher CO conversions are achievable by the PBMR design. This trend can be explained by comparing effective permeabilities of the un-treated Pd film (GPM design) and the CCP at $\zeta = 1$ (Figures 20c and 21c), which indicate that as ζ increases the effective rate of H_2 removal by the untreated Pd film (in the GPM or PBMR designs) is greater than that of the catalyst-coated film (CCP design).

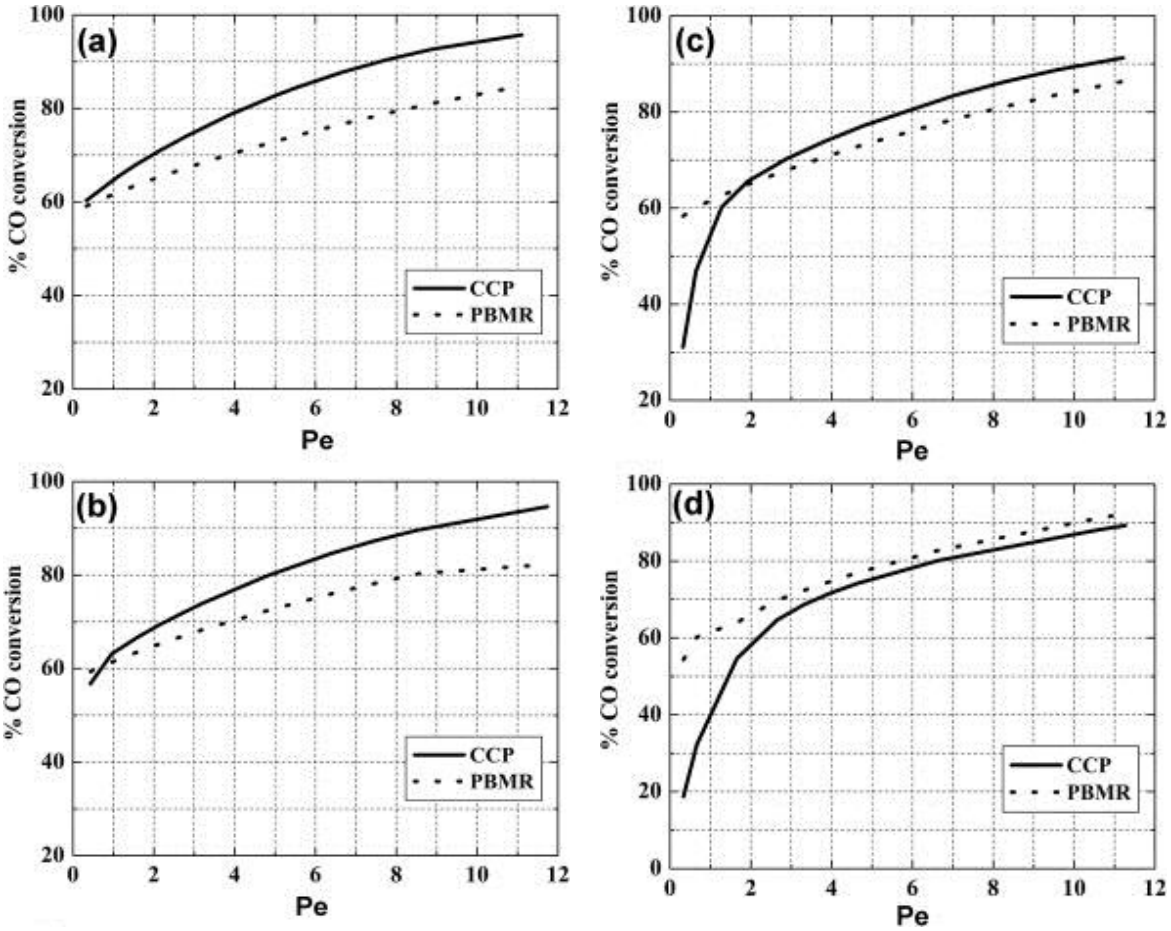

Figure 22. Comparison of CO conversion vs. membrane Peclet number in a CCP membrane design and equivalent PBMR design employing an infinitely H_2-permselective Pd film. (a) $\xi = 0.01$, $\zeta = 0.033$; (b) $\xi = 0.1$, $\zeta = 0.3$; (c) $\xi = 0.33$, $\zeta = 1$; and (d) $\xi = 1$, $\zeta = 3$.

Figure 23 presents a comparison of CO and H_2 partial pressures at the retentate-surface of the Pd film as a function of axial position (z) for all three designs (GPM, PBMR, CCP) corresponding to $\xi = 0.01$ and feed and sweep Peclet numbers of 2 (residence time of 2 s). In both membrane reactor configurations (PBMR, CCP), the WGS reaction provides a substantial reduction in CO content at the Pd surface (Figure 23a). Comparison of Pd surface CO partial pressures for these two designs indicates a narrow inlet region (approximately 2% of the entire axial length) wherein the CCP design achieves significant reduction in CO exposure relative to the PBMR, with mild reduction in CO exposure relative to the PBMR case maintained along the remainder of the axial length. This reduction in surface CO exposure translates into enhanced rates of H_2 permeation for the CCP design, despite a reduction in H_2 partial pressures at the Pd film retentate surface (Figure 23b) arising from the introduction of a catalytic diffusion barrier overtop the Pd film.

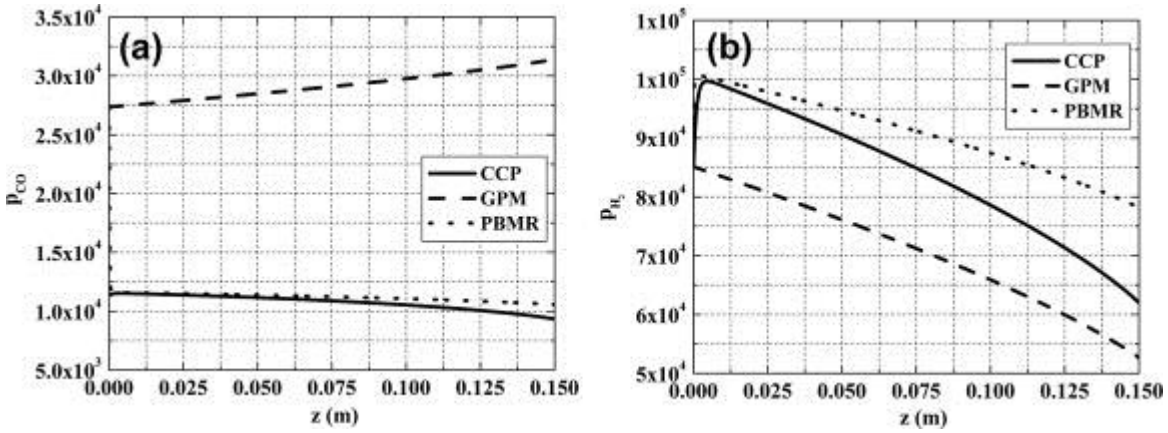

Figure 23. (a) CO and (b) H_2 partial pressures at the retentate surface of an infinitely H_2-permselective Pd film employed in a CCP membrane design and equivalent GPM and PBMR designs operating at feed and sweep residence times of 2 s (Pe = 2), $\xi = 0.01$, $\zeta = 0.03$.

Overall, results obtained for the case of an infinitely H_2-permselective Pd film demonstrate the potential for the CCP design to enhance performance of Pd films employed for H_2 recovery from reformate mixtures when Pd film permeabilities are >7.4 $\times 10^{-3}$ mol m^{-2} $Pa^{-0.5}$ (corresponding to $\zeta < 1$), while indicating that the CCP design is capable of achieving equivalent performance to the PBMR design in micromembrane architectures (Pd film permeabilities <7.4 $\times 10^{-4}$ mol m^{-2} $Pa^{-0.5}$, corresponding to $\xi > 1$). The above analysis assumes an H_2-permselective Pd film susceptible to significant inhibition via competitive surface adsorption of CO. As will be shown in Section 2.6.2 for the case of a finitely permselective membrane in the absence of inhibitory effects, the CCP design may be expected to enhance the product-reactant (H_2-CO) permselectivity at the expense of reducing the product-product (H_2-CO_2) permselectivity.

2.6.2 Case Study II: Moderately CO_2-permselective Polymer Film

Simulations were also carried out for the case of a CO_2-permselective polymeric film with CO_2:CO and CO_2:H_2 permselectivities of 100:1 and 50:1, respectively. By assuming moderate (<200:1) permselectivities (as reported for polymeric membranes), the analysis allows theoretical investigation of whether the CCP design is capable of enhancing overall membrane permselectivities relative to a standalone polymer film (GPM design) or in an equivalent PBMR design. For the case of the polymeric membrane, no inhibition of the permselective film is assumed; thus comparison between the CCP, GPM and PBMR designs is presented in the absence of any potential enhancement of the permselective film via catalytic conversion of CO.

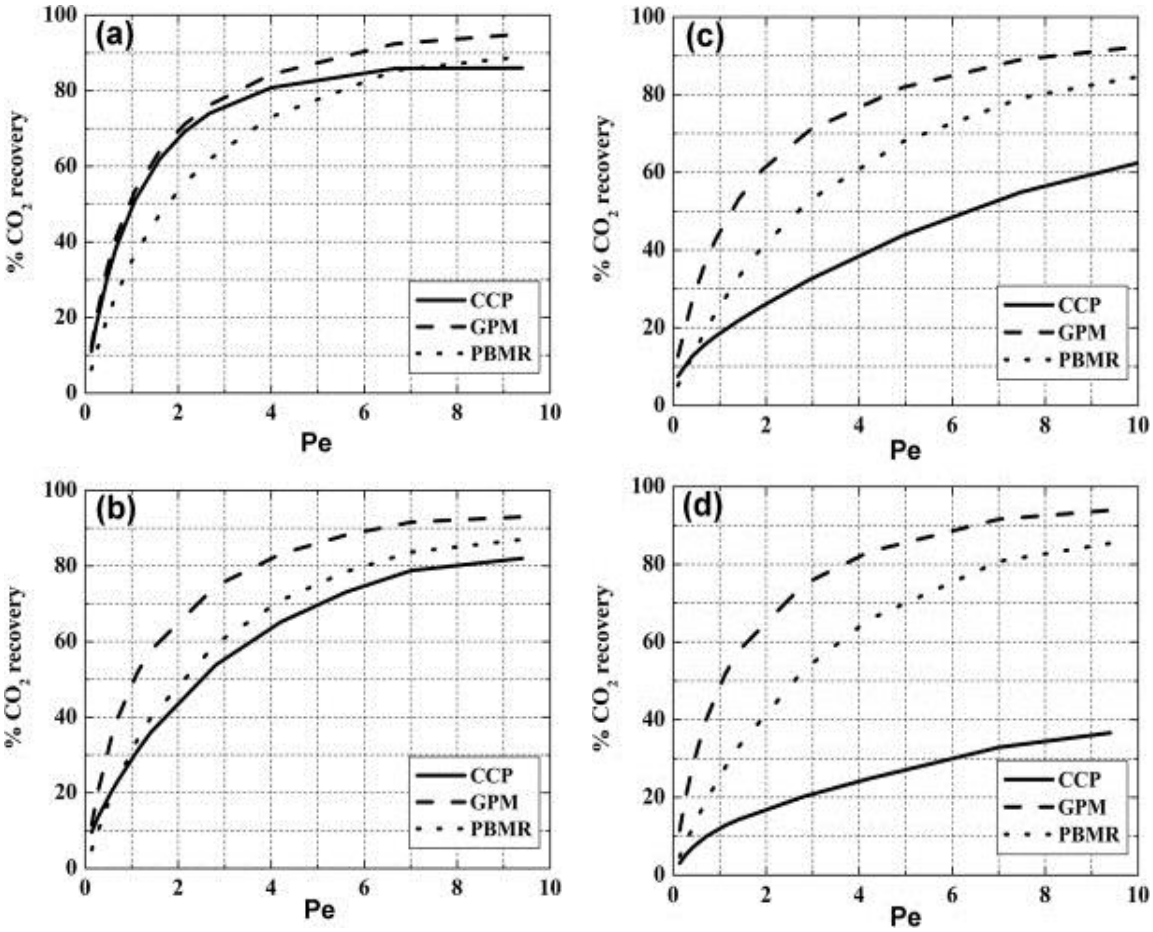

Figure 24. Comparison of %CO_2 recovery vs. membrane Peclet number for a CO_2-permselective polymer film employed in a CCP membrane design against equivalent GPM and PBMR designs. (a) $\xi = 0.01$, $\zeta = 0.036$; (b) $\xi = 0.1$, $\zeta = 0.36$; (c) $\xi = 0.28$, $\zeta = 1$; and (d) $\xi = 1$, $\zeta = 3.6$.

Figure 24 presents comparison of desired permeate (CO_2) recoveries for all three designs (GPM, PBMR, and CCP) at identical feed and sweep residence times at $\xi = 0.01$, 0.1, 0.28, and 1 or $\zeta = 0.036$, 0.36, 1, and 3.6, respectively. In the absence of any anti-inhibition benefits arising from the CCP design, CO_2 recoveries approaching those achieved by a stand-alone polymeric membrane (GPM design) are predicted for the case of $\xi = 0.01$ and $\zeta = 0.036$ (Figure 24a). These conditions correspond to negligible CO_2 diffusional limitations within the catalyst coating relative to polymer film CO_2 permeance.

Under these conditions, the CCP design achieves higher CO_2 recoveries than the PBMR design, owing to the increased residence time for CO_2 produced by the WGS reaction within the catalytic film of the CCP design as compared to CO_2 produced within the pseudo-homogeneous retentate volume of the PBMR design. However, for $\zeta > 0.036$, the CCP design yields significantly lower CO_2 recoveries than either GPM or PBMR designs, as increasing diffusional resistance to CO_2 transport within the catalyst film inhibits CO_2 recovery rates.

For the present case of coupling WGS reaction with a CO_2-permselective polymeric film having finite CO_2:H_2 permselectivities, loss of desired retentate (H_2) via cross-over may reduce overall H_2 recovery. For this reason, a side-by-side comparison of H_2 recovery for all three designs is presented in Figure 25. The increased effective residence time of H_2 produced via WGS reaction in the CCP design, owing to the additional diffusion time imparted by the catalytic film (discussed in Section 2.6.1), is seen to result in significant reduction of H_2 recoveries (owing to greater rate of H_2 permeation) as compared to the PBMR design under all conditions simulated (Figure 25). Likewise, consistently greater H_2 recoveries for the PBMR case relative to the GPM case may be explained in terms of the average residence time of H_2 in the system; for the PBMR case, H_2 produced by catalytic reaction at a point downstream of the membrane inlet experience a shorter residence time and, therefore, a lower rate of H_2 permeation than H_2 supplied at the membrane inlet. The resulting average residence time for H_2 exiting the PBMR is, therefore, less than that of the GPM case, corresponding to a lower rate of H_2 loss due to permeation.

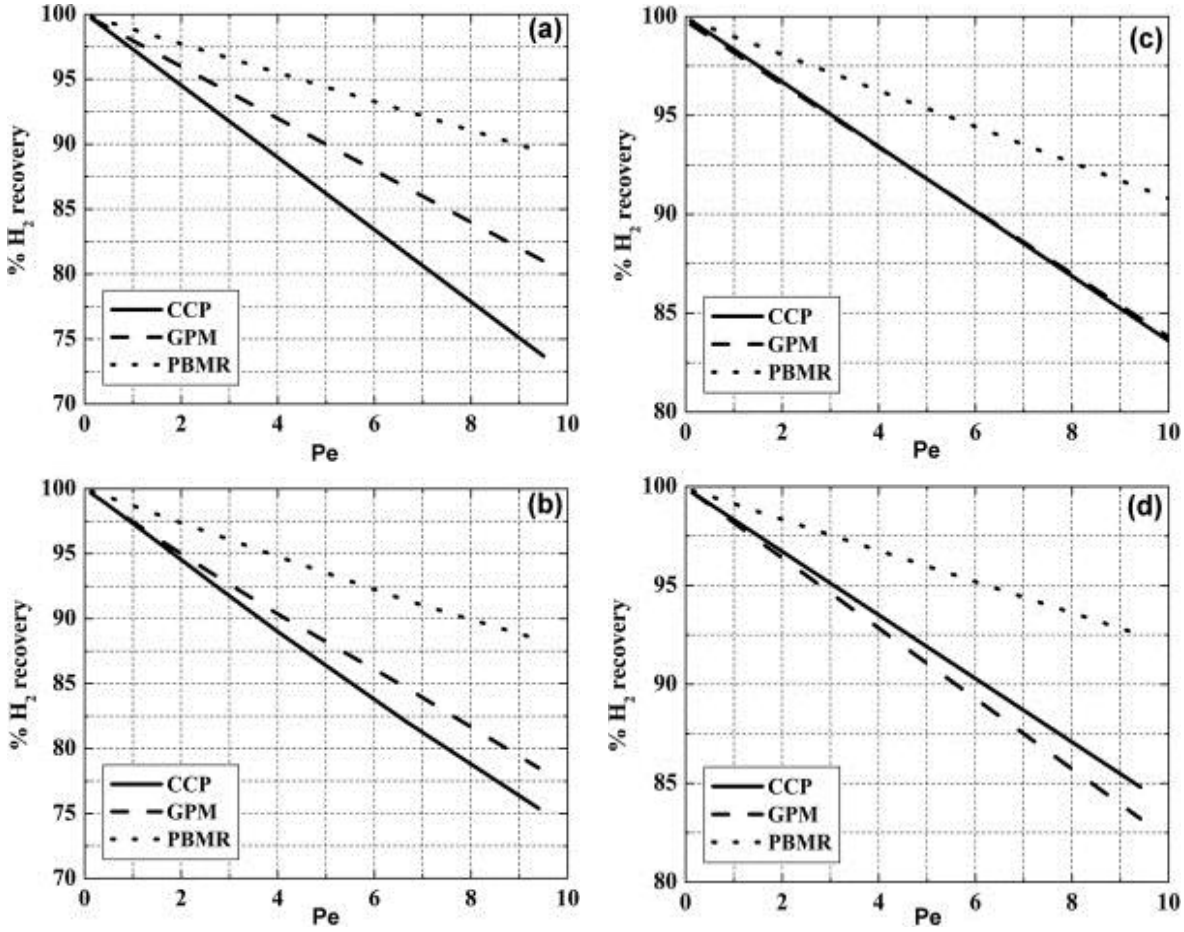

Figure 25. Comparison of $\%H_2$ recovery vs. membrane Peclet number for a CO_2-permselective polymer film employed in a CCP membrane design against equivalent GPM and PBMR designs. (a) $\xi = 0.01$, $\zeta = 0.036$; (b) $\xi = 0.1$, $\zeta = 0.36$; (c) $\xi = 0.28$, $\zeta = 1$; and (d) $\xi = 1$, $\zeta = 3.6$.

Comparison of the two catalytic membrane reactor designs (CCP and PBMR) in terms of CO conversion directly reflects the impact of reactor design upon reaction product (CO_2) removal (Figure 26). Thus, only under conditions where the CCP design is predicted to achieve greater CO_2 recoveries than the PBMR design ($\xi = 0.01$, $\zeta = 0.036$) does the CCP design achieve greater CO conversion. For all other cases, CO_2 diffusional

resistances within the catalytic layer of the CCP membrane reduce overall reaction product recovery and, therefore, CO conversion rates.

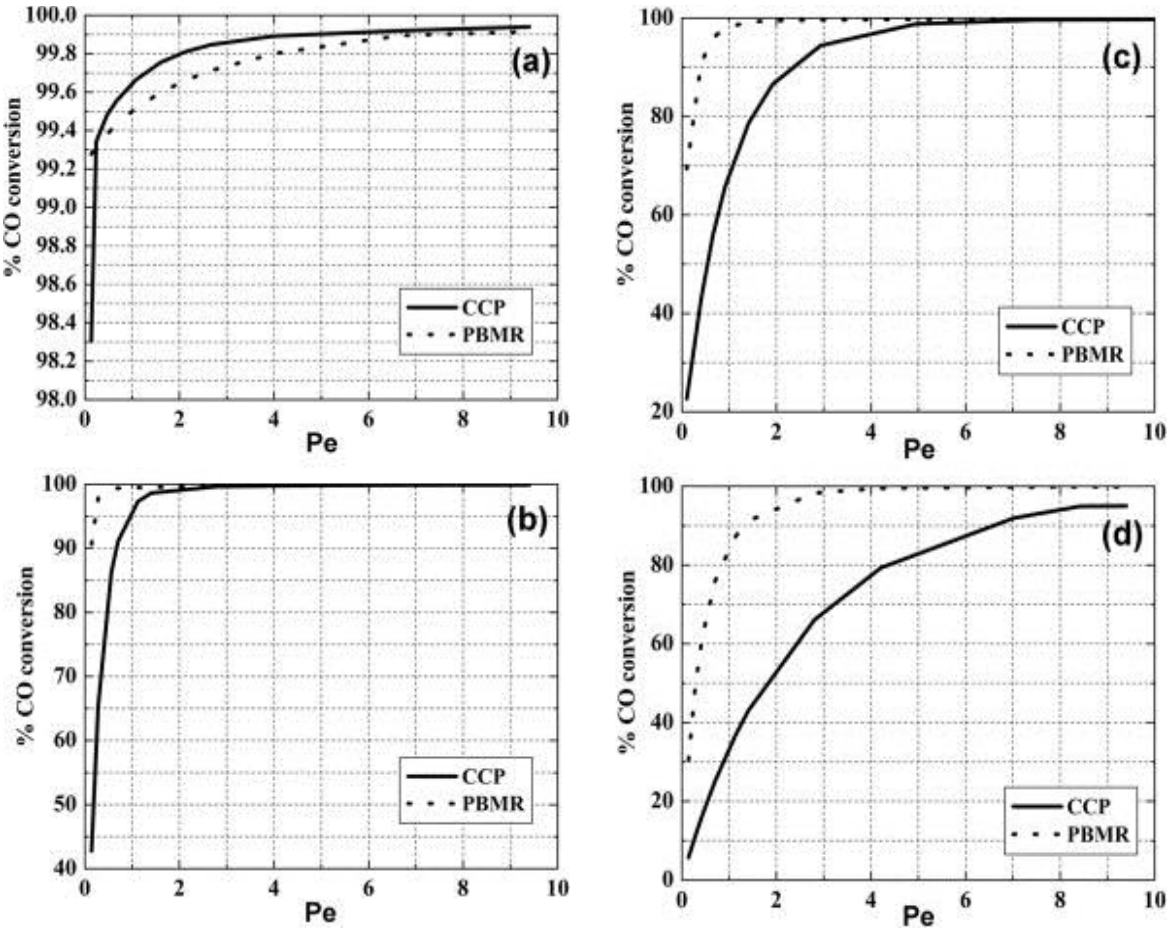

Figure 26. Comparison of CO conversion vs. membrane Peclet number in a CCP membrane design and equivalent PBMR design employing a CO_2-permselective polymer film. (a) $\xi = 0.01$, $\zeta = 0.036$; (b) $\xi = 0.1$, $\zeta = 0.36$; (c) $\xi = 0.28$, $\zeta = 1$; and (d) $\xi = 1$, $\zeta = 3.6$.

Figure 27 presents a side-by-side comparison of the apparent CO_2/H_2 selectivity for the GPM, PBMR, and CCP designs. In the presence of catalytic reaction (CCP and PBMR designs), production of additional CO_2 by WGS reaction results in up to a 3-fold increase in the ratio of CO_2:H_2 partial pressure on the retentate-side of the polymeric

membrane. This results in an optimum membrane residence time or Peclet number for both CCP and PBMR designs corresponding to a maximum apparent CO_2:H_2 permselectivity, with the PBMR consistently achieving greater enhancement in apparent permselectivity than the CCP design. This maximum apparent permselectivity decreases as the flux through the polymeric film increases with respect to the rate of reaction (i.e., increasing ξ). The maximum apparent CO_2:H_2 permselectivity for the PBMR case is greater than the intrinsic permselectivity of the polymeric film for all values of ζ and ξ investigated, while the CCP design results in apparent permselectivies lower than the intrinsic value of the polymer film for the case of significant CO_2 resistance associated with the catalytic layer of the CCP design ($\zeta > 1$, Figure 27d).

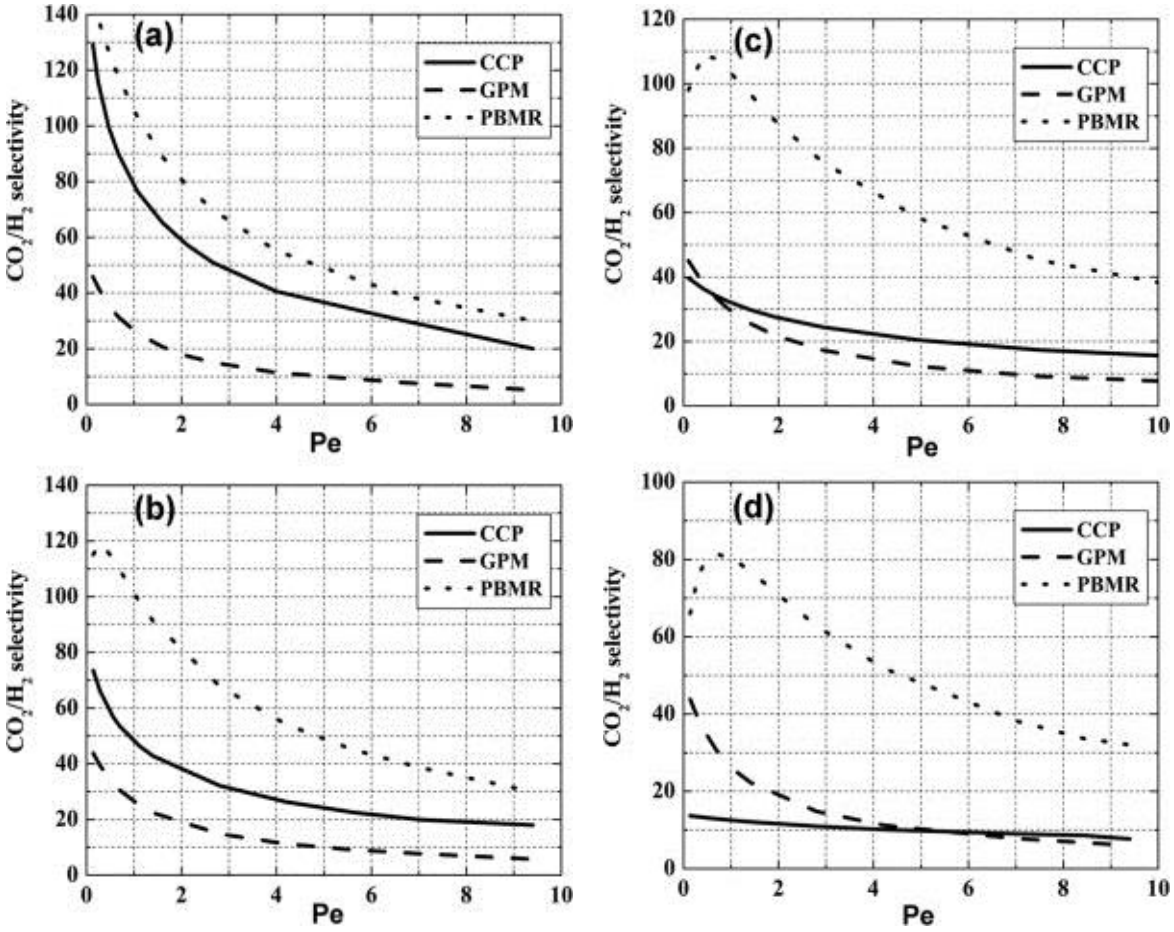

Figure 27. Comparison of CO_2/H_2 apparent permselectivity vs. membrane Peclet number for a CO_2-permselective polymer film employed in a CCP membrane design against equivalent GPM and PBMR designs. (a) $\xi = 0.01$, $\zeta = 0.036$; (b) $\xi = 0.1$, $\zeta = 0.36$; (c) $\xi = 0.28$, $\zeta = 1$; and (d) $\xi = 1$, $\zeta = 3.6$.

Figure 28 presents a comparison of CO_2:CO apparent permselectivities for the GPM, PBMR, and CCP designs. As CO and H_2O are catalytically converted to H_2 and CO_2, both catalytic membrane reactor designs (PBMR and CCP) achieve order of magnitude increases in apparent CO_2:CO permselectivities. The CCP design is consistently capable of up to 40% improvement in CO_2:CO permselectivities as compared to the PBMR design, owing to the reduction in CO partial pressure at the surface of the polymeric film achieved by the catalytic layer. However, for the present case wherein

CO_2:H_2 selectivity is the limiting factor ($\alpha_{CO_2/H_2} = 50:1$, as compared to $\alpha_{CO_2/H_2} = 100:1$), the advantage of enhanced CO_2:CO separation rates achieved by the CCP design must be weighed against the losses in CO_2:H_2 separation and resulting losses in H_2 recovery arising from the CCP design. It remains the topic of a future study to compare GPM, PBMR, and CCP designs employing polymeric membranes over a range of CO_2:CO and CO_2:H_2 permselectivities.

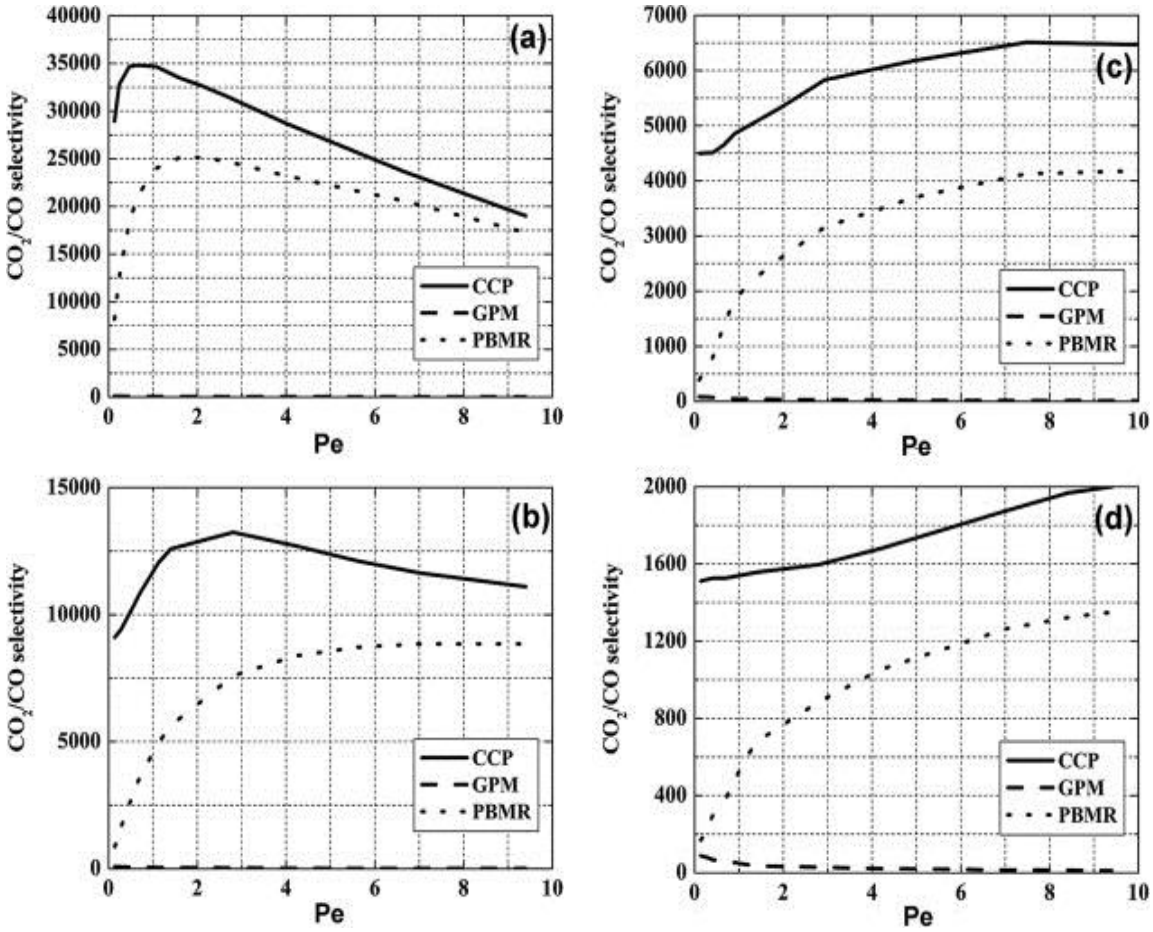

Figure 28. Comparison of CO_2/CO apparent permselectivity vs. membrane Peclet number for a CO_2-permselective polymer film employed in a CCP membrane design against equivalent GPM and PBMR designs. (a) $\xi = 0.01$, $\zeta = 0.036$; (b) $\xi = 0.1$, $\zeta = 0.36$; (c) $\xi = 0.28$, $\zeta = 1$; and (d) $\xi = 1$, $\zeta = 3.6$.

2.7 CONCLUSIONS

The present study provides the first theoretical comparison of the composite catalytic-permselective membrane design against reference cases of 1) an identical permselective film employed in a gas purification membrane system operating in the absence of catalytic reaction, and 2) the same permselective film coupled with catalytic reaction in parallel via packed-bed membrane reactor configuration. By presenting the analysis in terms of two dimensionless design parameters (ξ, ζ) over a range of membrane capacities (Pe), results may be used to determine the catalyst film thickness necessary to achieve permeation and/or permselectivity enhancement via CCP design for a specific set of membrane properties and feed conditions.

Results indicate that the CCP design is capable of significant improvements in overall H_2 recoveries for the coupling of water-gas shift reaction with Pd films, owing to a combination of 1) reduction in CO exposure at the retentate surface of the Pd film and 2) increased holdup of H_2 produced by WGS reaction in close proximity to the permselective film. These improvements are predicted under conditions such that H_2 permeation through the dense Pd film remains the limiting phenomenon for H_2 transport (i.e., $\zeta < 1$). For the present case of WGS reaction coupled with Pd films at 723 K, these conditions correspond to Pd film permeances $<7.4 \times 10^{-3}$ mol m^{-2} $Pa^{-0.5}$, or film thicknesses of the order of 10^{-5} m, as employed in commercial Pd membrane systems; thus, results indicate that the CCP design is a promising route to enhancing the cost effectiveness of industrial Pd-based membrane systems. Model predictions for the case of coupling WGS reaction with a moderately CO_2-permselective ($\alpha_{CO_2/H_2} = 50:1$,

$\alpha_{CO_2/CO} = 100:1$) polymeric film indicate that the CCP design is capable of providing up to a 40% enhancement in CO_2-CO (product-reactant) separation, but at the cost of significant losses in CO_2-H_2 (product-product) separation rates. In the absence of surface inhibition by reactants, the CCP design also limits overall desired permeate recoveries, as compared to equivalent PBMR designs. The present study thus provides a valuable basis for subsequent analysis focused on the parametric sensitivity of permeation and selectivity enhancement to variations in film permselectivity and relative rates of surface inhibition by CO, CO_2, and H_2O.

CHAPTER III

A THEORETICAL COMPARISON OF MULTIFUNCTIONAL CATALYST FOR SORPTION-ENHANCED REFORMING PROCESS

3.1 INTRODUCTION

Sorption-enhanced reforming processes (SERPs) have recently received significant attention due to the growing demands for high-purity H_2 and the escalating costs associated with CO_2 emissions. SERPs combine selective CO_2-adsorption with water-gas shift (WGS) or methane steam reforming (MSR) in a fixed-bed admixture of CO_2 adsorbent and catalyst particles, such that by-product removal of CO_2 from the bulk fluid simultaneously enhances H_2 yields, purifies H_2 product, and captures CO_2 for later utilization or controlled disposal. Although this admixture of CO_2 adsorbent and catalyst particles overcomes equilibrium limitations associated with the WGS and MSR catalytic processes, bed-scale dilution of CO_2 partial pressures limits adsorption rates while intraparticle diffusional limitations hinder catalyst utilization [184]. To address these limitations, multifunctional catalysts that combine adsorptive and catalytic properties at the particle scale have recently garnered interest.

Albercht et al. [196] fabricated small spherical pellets comprised of an adsorbent core encased in a porous shell made largely of sintered alumina that supported a nickel catalyst. Sorption-enhanced water-gas shift (SEWGS) reaction testing over a temperature range of 550 °C - 650 °C and a pressure range of 1.0 atm - 10.0 atm showed that these pellets were capable of producing hydrogen at or near thermodynamic equilibrium levels

during a period when CO_2 was being rapidly adsorbed by the core material. A product stream with 98 mol% H_2 (dry basis) was produced during the rapid CO_2 adsorption period of each cycle. Solsvik and Jakobsen [197] and Rout et al. [198] studied the performance of a combined catalyst-adsorbent pellet design for the sorption-enhanced methane steam reforming (SEMSR) process. In their spherical pellet, sorptive and catalytic functionalities were uniformly distributed in the particle. Their results demonstrated that the uniform-distributed pellet design is able to obtain higher values of catalyst effectiveness factors relative to that of the conventional design where the catalyst and adsorbent properties are separated into two pellet types.

Optimal distribution of catalytic properties within a single mono-functional catalyst particle is a well-established strategy for exploiting diffusional and thermal limitations to maximize catalyst efficiency [5, 199]. Previous work (Chapter I) successfully extended this concept for enhancing gas membrane separation performance using a bi-functional composite catalytic-permselective (CCP) membrane design, wherein a thick catalyst layer is washcoated over the retentate surface of a permselective film, such that undesired contaminants are catalytically destroyed before reaching the permselective surface. Likewise, the catalytic production of desired permeate species in close proximity to the permselective surface further enhances gas permeation rates. Two-dimensional simulations of the WGS reaction coupled with permselective H_2 removal demonstrated a significant enhancement in membrane permeation rates due to a combination of enhancement in local driving force for permeation and reduction in CO surface inhibition using the CCP design, as compared to the equivalent packed-bed membrane reactor and

the gas purification membrane design [166]. This enhancement was experimentally confirmed using a 30-micron palladium membrane coated with a 500-micron 13 wt% CuO/Al_2O_3 catalyst layer [167]. Based upon these findings the objective of the present work is to investigate if previous observations of sequentially structured patterning of functionalities can be extended into the unsteady-state sorption-enhanced process for WGS and MSR.

From the above review, the integration of catalytic and separation functionalities at the particle-scale is a promising means of improving the performance of SEWGS and SEMSR processes. While previous analysis suggests that for mass transfer limiting cases, a core-shell (or segregated) design (Figure 29a) may be preferable to a uniform-distributed design (Figure 29b), a direct comparison of these two designs is lacking. The purpose of this work is to provide the first side-by-side comparison of these two multifunctional catalyst designs.

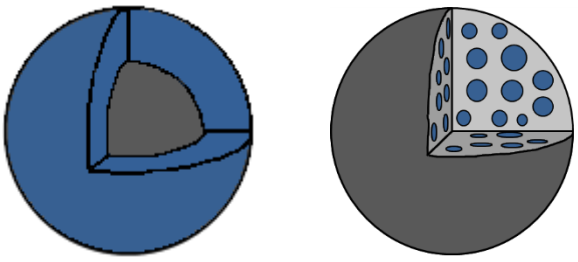

(a) **(b)**

Figure 29. Schematic of the two multifunctional catalyst designs considered in this study. (a) the core-shell design and (b) the uniform-distributed design.

3.2 MODEL DEVELOPMENT

Two-dimensional unsteady-state models were developed to compare the performance of the core-shell design and the uniform-distributed design. Core-shell multifunctional catalyst pellets consist of a calcium-based adsorbent core enclosed in a porous shell of MSR or WGS catalyst. Uniform-distributed multifunctional catalyst pellets, on the other hand, are spherical pellets in which adsorbent and catalyst are uniformly distributed. Comparison is provided in the context of typical particle dimensions and adsorbent-to-catalyst volume ratios reported in the literature for SEWGS and SEMSR processes.

A two-phase (gas-solid) dispersion model describing the dynamic behavior of a fixed-bed reactor was developed for comparing the multifunctional catalyst designs. Although the fluidized-bed reactor concept is believed to be more appropriate, several studies in the literature have used a fixed-bed reactor for sorption-enhanced reforming processes [180, 196, 197, 200, 201].

3.2.1 Particle Equations: Multifunctional Catalyst Pellet

All simulations assumed spherical pellets of constant diameter (d_p). Particle dimensions were selected to enable comparison at identical catalyst and adsorbent volumes. In a porous media, the general mass balance equation for species *i* in the reacting fluid is written as:

$$\epsilon \frac{\partial}{\partial t}(cx_i) = -\nabla \cdot N_i + r_i \tag{37}$$

where r_i represents the consumption or production rate of species *i* and N_i is the molar flux, which is described using the Dusty-Gas Model (DGM) [202]:

$$\sum_{j=1,\ j\neq i}^{n} \frac{x_i N_j - x_j N_i}{D_{ij}} - \frac{N_i}{D_{i,k}} = \frac{P}{RT}\nabla x_i + \frac{x_i}{RT}\left(1 + \frac{B_0 P}{\mu D_{i,k}}\right)\nabla P \tag{38}$$

where D_{ik} and D_{ij} represent the Knudsen and binary diffusivities, respectively. These diffusivities are estimated using Equations 17 and 18 (Section 2.2). A detailed description of the DGM model implementation is presented in Appendix A.

The fluid permeability of the catalyst film is calculated as follows:

$$B_0 = \frac{d_p^2 \epsilon}{32\tau} \tag{39}$$

where ϵ and τ are the particle porosity and tortuosity, respectively. A pellet porosity of 45% is assumed, with nominal pore diameter of 10 nm and tortuosity of 2 [187].

The source term (r_i) in the mass balance equation (Equation 37) depends on the distribution of the functionalities (core-shell or uniform-distributed) within the pellet. The source terms of both designs are given below [197]:

$$r_i = \begin{cases} \frac{1-\epsilon}{1+\alpha}\rho_{cat} r_{cat} + \frac{1-\epsilon}{1+\frac{1}{\alpha}}\rho_{sor}\, r_{sor} & \text{Uniform} - \text{distributed} \\ (1-\epsilon)\ \rho_{cat}\, r_{cat} & \text{Core} - \text{shell (catalyst)} \\ (1-\epsilon)\,\rho_{sor}\, r_{sor} & \text{Core} - \text{shell (adsorbent)} \end{cases} \tag{40}$$

where α represents the adsorbent-to-catalyst volume ratio. The term r_{sor} is equal to zero for all species except for CO_2.

The continuity equation can be obtained by summation of all individual species mass balances:

$$\epsilon\frac{\partial c}{\partial t} = \sum_i r_i \tag{41}$$

Water-gas shift and methane steam reforming were investigated as candidate reaction systems for comparing the performance of the uniform-distributed design and the

core-shell design. The water-gas shift reaction is described using the power-law rate expression developed by Hla et al. [203] for an iron-chromium based catalyst, assuming a catalyst density of 2600 kg m^{-3} [188].

$$r_{WGS} = F_{press}\, k_f\, P_{CO}^{0.9}\, P_{H_2O}^{0.31}\, P_{CO_2}^{-0.156}\, P_{H_2}^{-0.05} \left(1 - \frac{1}{K_{eq}} \frac{P_{CO_2} P_{H_2}}{P_{CO} P_{H_2O}}\right) \tag{42}$$

where F_{press} is a pressure scale-up factor [204] and k_f and K_{eq} are the rate and equilibrium constants defined as [203]:

$$k_f = 10^{0.659} \exp\left(\frac{-88{,}000}{RT}\right) \quad \text{and} \quad K_{eq} = 1.767 \times 10^{-2} \exp\left(\frac{4{,}400}{T}\right) \tag{43}$$

The methane steam reforming process is modeled using a Langmuir-Hinshelwood-Hougen-Watson rate expression, originally developed by Xu and Froment [205].

$$r_{MSR} = \frac{\frac{k_{MSR}}{p_{H_2}^{2.5}} \left(p_{CH_4}\, p_{H_2O} - \frac{p_{H_2}^3 p_{CO}}{K_{eq,MSR}}\right)}{\left(1 + K_{CO} p_{CO} + K_{H_2} p_{H_2} + K_{CH_4} p_{CH_4} + \frac{K_{H_2O} p_{H_2O}}{p_{H_2}}\right)^2} \tag{44}$$

$$r_{WGS} = \frac{\frac{k_{WGS}}{p_{H_2}} \left(p_{CO}\, p_{H_2O} - \frac{p_{H_2} p_{CO_2}}{K_{eq,WGS}}\right)}{\left(1 + K_{CO} p_{CO} + K_{H_2} p_{H_2} + K_{CH_4} p_{CH_4} + \frac{K_{H_2O} p_{H_2O}}{p_{H_2}}\right)^2} \tag{45}$$

$$r_{MET} = \frac{\frac{k_{MET}}{p_{H_2}^{3.5}} \left(p_{CH_4} p_{H_2O}^2 - \frac{p_{H_2}^4 p_{CO_2}}{K_{eq,MET}}\right)}{\left(1 + K_{CO} p_{CO} + K_{H_2} p_{H_2} + K_{CH_4} p_{CH_4} + \frac{K_{H_2O} p_{H_2O}}{p_{H_2}}\right)^2} \tag{46}$$

where rate coefficients (k_j), individual species adsorption coefficients (K_i), and reaction equilibrium coefficients ($K_{eq,i}$) are described by Equations 47 and 48. Pre-exponential and exponential values employed in the present work are summarized in Table 6.

$$k_j = k_{j,0} \exp\left(\frac{-E_{a,j}}{RT}\right) \quad \text{and} \quad K_i = K_{i,0} \exp\left(\frac{\Delta H_i}{RT}\right) \tag{47}$$

$K_{eq,MSR} = 1.198 \times 10^{17} \exp\left(\frac{-26{,}830}{T}\right)$, $K_{eq,WGS} = 1.767 \times 10^{-2} \exp\left(\frac{4{,}400}{T}\right)$, and

$$K_{eq,MET} = 2.117 \times 10^{15} \exp\left(\frac{-22{,}430}{T}\right) \quad (48)$$

Table 6. Kinetic parameters employed to describe reaction rates of MSR process based on the study by Xu and Froment [205].

Pre-exponential		Exponential	
$k_{MSR,0}$	4.22×10^{15} kmol bar$^{0.5}$ kg^{-1} cat h^{-1}	$E_{a,MSR}$	240.1 kJ mol^{-1}
$k_{WGS,0}$	1.95×10^{6} kmol bar^{-1} kg^{-1} cat h^{-1}	$E_{a,WGS}$	67.13 kJ mol^{-1}
$k_{MET,0}$	1.02×10^{15} kmol bar$^{0.5}$ kg^{-1} cat h^{-1}	$E_{a,MET}$	243.9 kJ mol^{-1}
$K_{CO,0}$	8.23×10^{-5} bar^{-1}	ΔH_{CO}	-70.7 kJ mol^{-1}
$K_{CH_4,0}$	6.65×10^{-4} bar^{-1}	ΔH_{CH_4}	-38.3 kJ mol^{-1}
$K_{H_2O,0}$	1.77×10^{5} bar^{-1}	ΔH_{H_2O}	88.7 kJ mol^{-1}
$K_{H_2,0}$	6.12×10^{-9} bar^{-1}	ΔH_{H_2}	-82.9 kJ mol^{-1}

A mathematical model describing the gas-solid reaction of CaO and CO_2 is given by Stendardo and Foscolo, assuming an adsorbent density of 2500 kg m^{-3} [175].

$$r_{sor} = \frac{dX}{dt} N_{Ca}\left(1 - c\, x_{CO_2} V_{CaO}(Z-1)\right) \quad (49)$$

$$\frac{dX}{dt} = \frac{\sigma_{0,CaO}(1-X)^{2/3}\left(c_{CO_2} - c_{CO_2,eq}\right)}{1+\frac{N_{Ca} k_S}{2D_{PL}}\delta_{CaO}\sqrt[3]{1-X}\left(1-\sqrt[3]{\frac{1-X}{1-X+XZ}}\right)} \quad (50)$$

$$\epsilon(X) = \epsilon_0 - N_{Ca} V_{CaO}(Z-1)X \quad (51)$$

where X is the extent of solid adsorbent conversion, N_{Ca} is the number of moles of calcium per unit volume of adsorbent particle, V_{CaO} is the molar volume of CaO, Z is the molar volume ratio of V_{CaCO3} to V_{CaO}, D_{PL} is the product layer diffusion coefficient, and ϵ_0 is the initial particle porosity.

The equilibrium pressure of carbon dioxide (in atm) in the gaseous phase is given as a function of temperature by Stanmore and Gilot [206].

$$P_{CO_2,eq} = 4.137 \times 10^{7} \exp\left(\frac{-20474}{T}\right) \qquad \therefore c_{CO_2,eq} = \frac{P_{CO_2,eq}}{RT} \quad (52)$$

Although the kinetics of the catalytic reactions and the CaO-CO_2 reaction were developed independently, in this study, it is assumed that these kinetic expressions can be used within the same particle without further modification. To the best of our knowledge, no kinetic information for the combined system is available in the open literature.

Pure component viscosities were calculated using Equations 53 to 56, where T* is $\kappa T/\varepsilon$ with T in K and ε/κ being a Lennard Jones parameter of units K. σ_i is a Lennard Jones parameter in Angstroms and M_i is the molecular weight in g mol^{-1}. The calculated viscosity has units of g cm^{-1} s^{-1} [207, 208]. Lennard-Jones parameters employed in Equations 55 and 61 are presented in Table 7.

$$\mu_{mix} = \sum_{i=0}^{n} \frac{x_i \mu_i}{x_i + \sum_{j=1}^{n} \Theta_{ij}} \tag{53}$$

$$\Theta_{ij} = \frac{\left[1+\left(\frac{\mu_i}{\mu_j}\right)^{1/2}\left(\frac{M_j}{M_i}\right)^{1/4}\right]^2}{\sqrt{8}\left(1+\frac{M_i}{M_j}\right)^{1/2}} \tag{54}$$

$$\mu_i = 2.6693 \times 10^{-5} \frac{\sqrt{M_i T}}{\sigma_i^2 \Omega_\mu} \tag{55}$$

$$\Omega_\mu = \frac{1.16145}{T^{*0.14874}} + \frac{0.52487}{\exp(0.77320\, T^*)} + \frac{2.16178}{\exp(2.43787\, T^*)} \tag{56}$$

Table 7. Lennard-Jones parameters used in calculating individual species viscosities (Equation 55) and thermal conductivities (Equation 61).

Species	σ_i (Å)
H_2	2.915
N_2	3.667
CO	3.590
CO_2	3.996
CH_4	3.780
H_2O	3.165

The heat transport within the particles is described by the following one-dimensional equation:

$$\left[(1-\epsilon_P)C_{p,s}\rho_s + \epsilon C_{p,mix}\rho_{mix}\right]\frac{\partial T}{\partial t} = -\nabla \cdot Q_r + r_T \tag{57}$$

$$Q_r = -\left[(1-\epsilon)k_s + \epsilon_P k_{mix}\right]\frac{\partial T}{\partial r} \tag{58}$$

where the k_s and k_{mix} are the solid and gas mixture conductivities, respectively. The specific heat of the fluid phase is calculated using a mol-weighted average of individual species specific heats, while thermal conductivity is calculated from individual species thermal conductivities as [209, 210]:

$$k_{mix} = \sum_{i=0}^{n} \frac{x_i k_i}{x_i + \sum_{j=1}^{n} \Theta_{ij}} \tag{59}$$

$$\Theta_{ij} = \frac{\left[1+\left(\frac{k_i}{k_j}\right)^{1/2}\left(\frac{M_j}{M_i}\right)^{1/4}\right]^2}{\sqrt{8}\left(1+\frac{M_i}{M_j}\right)^{1/2}} \tag{60}$$

$$k_i = 1.9891 \times 10^{-4}\frac{\sqrt{T/M_i}}{\sigma_i^2 \Omega_k} \tag{61}$$

$$\Omega_k = \frac{1.16145}{T^{*0.14874}} + \frac{0.52487}{\exp(0.77320\,T^*)} + \frac{2.16178}{\exp(2.43787\,T^*)} \tag{62}$$

In the same way as for the species mass balance, the source term in Equation 57, r_T, depends on the distribution of the functionalities within the pellet, as defined in Equation 63:

$$r_T = \begin{cases} \frac{1-\epsilon}{1+\alpha}\rho_{cat}\sum(\Delta H_r)\, r_{cat} + \frac{1-\epsilon}{1+\frac{1}{\alpha}}\,\rho_{sor}\, r_{sor}(\Delta H_r) & \text{Uniform} - \text{distributed} \\ (1-\epsilon)\ \rho_{cat}\sum(\Delta H_r)\ r_{cat} & \text{Core} - \text{shell (catalyst)} \\ (1-\epsilon)\,\rho_{sor}\, r_{sor}(\Delta H_r) & \text{Core} - \text{shell (adsorbent)} \end{cases} \tag{63}$$

The gas-solid mass and heat transfer coefficients are calculated using correlations reported by Wakao and Funazkri [211]:

$$\mathrm{Sh} = 2 + 1.1(\mathrm{Sc})^{1/3}(\mathrm{Re_p})^{0.6} \tag{64}$$

$$\mathrm{Sh} = \frac{\mathrm{D_m}}{\mathrm{k_{gs}\, d_p}} \tag{65}$$

and,

$$\mathrm{Nu} = 2 + 1.1(\mathrm{Pr})^{1/3}(\mathrm{Re_p})^{0.6} \tag{66}$$

$$\mathrm{Nu} = \frac{\mathrm{k_{mix}}}{\mathrm{h_f\, d_p}} \tag{67}$$

The boundary conditions for the mass and heat balance equations are derived assuming a symmetric profile within the particles:

$$\left.\begin{matrix}\mathrm{N_{i,r}} = 0 \\ \mathrm{Q_r} = 0\end{matrix}\right\} \text{ for } \mathrm{r} = 0 \quad \text{and} \quad \left.\begin{matrix}\mathrm{N_{i,r}} = \mathrm{k_{gs}}\left(\mathrm{x_i c} - \mathrm{c_{i,fluid}}\right) \\ \mathrm{Q_r} = \mathrm{h_f}\left(\mathrm{T_{fluid}} - \mathrm{T_p}\right) \\ \mathrm{c} = \mathrm{c_{fluid}}\end{matrix}\right\} \text{ for } \mathrm{r} = \mathrm{r_p} \tag{68}$$

The initial conditions are as follows:

$$\left.\begin{matrix}\mathrm{x_i} = 0 \\ \mathrm{T} = \mathrm{T_0} \\ \mathrm{c} = 0 \\ \mathrm{X} = 0\end{matrix}\right\} \text{ for } \mathrm{t} = 0, \forall \mathrm{r} \tag{69}$$

For the SEWGS case, the initial reactor temperature and pressure are 600 °C and 28 bar, respectively [179]. An inlet flow composition of 10 mol% CO, 50 mol% H_2, 32 mol% H_2O, 5 mol% CO_2, balance with nitrogen is fed to the reactor in all simulations [212]. For SEMSR case, the initial reactor temperature and pressure are 650 °C and 15 bar, respectively. All simulations were performed using a steam to methane molar ratio of 3:1 [213].

3.2.2 Gas Bulk Equations

A transient one-dimensional model with axial dispersion is used to describe the reactor fluid phase. The mass transport equation, assuming ideal plug-flow, is given as:

$$\varepsilon_{bed}\frac{\partial c_{i,fluid}}{\partial t}+\frac{\partial}{\partial z}\left(c_{i,fluid}\,u\right)=\frac{\partial}{\partial z}\left(\varepsilon_{bed}D_{z,i}\frac{\partial c_{i,fluid}}{\partial z}\right)+S_i \tag{70}$$

where $D_{z,i}$ represents the axial dispersion coefficients and are calculated as [214]:

$$D_{z,i}=0.73D_{im}+\frac{0.5ud_p}{1+9.49D_{im}/(ud_p)} \tag{71}$$

The source term, S_i, is given as:

$$S_i=a_{v,p}k_{gs}\left(c_{i,p}-c_{i,fluid}\right) \tag{72}$$

where k_{gs} is the gas-solid mass transfer coefficient calculated using Equation 65.

The one-dimensional heat balance equation is given as:

$$\left(\rho_{mix}C_{p,mix}\varepsilon_{bed}+\rho_s C_{ps}\right)\frac{\partial T_{fluid}}{\partial t}+\rho_{mix}uC_{p,mix}\frac{\partial T_{fluid}}{\partial z}=\frac{\partial}{\partial z}\left(k_z\frac{\partial T_{fluid}}{\partial z}\right)+S_T \tag{73}$$

where k_z represents the effective axial bed conductivity and is calculated using correlations given by Yagi et al. [215]. The source term in Equation 73 (S_T) is given as:

$$S_T=a_{v,p}h_f\left(T_p-T_{fluid}\right) \tag{74}$$

The reactor initial and boundary conditions are as follows:

$$\left.\begin{matrix}D_{z,i}\frac{\partial c_{i,fluid}}{\partial z}=u\left(c_{i,fluid}-c_{0,i}\right)\\ T_{fluid}=T_0\end{matrix}\right\}\ \text{at } z=0 \quad \text{and} \quad \left.\begin{matrix}\frac{\partial c_{i,fluid}}{\partial z}=0\\ \frac{\partial T_{fluid}}{\partial z}=0\end{matrix}\right\}\ \text{at } z=L \tag{75}$$

$$\left.\begin{matrix}c_i=0\\ T=T_0\end{matrix}\right\}\ \text{for } t=0,\forall z \tag{76}$$

3.3 DESIGN OF SIMULATION

Bed-scale unsteady-state simulations of the core-shell design and the uniform-distributed design were performed over a range of particle dimensions from 1.0 mm to 8.0 mm. The normalized Thiele Modulus (Φ_c) was calculated using the catalyst-shell thickness of the core-shell design (t_c) and employing the general definition of the Thiele Modulus with normalizations for shape, second-order kinetics [191], and reversible reaction [192]:

$$\Phi_c = t_c \frac{1}{3}\sqrt{\frac{3}{2}} \sqrt{\frac{1+K_{eq}(T_0)}{K_{eq}(T_0)}} \sqrt{\frac{r_i(p_{i,0},T_0)\, RT_0}{D_i^{eff} p_{i,0}}} \tag{77}$$

A dimensionless ratio of the expected rate of CO_2 diffusion through the catalyst shell to the rate of CO_2 sorption at the catalyst-adsorbent interface, ζ, is defined as follows:

$$\zeta = \frac{{t_c}^2}{D_{CO_2}^{eff}} \left(\frac{cCO_{2,0}}{r_{cap}(pCO_{2,0},T_0)} \right)^{-1} \tag{78}$$

The parameter ζ represents the reduction in CO_2 transport to sorbent surface arising from the presence of the outer catalyst shell at initial (t = 0) conditions. As the radius of active CaO decreases over time, the diffusion length (t_c) necessary for CO_2 to reach the CaO increases linearly, while the surface area and, therefore, the surface reaction rate, decreases with t_c^{-2}. Thus, values for ζ are expected to decrease with time and a shrinking core of unreacted CaO.

Previous analysis by Romero and Wilhite [166] employing a composite catalytic-permselective membrane showed that as ζ decreases, a layered structure (analogous to the core-shell design) is favored over a packed-bed membrane reactor configuration (analogous to the uniform-distributed design). Therefore, the present comparison between

the core-shell and uniform-distributed designs is performed over a range of catalyst-shell Thiele Modulus and dimensionless ratio ζ, similar to the values employed in the previous CCP analysis (0.01 – 1). Comparison is also performed over a range of sorbent-to-catalyst volume ratio (α) from 2 to 8 in order to identify the range of conditions under which each design is favored.

Finally, the adsorbent Damköhler number is defined based on initial rate of CO_2 capture at bulk inlet fluid conditions and CO_2 residence time as [159]:

$$\mathrm{Da_{sor}} = \frac{\mathrm{r_{cap}(p_{CO_{2,0}}, T_0)}}{\mathrm{cCO_{2,0}}}\ \theta \tag{79}$$

An adsorbent Damköhler number of 350 was selected in all simulations to clearly present both pre-breakthrough and post-breakthrough regimes. Lower values of Damköhler number typically resulted in CO_2 bypassing the reactor and very short (almost undetectable) pre-breakthrough periods.

3.3.1 Analysis of Simulation Results

The performance of each multifunctional design is measured in terms of adsorbent utilization at the breakthrough time. For this analysis, the breakthrough point is the time when the outlet CO_2 concentration exiting the reactor is equivalent to 5% of the equilibrium CO_2 concentration expected solely by catalytic reaction at the designated temperature and pressure. Beyond this point, the carbonation reaction is considered to be insufficient due to $CaCO_3$ formation on active CaO grains.

Steady-state catalyst effectiveness is generally defined as:

$$\eta = \frac{\text{actual rate of reaction}}{\text{rate of reaction at bulk fluid conditions}} \tag{80}$$

Theoretical catalyst effectiveness for the uniform-distributed design and the core-shell design are calculated as:

$$\eta = \frac{\tanh\Phi}{\Phi} \qquad \text{Uniform-distributed design} \quad (81)$$

$$\eta = \frac{\frac{1}{\Phi^2}\left\{(R_1-R_2)[R_2-R_1u_0]-\Phi R_1R_2\frac{1}{\sinh(\Phi)}[u_0+1]+\frac{\Phi}{\tanh(\Phi)}\left[{R_2}^2+{R_1}^2u_0\right]\right\}}{\frac{\left[{R_2}^3-{R_1}^3\right]}{3(R_2-R_1)}} \qquad \text{Core-shell design} \quad (82)$$

where, $u_0 = \frac{\Phi R_2}{(R_2-R_1)\sinh(\Phi)+\Phi R_1\cosh(\Phi)}$, R_2 is adsorbent core radius, and R_1 is the total (core + shell) particle radius.

For an unsteady-state chemical reaction such as CaO carbonation (Equation 14), the definition of the effectiveness factor cannot be used in its conventional form (Equation 79). In this study, the following definition of the effectiveness factor proposed by Solsvik [201] is employed:

$$\eta = \frac{\text{actual rate of reaction}}{\text{reference reaction rate, } r_{ref}} \qquad (83)$$

Table 8 summarizes the values of dimensionless parameters, Φ_c and ζ, and theoretically catalyst and adsorbent effectiveness for four different particle diameters with an adsorbent-to-catalyst volume ratio of 4. Adsorbent effectiveness was calculated at 5% and 75% CaO conversion. The catalyst effectiveness of the core-shell design is always higher than that of the uniform-distributed design since in the core-shell design the catalyst is concentrated in the external shell of the particle rather than diluted in the entire volume.

Table 8. Dimensionless parameters values for the core-shell and uniform-distributed designs.

	CASE I	CASE II	CASE III	CASE IV
dp (mm)	7.68	3.84	1.92	0.96
Uniform-distributed				
Thiele Modulus, $\boldsymbol{\Phi_c}$	38.43	19.21	9.60	4.80
Theoretical Catalyst Effectiveness, $\boldsymbol{\eta_c}$	0.03	0.05	0.10	0.21
Theoretical Adsorbent Effectiveness, $\boldsymbol{\eta_s}$ (5%)	0.60	0.62	0.62	0.63
Theoretical Adsorbent Effectiveness, $\boldsymbol{\eta_s}$ (75%)	0.37	0.39	0.39	0.39
Core-shell				
Catalyst-Shell Thiele Modulus $\boldsymbol{\Phi_c}$	6.2	3.1	1.5	0.8
Catalyst-Shell Thickness, t_c	0.28	0.14	0.07	0.03
$\boldsymbol{\zeta}$	2.29	0.57	0.14	0.04
Theoretical Catalyst Effectiveness, $\boldsymbol{\eta_c}$	0.17	0.34	0.63	0.87
Theoretical Adsorbent Effectiveness, $\boldsymbol{\eta_s}$ (5%)	0.68	0.74	0.764	0.77
Theoretical Adsorbent Effectiveness, $\boldsymbol{\eta_s}$ (75%)	0.38	0.45	0.46	0.47

3.3.2 Numerical Solution

Two-dimensional models were implemented using the commercial Finite Element Method (FEM) software COMSOL Multiphysics® version 4.2. The catalyst-adsorbent multifunctional particles are modeled as two-dimensional elements with no flux in the axial direction. All models used a time-dependent version of the PDE General Form. The finite-element meshes employed were similar for both models and consisted of approximately 5000 triangular elements which corresponded to ~10^5 degrees of freedom. The reactor fluid phase is modeled as a one-dimensional element using the Weak Form Boundary PDE interface available in COMSOL Multiphysics®. A condition of maximum element size of 100 microns was employed, resulting in approximately 200 edge elements. Further mesh refinement resulted in < 0.1% variation in results, validating the accuracy of

the mesh. Solutions were obtained using the prepackaged time dependent solver MUMPS, with a relative tolerance of 10^{-6} and a maximum number of iterations of 25. All solutions were performed on a Dell PowerEdge R820 with eight (8) Intel Xeon CPU E5-4650 at 2.7 GHz and equipped with 256 GB of RAM. The typical solution times ranged from 1200 to 5000 s.

3.4 RESULTS AND DISCUSSION

3.4.1 Isothermal Sorption-Enhanced Water-Gas Shift Process

Figure 30 shows breakthrough curves for an isothermal SEWGS process at 600 °C and 28 bar with adsorbent Damköhler numbers varying between 50 and 500. A 4 mm particle size and an adsorbent-to-catalyst volume ratio of 4:1 were selected based upon previous SEWGS studies [198, 216]. Low Damköhler number values (< 200) resulted in CO_2 bypassing the reactor and very short pre-breakthrough periods. A sorbent Damköhler number of 350 was selected for all subsequent simulations to clearly present both pre-breakthrough and post-breakthrough regimes.

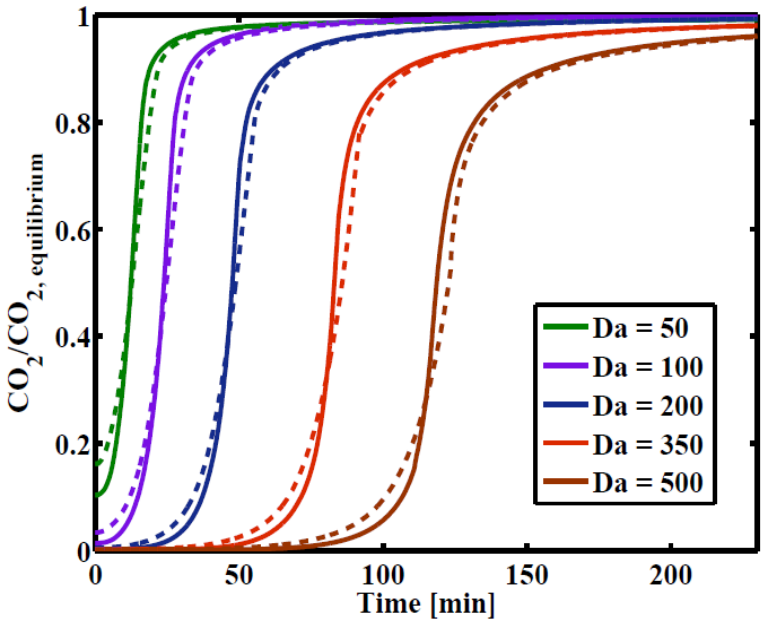

Figure 30. Carbon dioxide breakthrough curves for an isothermal SEWGS process with adsorbent Damkhöler numbers varying between 50 and 500. Core-shell (- -) and uniform-distributed (—) designs. Simulations conducted at 600 ºC and 28 bar.

Figure 31 presents how the composition of the SEWGS product stream changed over time. During the initial pre-breakthrough period, virtually all the CO_2 was adsorbed, resulting in high H_2 concentration in the product stream and complete CO conversion. This period is the fast-adsorption period when the CaO is most active for CO_2 capture. As time progressed, the CaO adsorbent was gradually converted to $CaCO_3$ and the rate of CO_2 adsorption slowed significantly. After breakthrough, the product gas composition became nearly constant (close to the equilibrium composition for WGS at the operating pressure and temperature), indicating the onset of the slow-adsorption period. In this slow-adsorption regime, most of the CaO had reacted, and the sorption reaction rate slowed down due to product layer formation on active CaO sites.

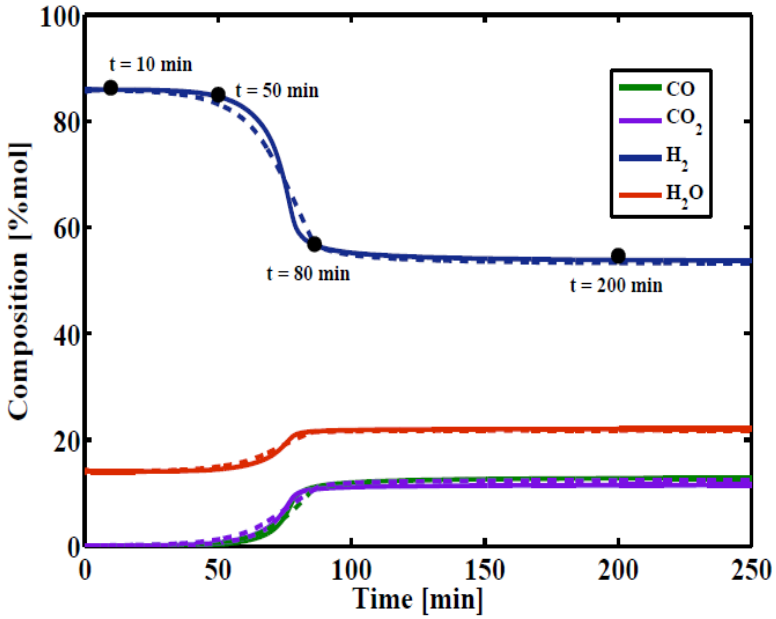

Figure 31. Outlet gas concentrations for an isothermal SEWGS process at 600 ºC and 28 bar. Core-shell (- -) and uniform-distributed (—) designs.

Both core-shell and uniform-distributed multifunctional designs had very similar breakthrough curves for the simulated conditions. The major difference is observed in the transition from the fast-adsorption to the slow-adsorption period (when the adsorbent bed is nearly saturated with CO_2). The core-shell design displayed a more gradual breakthrough profile than the uniform-distributed design; while this may be advantageous for the catalytic reaction; it represents lower adsorbent utilization per cycle. Figure 32 presents the concentration profiles along the reactor length for the different times indicated in Figure 31. These times were selected to clearly show the concentration profiles inside the reactor for both pre-breakthrough and post-breakthrough regimes. Figures 31 and 32 indicate that in the absence of thermal effects, the breakthrough curves of both designs are similar, with the uniform-distributed design enabling a higher adsorbent utilization.

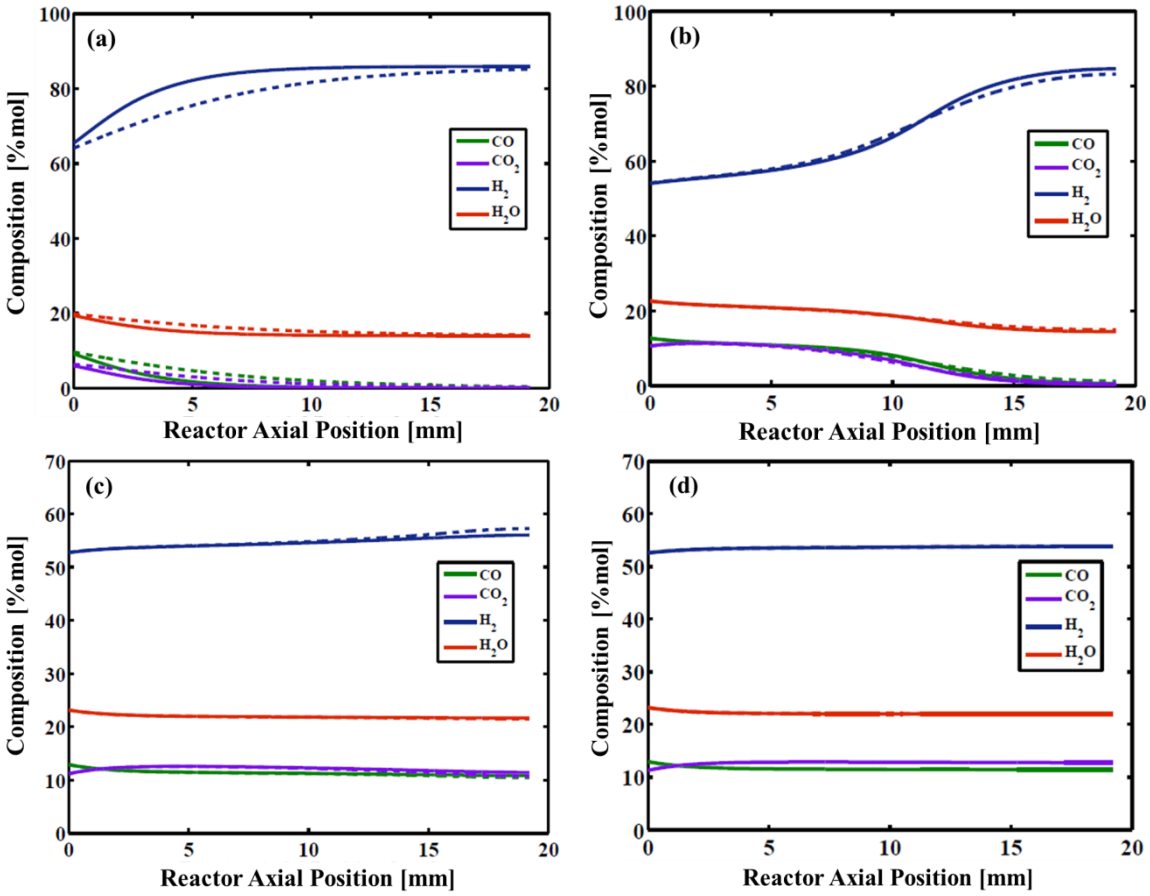

Figure 32. Concentration profiles along the reactor length for an isothermal SEWGS process at 600 ºC and 28 bar. Core-shell (- -) and uniform-distributed (—) designs at times (a) 10 min; (b) 50 min; (c) 80 min; and (d) 200 min.

3.4.2 Adiabatic Sorption-Enhanced Water-Gas Shift Process

Figure 33 displays outlet gas concentration as a function of time for an adiabatic SEWGS process at 28 bar. The fast-adsorption period lasted for approximately 50 minutes and, as time progressed, the CO_2 starts to appear in the reactor effluent. The temperature inside the reactor increased over time due to the exothermic nature of the carbonation and the water-gas shift reactions.

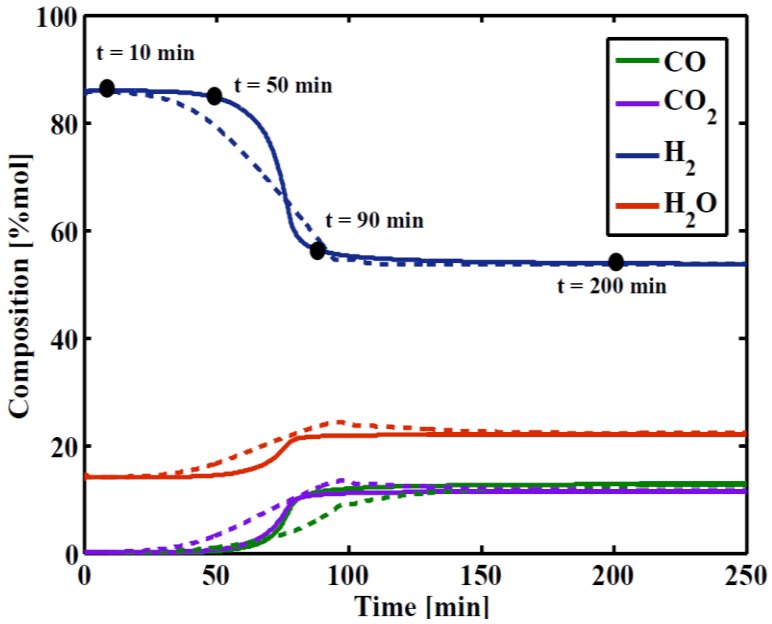

Figure 33. Outlet gas concentrations for an adiabatic SEWGS process at 28 bar. Core-shell (- -) and uniform-distributed (—) designs.

As for the isothermal SEWGS case, the core-shell design has a more gradual breakthrough profile than the uniform-distributed design. Figure 34 presents the temperature profiles along the reactor length.

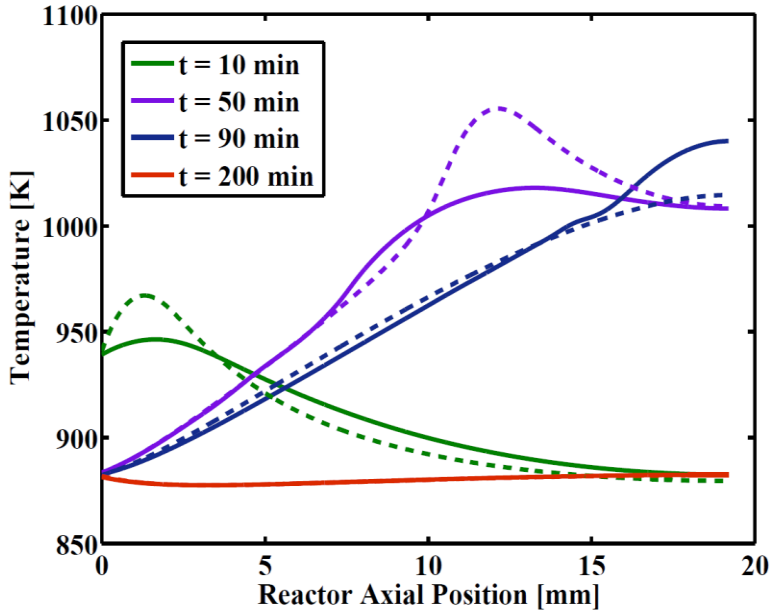

Figure 34. Temperature profiles along the reactor length for an adiabatic SEWGS process at 28 bar. Core-shell (- -) and uniform-distributed (—) designs at 10 min, 50 min 90 min, and 200 min.

The uniform-distributed design had a significantly higher hot-spot than the core-shell design during the fast-adsorption period (10 and 50 minutes). These higher temperatures are related to the higher sorption rates associated with the uniform-distributed design during the pre-breakthrough regime. Figure 35 shows the concentration profiles along the reactor length for the different times indicated in Figure 33.

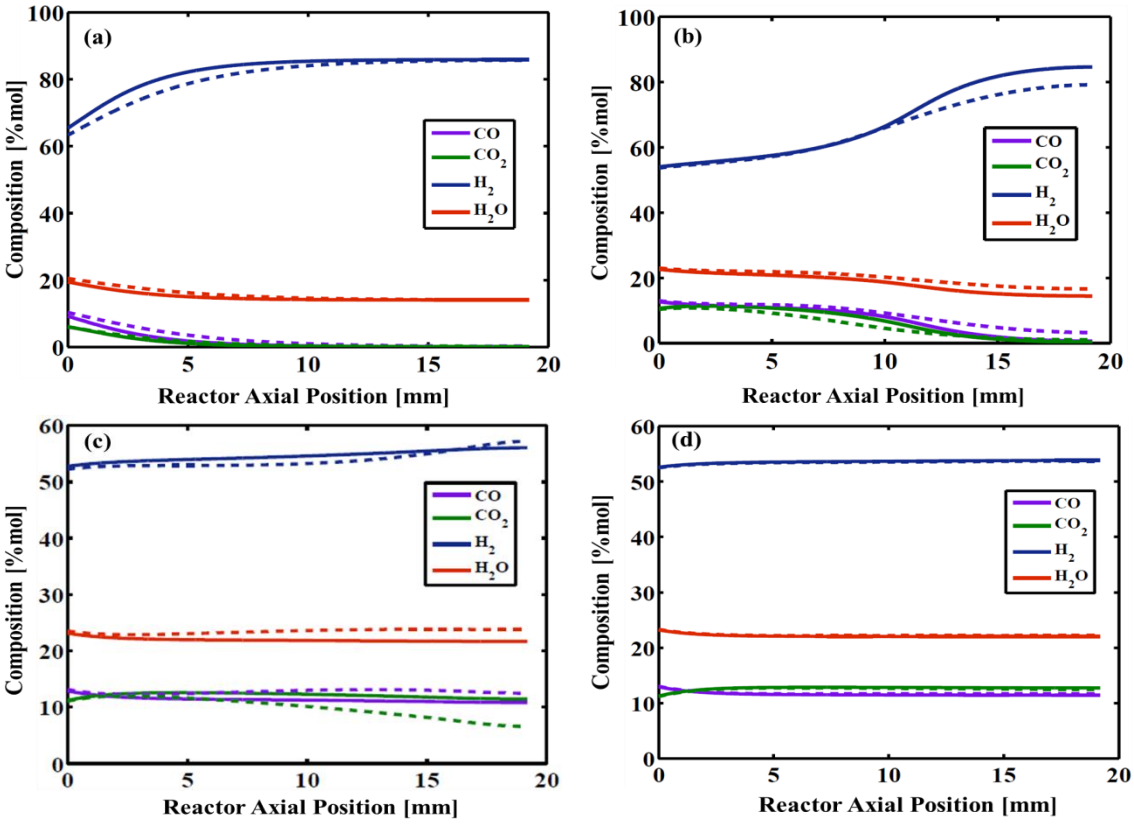

Figure 35. Concentration profiles along the reactor length for an adiabatic SEWGS process at 28 bar. Core-shell (- -) and uniform-distributed (—) designs at times (a) 10 min; (b) 50 min; (c) 90 min; and (d) 200 min.

3.4.3 Isothermal Sorption-Enhanced Methane Steam Reforming

Figure 36 presents how the composition of the SEMSR product stream changed over time for core-shell and uniform-distributed pellet simulations at 650 °C and 15 bar. These results correspond to an adsorbent-to-catalyst volume ratio of 4:1, an adsorbent Damköhler number of 350, and a particle size of 4 mm. For this process, the fast-adsorption period lasted for approximately 100 minutes. As time progressed, the CaO adsorbent was gradually converted to $CaCO_3$ and CO_2 started to appear in the reactor

effluent. Eventually, the product gas composition became nearly constant, close to the equilibrium composition for MSR process at operating pressure and temperature.

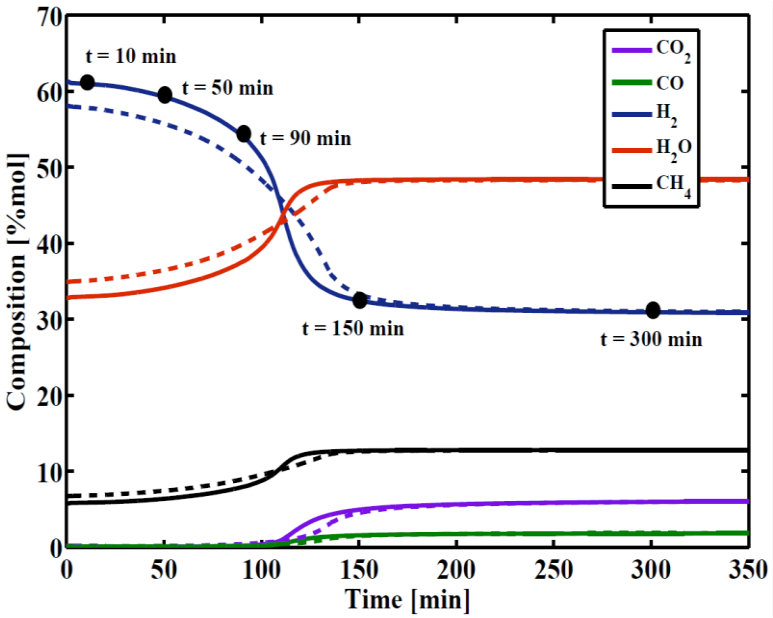

Figure 36. Outlet gas concentrations for an isothermal SEMSR process at 650 ºC, 15 bar, and with a 3:1 steam to CH_4 ratio. Core-shell (- -) and uniform-distributed (—) designs.

Figure 37 shows the concentration profiles along the reactor length for the different times indicated in Figure 36. Figures 36 and 37 show that in the absence of thermal effects, the breakthrough curve of the uniform-distributed design is slightly steeper and, therefore, this design has greater adsorbent utilization. During the breakthrough period (110 min to 150 min), the core-shell design had higher H_2 and lower CO and CH_4 concentrations exiting the reactor. However, outside the breakthrough period frame, the composition of the undesired species (CO, CH_4, CO_2) was lower for the uniform-distributed design.

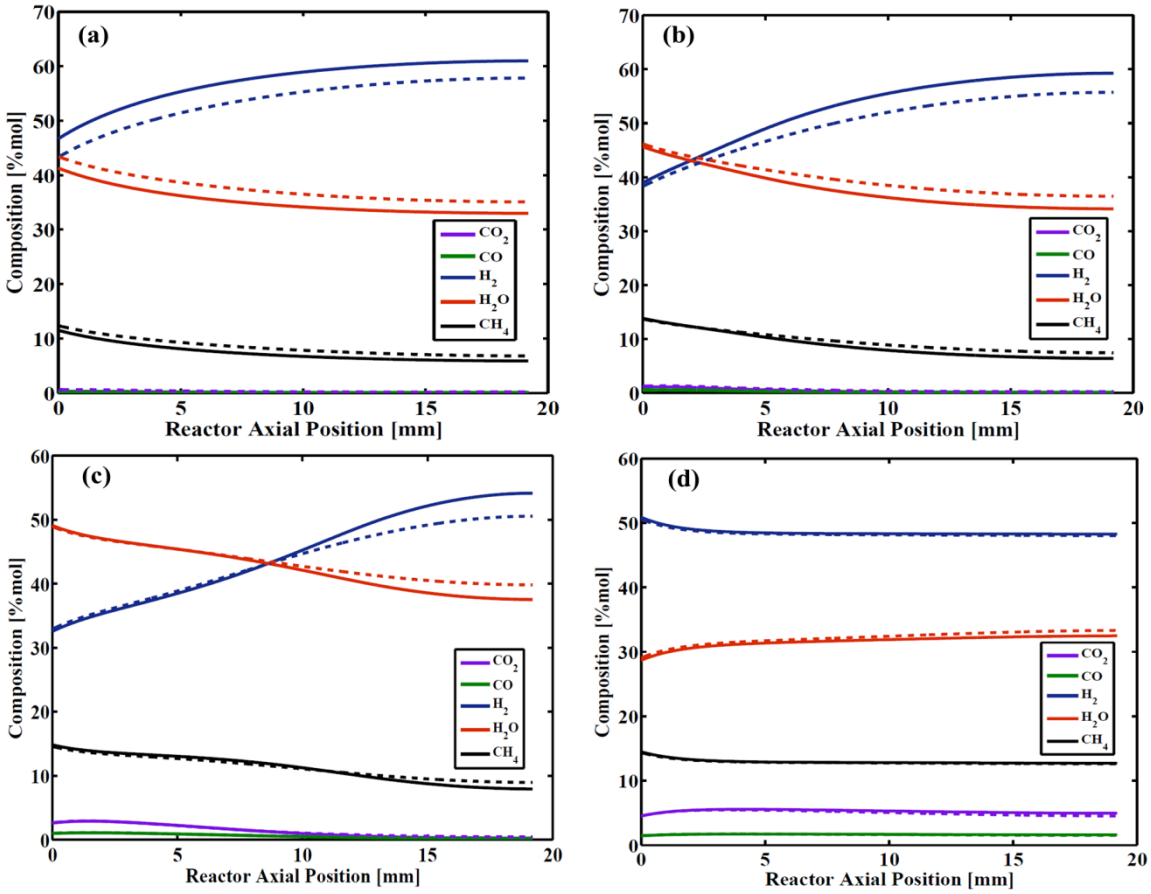

Figure 37. Concentration profiles along the reactor length for an isothermal SEMSR process at 650 ºC, 15 bar, and with a 3:1 steam to CH_4 ratio. Core-shell (- -) and uniform-distributed (—) designs at times (a) 10 min; (b) 50 min; (c) 90 min; (d) and 150 min.

3.4.4 Adiabatic Sorption-Enhanced Methane Steam Reforming

Figure 38 presents outlet gas concentration as a function of time for an adiabatic SEMSR process at 15 bar. As for the isothermal SEMSR case, the fast-adsorption period lasted for approximately 100 minutes. As time progressed, the temperature inside the reactor starts to decrease due to the endothermic nature of the MSR process. The temperature profiles along the reactor length for the different times indicated in Figure 38 are presented in Figure 39.

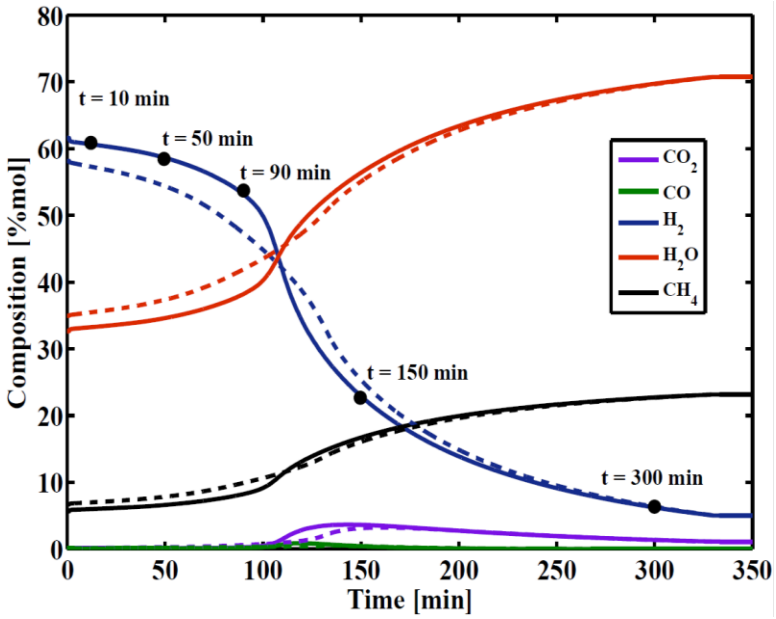

Figure 38. Outlet gas concentrations for an adiabatic SEMSR process at 15 bar and with a 3:1 steam to CH_4 ratio. Core-shell (- -) and uniform-distributed (—) designs.

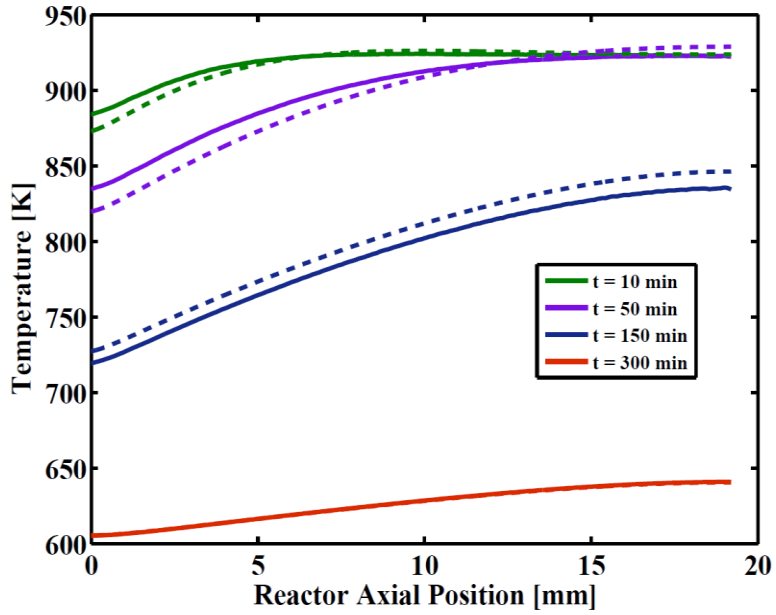

Figure 39. Temperature profiles along the reactor length for an adiabatic SEMSR process at 15 bar, and with a 3:1 steam to CH_4 ratio. Core-shell (- -) and uniform-distributed (—) designs at times 10 min, 50 min, 150 min, and 300 min.

The uniform-distributed design achieves higher temperatures than the core-shell design during the fast-adsorption period (10 and 50 minutes) due to the higher rates of exothermic CaO-CO_2 reaction. At 150 minutes, the uniform-distributed design has consumed most of the CaO available and, therefore, the endothermic MSR process is more predominant causing a decrease in temperature.

Figure 40 presents the gas concentration profiles along the reactor length. At every position inside the reactor, the uniform-distributed design has a higher concentration of H_2 and a lower concentration of H_2O, CO, and CH_4, except for the slow adsorption period (150 min) when the core-shell design has a slightly higher rate of heat production due to exothermic CaO carbonation.

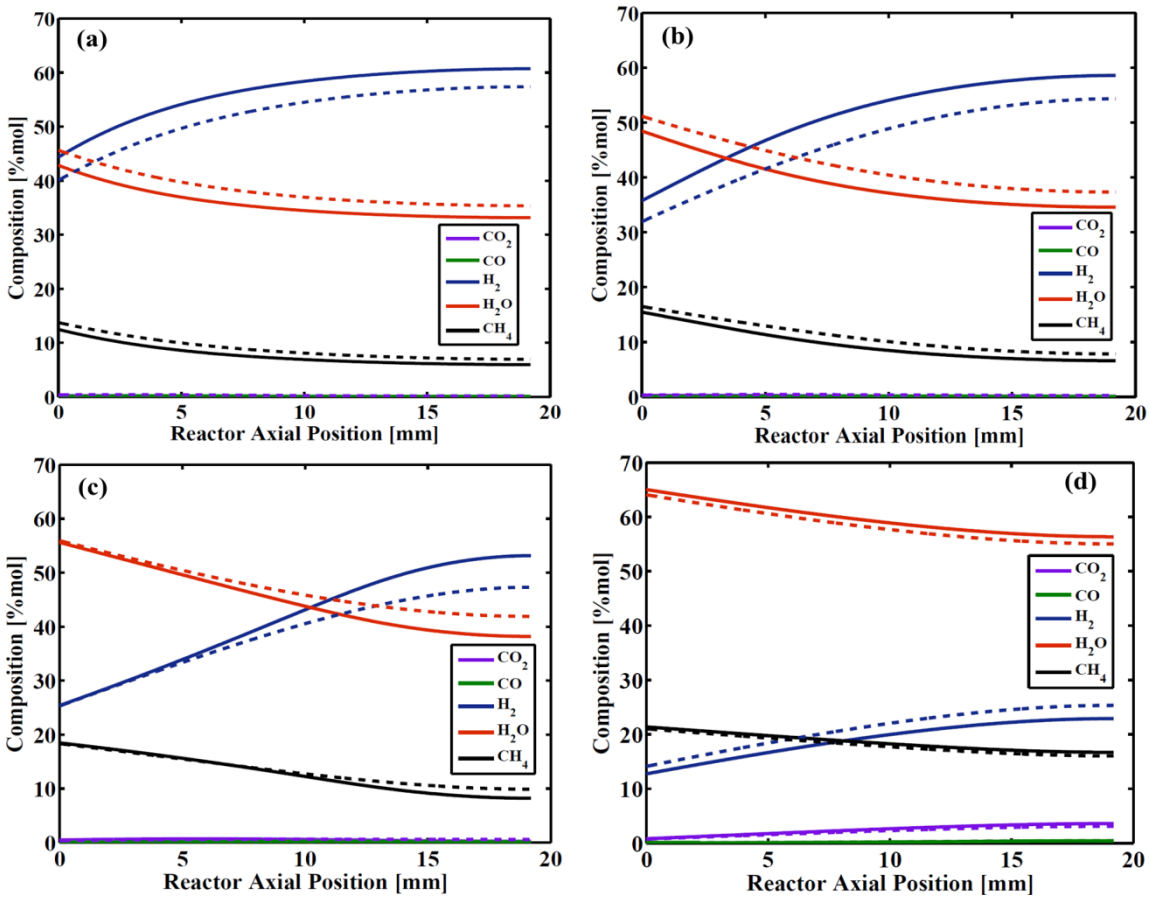

Figure 40. Concentration profiles along the reactor length for an adiabatic SEMSR process at 15 bar, and with a 3:1 steam to CH_4 ratio. Core-shell (- -) and uniform-distributed (—) designs at times (a) 10 min; (b) 50 min; (c) 150 min; and (d) 300 min.

3.4.5 Catalyst-Shell Thiele Modulus

To study the effects of catalyst-shell Thiele Modulus on overall process performance, simulations were carried with an adsorbent-to-catalyst volume ratio of 4:1 and an adsorbent Damköhler number of 350. Particle dimensions were selected to compare catalyst-shell Thiele Modulus in the range of 0.7 - 6.2 for the SEWGS case and 1.2 - 9.7 for the SEMSR case (Table 9).

Table 9. Particle dimensions of core-shell design for different catalyst-shell Thiele Modulus.

	Case I	Case II	Case III	Case IV
Particle Diameter (mm)	7.68	3.84	1.92	0.96
Adsorbent-to-catalyst Volume Ratio	4	4	4	4
Catalyst Thickness (mm)	0.28	0.14	0.07	0.03
Catalyst-Shell Thiele Modulus (WGS)	6.16	3.08	1.54	0.77
ζ (WGS)	2.29	0.57	0.14	0.04
Catalyst-Shell Thiele Modulus (MSR)	9.70	4.85	2.43	1.21

The comparison is made in terms of adsorbent utilization at the breakthrough point. The adsorbent utilization is calculated using the method presented by Geankoplis [186]. For this analysis, the breakthrough point is the time when the CO_2 exiting the reactor is equal to 5% of equilibrium CO_2 concentration expected solely by catalytic reaction at operating temperature and pressure. Figure 41a and 41b present the adsorbent utilization with uniform-distributed and core-shell designs as a function of the catalyst-shell Thiele Modulus for isothermal SEWGS and SEMSR processes, respectively. For both cases and for all catalyst-shell Thiele Modulus investigated, the uniform-distributed design had higher adsorbent utilization than the core-shell design. As the catalyst-shell thickness is increased, the difference in performance between the uniform-distributed and core-shell designs is higher. The ζ dimensionless parameter (Equation 78) increases as catalyst-shell thickness increases, suggesting that there is an increased resistance to CO_2 transport to adsorbent sites resulting from the addition of the outer catalyst layer. Figure 42 presents the adsorbent utilization with uniform-distributed and core-shell designs for the adiabatic SEWGS case.

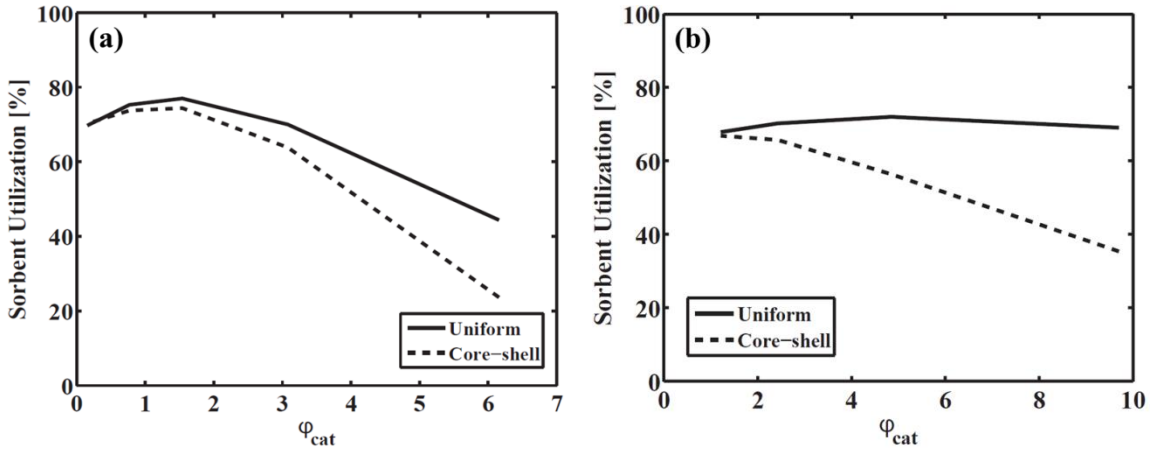

Figure 41. Adsorbent utilization at the breakthrough time as a function of catalyst-shell Thiele Modulus. Core-shell (- -) and uniform-distributed (—) designs. (a) Isothermal SEWGS process and (b) Isothermal SEMSR process.

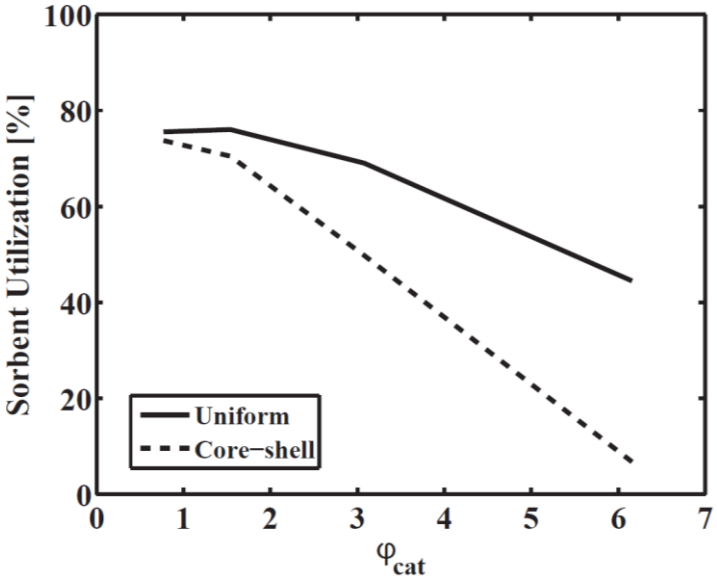

Figure 42. Adsorbent utilization at the breakthrough time as a function of catalyst-shell Thiele Modulus for an adiabatic SEWGS process. Core-shell (- -) and uniform-distributed (—) designs.

Figure 43 and 44 show the average H_2 mol% and CO mol% exiting the reactor before the breakthrough time is reached for isothermal SEWGS and SEMSR processes, respectively. For both processes and for all catalyst-shell thicknesses, the uniform-

distributed design always had higher H_2 mol% and lower CO mol% than the core-shell design up to breakthrough conditions.

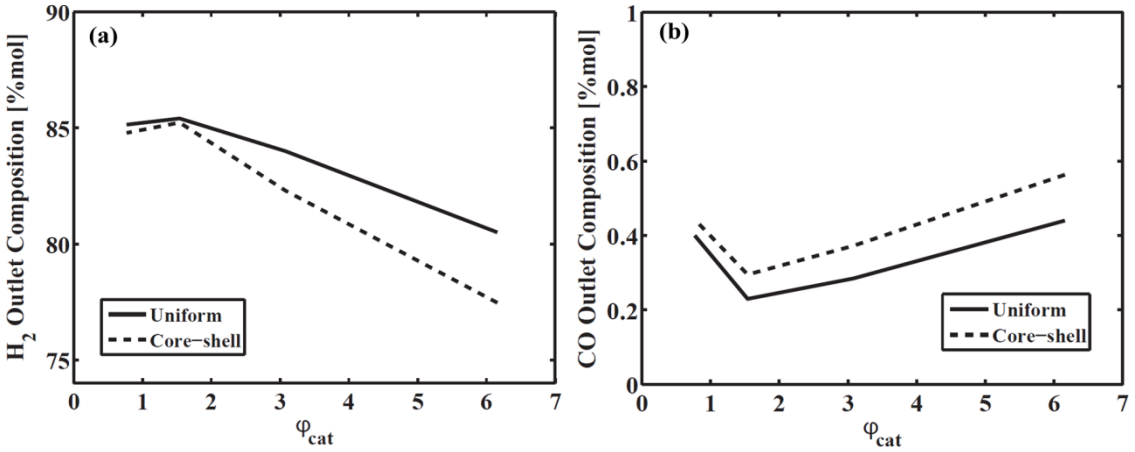

Figure 43. Average outlet mol% of (a) H_2 and (b) CO up to breakthrough conditions as a function of catalyst-shell Thiele Modulus for an isothermal SEWGS process at 600 ºC and 28 bar. Core-shell (- -) and uniform-distributed (—) designs.

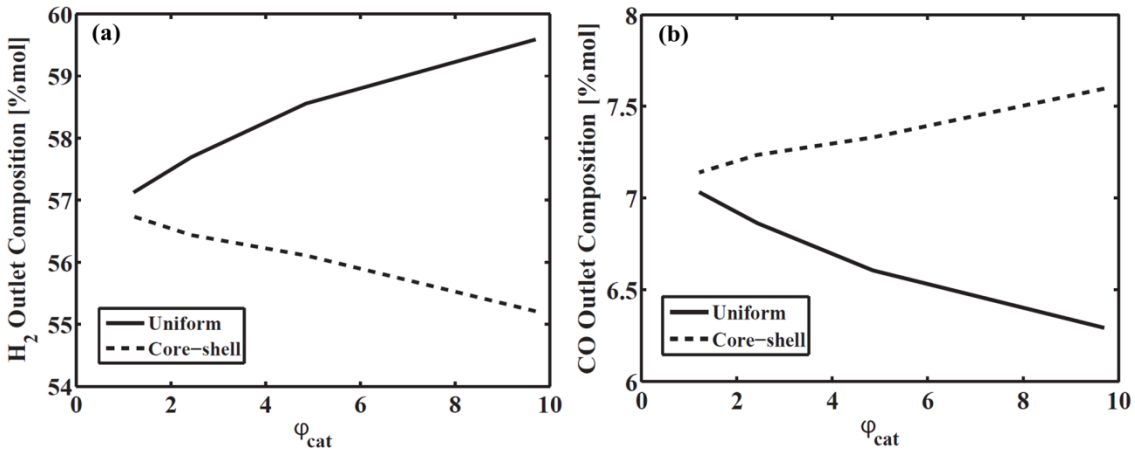

Figure 44. Average outlet mol% of (a) H_2 and (b) CO up to breakthrough conditions as a function of catalyst-shell Thiele Modulus for an isothermal SEMSR process at 650 ºC and 15 bar. Core-shell (- -) and uniform-distributed (—) designs.

3.4.6 Adsorbent-to-Catalyst Volume Ratio

To study the effects of adsorbent-to-catalyst volume ratio, simulations were carried out with a catalyst-shell Thiele Modulus of 1.5 (based on SEWGS) and an adsorbent Damköhler number of 350. Particle dimensions for both designs were selected in order to compare adsorbent-to-catalyst volume ratios of 2, 4, 6 and 8 (Table 10).

Table 10. Particle dimensions of core-shell design for different adsorbent-to-catalyst volume ratios.

	Case I	Case II	Case III	Case IV
Particle Diameter (mm)	1.09	1.92	2.75	3.57
Catalyst Thickness (mm)	0.07	0.07	0.07	0.07
Catalyst-Shell Thiele Modulus (WGS)	1.5	1.5	1.5	1.5
ζ (WGS)	0.14	0.14	0.14	0.14
Adsorbent-to-catalyst Volume Ratio	2	4	6	8

Figure 45 indicates that for isothermal and adiabatic SEWGS cases, the adsorbent utilization is nearly constant when the adsorbent-to-catalyst volume ratio is varied and the catalyst-shell thickness is kept constant. Although the particle size changes as the adsorbent-to-catalyst volume ratio is modified, it is the thickness of the catalyst layer of the core-shell design that affects the adsorbent utilization the most.

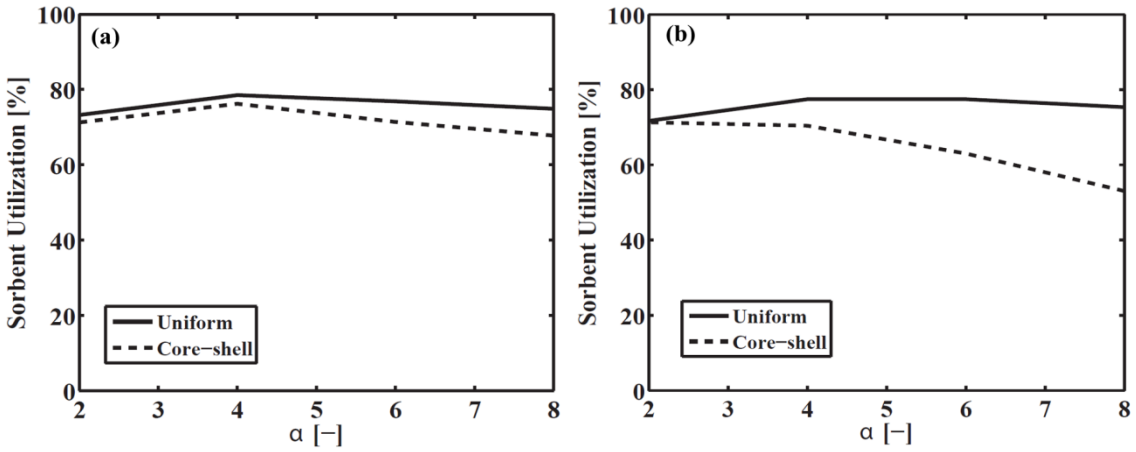

Figure 45. Adsorbent utilization at the breakthrough time as a function of adsorbent-to-catalyst volume ratio for SEWGS process. Core-shell (- -) and uniform-distributed (—) designs. (a) Isothermal case and (b) Adiabatic case.

3.5 CONCLUSIONS

This work presents the first side-by-side comparison of the two multifunctional catalysts proposed in the literature for sorption-enhanced reforming processes. Comparison of these two one-pellet designs demonstrates that the uniform-distributed design has a better adsorbent utilization than the core-shell design and, therefore, is preferable for SEWGS and SEMSR processes. The addition of the outer catalyst layer increases the resistance for CO_2 transport to adsorbent active sites, which translates to lower sorption rates. As core-shell design catalyst-shell thickness and ζ parameter decrease, the core-shell design performance approaches that of the uniform-distributed case. Variations in the adsorbent-to-catalyst volume ratio have no significant effect on the performance of either one-pellet design. Finally, for the case of an adiabatic SEWGS process, the core-shell design reduces the hot-spot temperature by ~40 K when compared

to the uniform-distributed design while adsorbent utilization at breakthrough is reduced by 20%.

CHAPTER IV

SUPER HYDROGEN AND HELIUM BARRIER WITH POLYELECTOLYTE NANOBRICK WALL THIN FILM*

4.1 INTRODUCTION

Gas barrier films have found broad application in the food, pharmaceutical, and flexible electronics industries [132-134]. These films often require a combination of low permeability, optical transparency, mechanical strength, and flexibility [135]. Current barriers include metallized films [137], SiO_x coatings [138], and polymer composites [139]. While these materials offer excellent barrier properties, they often suffer from poor substrate adhesion, undesirable optical quality, and limited flexibility [140].

Although chemical vapor deposition (CVD) [217, 218] and solvent casting [219, 220] are the most common techniques used for gas barrier film fabrication, the Layer-by-Layer (LbL) assembly technique continues to grow in popularity since the early 90s [117] due to its simplicity and versatility. By alternately exposing a substrate to polymer solutions with a specific interaction (e.g., ionic or hydrogen-boding), the attractions between the ingredients result in the buildup of a functional multilayer structure with unique properties. LbL assemblies prepared with polymers and clay nanoplatelets have proven capable of overcoming limitations associated with current gas barrier films (e.g., poor substrate adhesion, limited flexibility) while still providing low permeability and

* Reprinted with permission from "Super Hydrogen and Helium Barrier with Polyelectolyte Nanobrick Wall Thin Film" by Ping Tzeng, Elva Lugo, Garret D. Mai, Benjamin A. Wilhite,* and Jaime C. Grunlan, 2015. Macromolecular Rapid Communications, 36, pp 96–101, Copyright 2015 by John Wiley & Sons, Inc.

optical transparency owing to the formation of a nanobrick wall structure [221-224]. The work presented in this Chapter marks the first investigation of LbL thin films for providing low He and H_2 permeabilities (i.e., high barrier) to plastic films.

Hydrogen is a key feedstock for the manufacture of important chemicals such as ammonia and methanol [12]. The wide flammability window and low ignition temperature for H_2, combined with an extremely high solid-state mobility, in both metallic and polymeric materials, require the use of thick-walled metallic containers for safe transport and storage of industrial scale H_2 [223]. Additionally, H_2 corrosion and embrittlement of process equipment remains a significant safety concern [225]. Recent growth in H_2-driven fuel cell technologies, offering high efficiencies and zero point-of-use emissions for portable, household, and vehicular power generation, necessitates breakthroughs in size and weight reduction for H_2 storage and transportation equipment [226-228], which may be achieved through the development of polymer nanocomposite H_2 barrier coatings. Furthermore, these conformal H_2 barrier coatings would allow an extension of process equipment lifetime by reducing the risk of equipment failure owing to prolonged H_2 exposure.

Helium is widely used in the manufacturing sector for leak detection [229, 230] and as an inert gas blanket for high-temperature welding [231] and reactive chemical storage [232]. It is also used in the medical sector as a cryogenic medium for magnetic resonance imaging (MRI) tools [233]. Additionally, helium provides an excellent source of lift for lighter-than-air vehicles (for meteorological and aviation use) [234]. Despite being the second-most abundant element in the universe, terrestrial supplies of helium

continue to dwindle as released gas is sufficiently buoyant to escape the atmosphere [235]. This non-renewable nature of terrestrial helium requires further advances in He-barrier film technologies to ensure the continued sustainability of manufacturing and medical industries. A He-H_2 barrier thin film would allow the storage of these gases, at least temporarily, in relatively lightweight polymeric containers.

Commercial He gas barriers currently employ aluminized polyurethane or polyolefin/polyester that are capable of providing low He permeability (10 - 300 cm^3 mm m^{-2} day^{-1} atm^{-1}) [236, 237], but are produced using complex process conditions, have poor optical properties, and potential health hazards. Metallization of polymeric films requires ultra-high vacuum and high-temperature conditions, resulting in a complex and energy-intensive process. Aluminum nanocoatings are typically opaque and often have adhesion problems, which further limits their applicability [238]. These films also pose environmental and health concerns, as aluminum can contaminate the environment through both water and airborne transmission [238]. Current materials employed to fabricate H_2 gas barriers include ethylene vinyl-alcohol (EVOH) copolymer and polyester/nanoflake composites, with reported permeabilities of 0.1 - 3.1 cm^3 mm m^{-2} day^{-1} atm^{-1} [223, 239, 240]. Unfortunately, EVOH copolymers are plasticized in the presence of moisture, irreversibly altering their morphology and causing an increase in free volume and permeability [241]. Polymer/nanoflake film properties remain difficult to control owing to both nanoflake dispersion and exfoliation during processing.

In the present work, a polymer/clay composite thin film fabricated via LbL assembly, is investigated as a He and H_2 gas barrier. Clay-polymer composites assembled

via LbL have been shown to improve mechanical [242], oxygen barrier [126, 243], drug release [244], and flame retardant properties [245], relative to all-polymer LbL films and traditional thick film nanocomposites. The simplicity of the LbL technique, as compared to current gas barrier film fabrication methods, makes it an attractive alternative. The present quadlayer (QL) system was prepared by repeatedly depositing polyethylenimine (PEI), poly(acrylic acid) (PAA), PEI, and montmorillonite (MMT) clay (Figure 46a and b). This system was previously investigated for its super oxygen barrier [126], but barrier to light gases (i.e., hydrogen and helium) was very unexpected. Highly aligned and impermeable clay platelets create an extremely tortuous pathway which extends permeate retention times and reduces even light gas transmission rate [246, 247].

4.2 EXPERIMENTAL PROCEDURE

4.2.1 Materials

Branched PEI (Aldrich, St. Louis, MO) (MW ~ 25,000 g mol^{-1}) is a cationic polymer that was dissolved in 18.2 MΩ deionized water to create a 0.1 wt% solution. The pH was adjusted from its unaltered value (~10.5) to 10 by adding 1.0 M hydrochloric acid (HCl). PAA (Aldrich) (MW ~ 100,000 g mol^{-1}) is an anionic polymer that was prepared as a 0.2 wt% solution with deionized water. The pH of PAA was adjusted from its unaltered value (~3.1) to 4 by adding 1.0 M sodium hydroxide (NaOH). Anionic natural sodium MMT (trade name Cloisite Na+) (Southern Clay Products, Inc., Gonzales, TX) clay was prepared as a 1.0 wt% aqueous suspension. This suspension of high aspect ratio nanoplatelets (aspect ratio is 80 to 300, with 1 nm platelet thickness) [248] was used at its

natural pH (~9.7). The aqueous solutions were used to grow barrier films on 51 µm (trade name Trycite 8001) polystyrene (PS) substrates (Dow, Midland, MI).

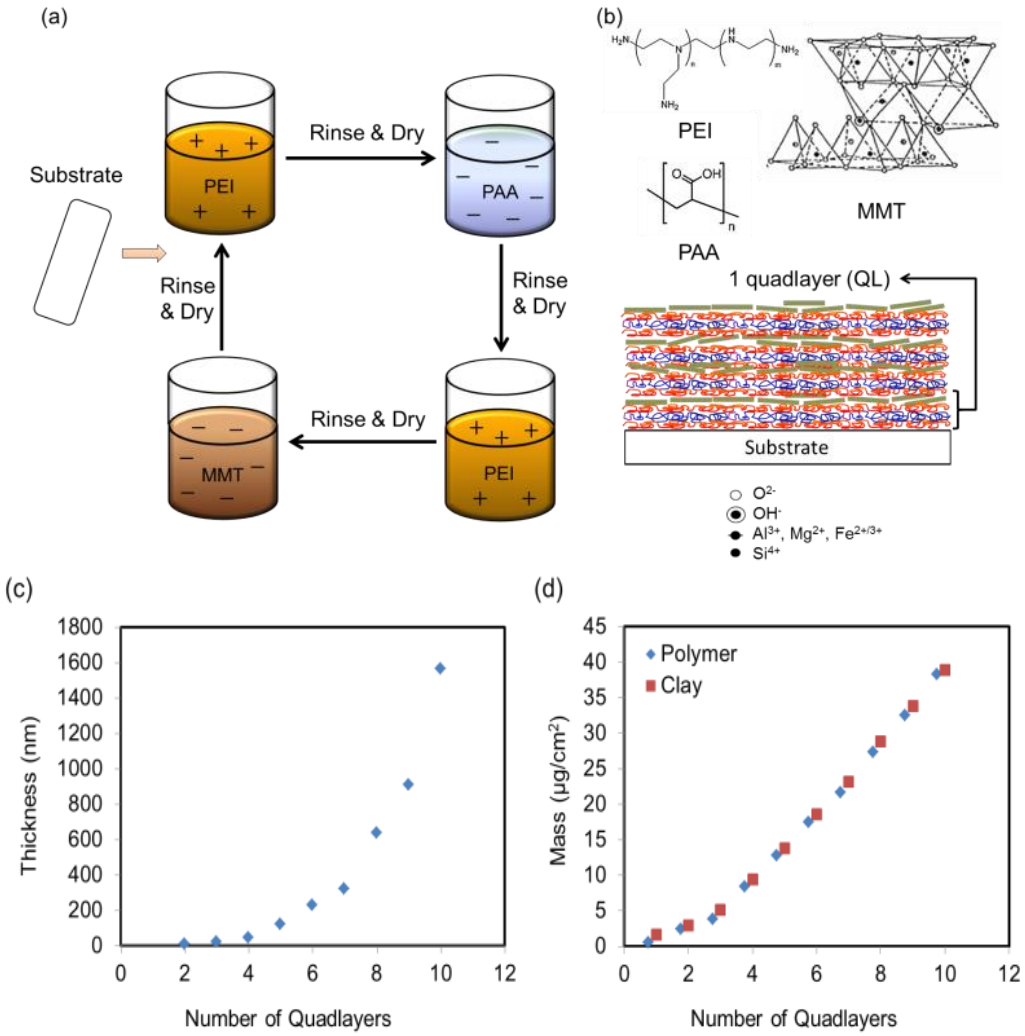

Figure 46. (a) Schematic of the quadlayer assembly process. (b) Polyelectrolytes and clay used in the quadlayer assemblies and a cross-sectional illustration of the resulting nanobrick wall thin film. MMT structure [248]: (•)Al^{3+}, Mg^{2+}, $Fe^{3+/2+}$; (○) O^{2-}; (⊙) OH^{-}; (●) Si^{4+}. (c) Film thickness as a function of PEI/PAA/PEI/MMT quadlayers deposited. (d) Mass as a function of quadlayers deposited. Diamond and rectangular dots indicate the accumulated mass measured from the first PEI layer to the specific polymer or clay layer, respectively.

4.2.2 Layer-by-Layer Deposition

The PS substrate was rinsed with deionized water and methanol before use, then plasma-treated with an ATT0 Plasma Cleaner (Thierry Corp., Royal Oak, MI). Plasma treatment improves adhesion of the first polyelectrolyte layer by oxidizing the film surface [249]. The substrate was first dipped into the PEI solution for 5 minutes, followed by rinsing with deionized water for 30 seconds and drying with a stream of filtered air. After the first positively-charged layer was adsorbed, the substrate was dipped into PAA solution for another 5 minutes, followed by another rinsing and drying cycle. The substrate was then dipped into PEI and MMT solutions (5-minute dips) to form one quadlayer. Starting from the second deposition cycle, the remaining layers were deposited using one minute dip times. This process was carried out using home-built robot system [249, 250]. The pH of PEI and PAA is shown as a subscript next to the initials in the figures and text. For example, one quadlayer of PEI(pH=10)/PAA(pH=4)/PEI(pH=10)/MMT (unaltered pH of 9.7) is abbreviated as $(PEI_{10}/PAA_4/PEI_{10}/MMT)_1$.

4.2.3 Film Characterization

Assembly thickness on silicon wafers was measured every quadlayer with a PHE-101 Discrete Wavelength Ellipsometer (Microphotonics, Allentown, PA) in absorbance mode, using a 632.8 nm laser at an incidence angle of 65°. Mass increments were measured each layer with a research quartz crystal microbalance (QCM) (Inficon, East Sycrase, NY) using a frequency range of 3.8 - 6 MHz. The 5 MHz quartz crystal was inserted in a holder and dipped into the solutions. After each deposition, the crystal was rinsed and dried and then left on the microbalance to stabilize for 5 minutes. Cross-sections

of the quadlayer assemblies were imaged with a Tecnai F20 transmission electron microscopy (TEM, FEI, Hillsboro, OR), operated at 200 kV. Samples were prepared for imaging by embedding a piece of coated polyethylene terephthalate (PET) in epoxy prior to sectioning it with a diamond knife.

4.2.4 Gas Permeation System

Gas permeability coefficients of H_2 and He were measured using a constant-volume, variable-pressure apparatus (Figure 47). Permeate flux was measured through a membrane by monitoring the pressure increase, in a closed vessel, using a pressure transducer. The film was mounted in a permeation cell and the upstream and downstream volumes were evacuated to degas the film. The valve connecting the permeation cell to the vacuum pump was then closed and a measurement of the vacuum leak rate in the downstream side, $(dp_1/dt)_{leak}$, was taken. Once the leak rate was determined, feed gas was introduced into the upstream side of the membrane and the pressure rise as a function of time in the downstream side was recorded. Gas permeabilities P_i (cm^3 (STP) cm cm^{-2} s^{-1} $cmHg^{-1}$) were calculated using the steady-state pressure increase, $(dp_1/dt)_{ss}$, in a fixed downstream volume as [113]:

$$P_i = \frac{V_d t_m}{p_2 A_{mem} RT}\left[\left(\frac{dp_1}{dt}\right)_{ss} - \left(\frac{dp_1}{dt}\right)_{leak}\right] \quad (84)$$

where V_d is the downstream volume in cm^3, t_m is the film thickness in cm, p_2 is the upstream absolute pressure in cmHg, A_{mem} is the film area available for gas transport in cm^2, R is the gas constant, T is the absolute temperature in Kelvin, and $(dp_1/dt)_{ss}$ and $(dp_1/dt)_{leak}$ are the steady-state rates of pressure increase (cmHg/s) in the downstream

volume at a specific upstream pressure and under vacuum, respectively. In order to achieve proper gas permeability measurements, the maximum pressure increase rate under vacuum, $(dp_1/dt)_{leak}$, was kept below 10% of the steady-state pressure increase rate, $(dp_1/dt)_{ss}$.

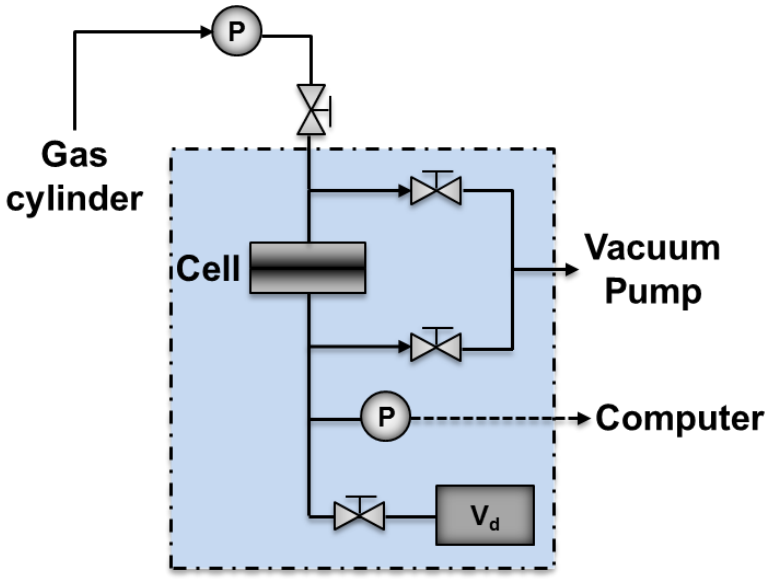

Figure 47. Schematic of constant-volume variable-pressure apparatus used for gas permeability measurements [113].

The permeation cell is a 47 mm HP Filter Holder (Millipore, Billerica, MA) with an area of 9.6 cm^2. The downstream pressure was always kept below 10 Torr to maintain an effectively constant pressure difference across the membrane. The pressure rise in the downstream volume was monitored using a Baratron 626B 100 Torr capacitance manometer (MKS, Andover, MA). The calibrated downstream volume was 306 cm^3. A relief valve was used to prevent the downstream pressure from increasing above atmospheric pressure. This was necessary to prevent accidental over-pressurization of the

transducer in the event of membrane rupture. The upstream pressure was varied between 4 atm - 6 atm and was measured using a PX409-250 pressure transducer (Omega Engineering, Stamford, CT). Measurements were carried out at room temperature using UHP[6] grade gases. Swagelok VCR connections and VCO needle valves were used for the downstream volume connections to minimize leaks.

4.3 RESULTS AND DISCUSSION

Unlike some LbL systems, which grow linearly, the exponential growth shown in Figure 46c is attributed to interdiffusion of the weak polyelectrolytes in this quadlayer assembly [120, 126, 242, 251]. The thin growth observed in the first few QL is strongly affected by the substrate, suggesting the deposited materials may not have full coverage during this 'island growth' period [120, 252]. After the initial growth, interdiffusion of PEI and PAA takes over because both are in their low charge state at pH 10 and pH 4, respectively. For the mass growth, since polymers (~1.0 g cm^{-3}) [251] have a lower density than clay (2.9 g cm^{-3}) [253], so instead of seeing an obvious exponential trend caused by the polymer, one can only observe a slope change between the initial stage and interdiffusion stage. Despite the unobvious trend, clay concentration decreases as the number of QL increases, as shown in Table 11 and Figure 46d, attributed to the additional PEI and PAA deposited through interdiffusion.

Figure 48 shows TEM cross-sectional images of PEI/PAA/PEI/MMT assemblies, showing how clay concentration decreases at higher quadlayer numbers. The dark lines in

[6] Ultra High Purity

Figure 48a represent individual platelets, revealing that they are oriented parallel to the substrate and well exfoliated. Although clay is deposited five times in this 5 QL film, more than five clay layers are observed. Both exfoliated platelets and intercalated stacks can be seen, similar to the results found in other studies [126, 242]. A possible reason can be incomplete coverage of the films during the assembly, resulting in clay depositing at different vertical position at each quadlayer. This geometric imperfection is the reason of increasing internal roughness [254], and can certainly lead to exponential growth. The 10 QL film shows similar structure to the 5 QL film in the initial quadlayers (Figure 48b), but later exhibits increasing clay spacing (Figure 48c). Since the distance between the top and the bottom clay layer in Figure 48c is 530 nm, it is believed that the four clay layers represent the 5th, 6th, 7th and 8th quadlayer, based on ellipsometry results. The spacing reaches ~160 nm in Figure 48c, suggesting a decreased clay concentration. The images show that the interdiffusion of PEI and PAA is able to expand the clay stacks and diffuse through the layers of platelets.

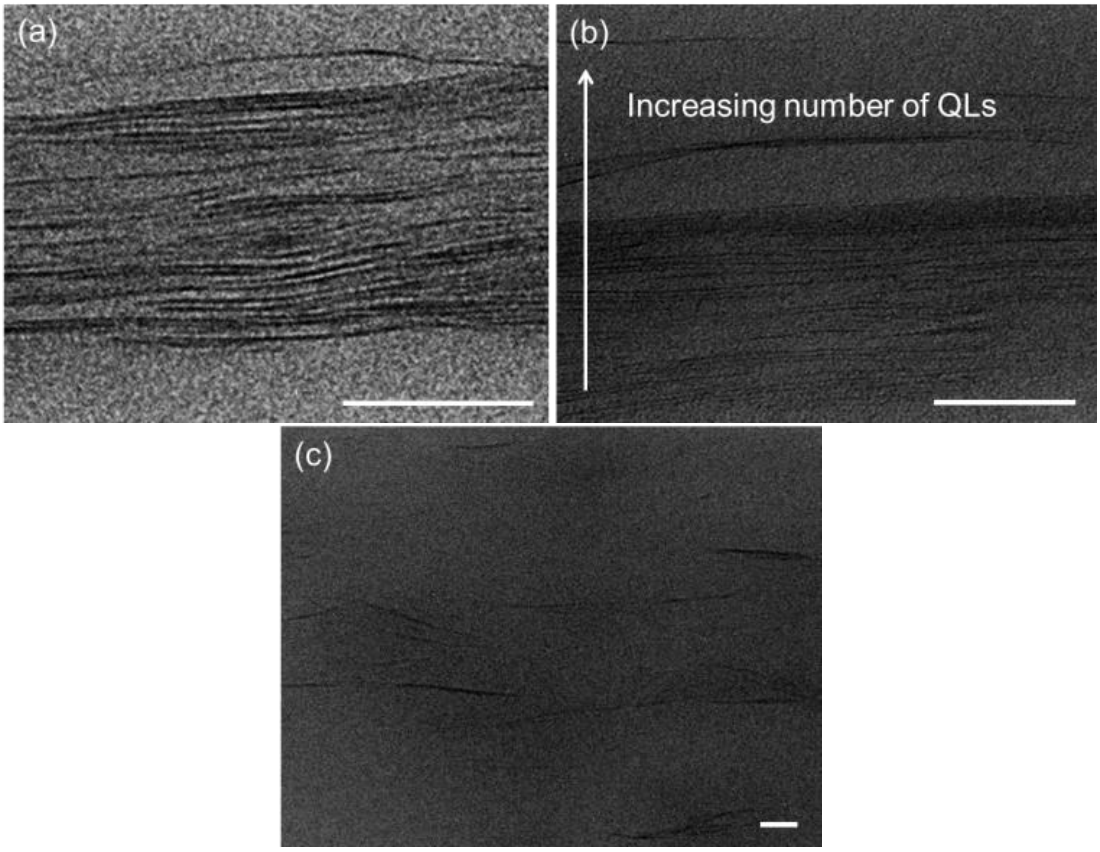

Figure 48. TEM cross-sectional images of (a) 5 and (b) (c) 10 PEI/PAA/PEI/MMT QL. (b) is the portion of the film closest to the polystyrene substrate, while (c) is further away, the four dark lines most likely represent the 5th, 6th, 7th and 8th QL. White scale bar in each figure represents 50 nm.

These TEM images confirm that a nanobrick wall structure is generated by this LbL deposition (Figure 48). Figure 49 shows H_2 and He permeabilities of LbL quadlayer assemblies deposited on 51 μm polystyrene substrates. The overall He and H_2 permeabilities are observed to decrease by three orders of magnitude relative to the bare substrate, while the overall film thickness increases by only 0.2% (Table 11). Increasing the number of QLs from 5 to 10 does not improve the barrier properties. This lack of improvement may be attributed to the dramatically expanded clay spacing and associated concentration reduction (as confirmed by analysis of growth profiles and film morphology

in Figures 46c and 48, respectively), which diminishes the tortuous path afforded by the nanobrick wall structure. The 5 QL nanocomposite, with a thickness of 122 nm, exhibits a H_2 permeability one order of magnitude lower than laminated EVOH film [239], and a He permeability three orders of magnitude lower than metallized polyolefin/polyester [236].

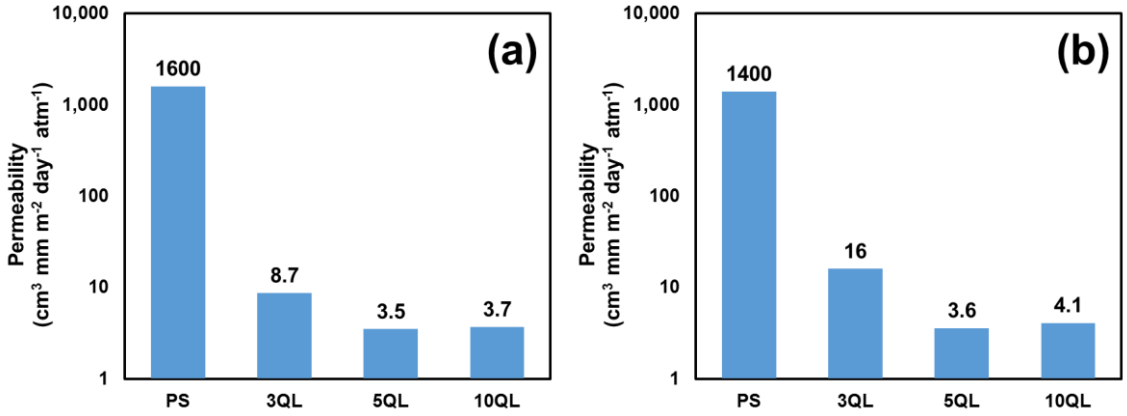

Figure 49. Permeability of (a) hydrogen and (b) helium as a function of quadlayers deposited on a 51 μm polystyrene substrate.

Table 11. Permeability, film thickness, and clay concentration of quadlayer assemblies deposited on 51 μm polystyrene.

	Film Thickness (nm)	Clay loading (wt%)	Transmission Rate ($cm^3\ m^{-2}\ day^{-1}\ atm^{-1}$)		Permeability ($cm^3\ mm\ m^{-2}\ day^{-1}\ atm^{-1}$)	
			H_2	He	H_2	He
PS			31000	27000	1600	1400
3QL	48.6	54.9	170	320	8.7	16
5QL	122	34.7	69	71	3.5	3.6
10QL	1564.8	26.8	71	78	3.7	4.1

4.4 CONCLUSIONS

The present study represents the first demonstration of LbL deposited films with low hydrogen and helium permeabilities. The impermeable clay platelets, together with highly interdiffused PEI and PAA mortar, formed a nanobrick wall structure that imparts significant light gas barrier. The permeability of both helium and hydrogen decreased as the number of quadlayers increased, showing two to three orders of magnitude improvement compared to commercial barriers. However, increasing the number of quadlayers from 5 to 10 did not improve the barrier properties. This lack of improvement is attributed to the expanded clay spacing and associated concentration reduction. The uniqueness of these polymer/clay barrier thin films is due to the high clay loading and strong ionic interactions between the polyelectrolytes. The excellent performance of these thin films, combined with the simplicity of the LbL deposition method, makes these light gas barrier coatings an exciting opportunity for several packaging and protective applications.

CHAPTER V

HIGHLY SELECTIVE MULTILAYER POLYMER FILMS FOR CO_2/N_2 SEPARATION

5.1 INTRODUCTION

The use of membranes to selectively remove CO_2 from mixtures with N_2 is of interest for the application in flue gas rectification [255, 256]. In the present study, the Layer-by-Layer (LbL) technique is used to assemble a hydrogen-bonded film of poly(ethylene oxide) (PEO) and poly(methacrylic acid) (PMAA) for the separation of CO_2 from N_2. Polymers containing polar ether groups, such as PEO, are generally more selective to CO_2 than to other gas molecules, due to favorable dipole-quadrupole interactions between CO_2 and the polar ether groups [257]. There have been numerous studies of polymer membranes containing PEO, poly(ethylene glycol) (PEG), or other groups bearing polar ether segments [258]. Despite the interest in PEO-based materials for CO_2 separations, these materials have a high degree of crystallinity which typically results in low permeability values.

LbL assembly, which was developed two decades ago, has been studied as a simple and versatile technique to fabricate multifunctional thin films [114, 259, 260]. Extension of the LbL assembly technique to gas purification membranes promises the ability to tune overall gas permeability and selectivity by varying different deposition parameters (e.g., deposition time, pH, concentration, etc.). The hypothesis of this work is that the versatility

of the LbL method will allow the formation of very dense PEO-based films while avoiding/mitigating the formation of crystalline regions.

Previous studies of LbL membranes for gas separation purposes have focused on producing amorphous assemblies of conventional gas separation polymers. However, these studies have resulted in polymer materials with reduced permeability values than the equivalent homogenous polymer blends at similar selectivities [155]. Kim et al. [124] reported an ion-paired polyethylenimine (PEI)/poly(acrylic acid) (PAA) thin film with outstanding H_2/CO_2 and H_2/ N_2 selectivities (190:1 and 2350:1, respectively) owing to a unique ionically crosslinked structure achieved by using the LbL technique. However, the permeability of these membranes was significantly reduced due to the dense structure of the polyelectrolyte layers.

In this work, hydrogen-bonded LbL films are created by alternately exposing a polystyrene (PS) substrate to an aqueous solution of proton-donating (PMAA) and proton-accepting (PEO) polymers. Previous work with hydrogen-bonded LbL assemblies has shown that these films are highly elastomeric and more permeable than ion-paired thin films due to weaker interactions between the polymer constituents (hydrogen bonds vs. ionic bonds) [261]. The higher permeability of hydrogen-bonded thin films may make them more suitable for gas separation applications than conventional ion-paired LbL membranes.

5.2 EXPERIMENTAL PROCEDURE

5.2.1 Materials

Branched PEI (MW 25,000 g/mol) was purchased from Sigma-Aldrich (Milwaukee, WI) and was used as a 0.1 wt% aqueous solution at its unaltered pH (~10.5). PEO (MW 4,000,000 g/mol) and PMAA (MW 100,000 g/mol), purchased from Polysciences, Inc. (Warrington, PA), were prepared as 0.1 wt% and 0.2 wt% aqueous solutions, respectively. All solutions were made in 18.2 MΩ deionized water and rolled overnight to achieve homogeneity. PMAA and PEO solutions were altered to different pH levels (2, 2.5, or 3) using 1 M hydrochloric acid (HCl) or sodium hydroxide (NaOH).

5.2.2 Substrate

Single-side polished (100) silicon wafers (University Wafer, South Boston, MA) were used as substrates to measure film thickness and for scanning electron microscopy (SEM) and atomic-force microscopy (AFM) imaging. Polystyrene films, with a thickness of 25 μm, were purchased from Goodfellow Corporation (Huntington, England) and used as substrates for gas permeation testing. Prior to film deposition, the polystyrene substrate was rinsed with deionized water and plasma treated with an ATTO plasma cleaner (Diener, Germany) at 25W for 5 min to improve the adhesion of the first PEI layer deposited. Teflon films were used as substrates for preparing free-standing films that were used for differential scanning calorimetry (DSC) and Fourier-transform infrared (FTIR) testing. Plasma treatment was not applied to avoid the strong adhesion of films to the substrate. Teflon substrates were rinsed with deionized water and methanol, then dried with filtered air before deposition. Polished Ti/Au crystals, with a resonant frequency of

5 MHz, were purchased from Inficon (East Syracuse, NY) and used to monitor mass deposition. The resonant frequency was measured after 5 min drying, following each deposition step, using a research quartz crystal microbalance (QCM) (Maxtek Inc., Cypress, CA).

5.2.3 Layer-by-Layer-Deposition

LbL deposition was carried out under ambient conditions using a home-built robotic system [249, 250]. All properly treated substrates were first dipped into the PEI solution for 5 min to deposit a primer layer, followed by rinsing with deionized water three times (20 sec each time) and drying with a stream of filtered air. After the first layer was adsorbed, the substrate was dipped into PMAA solution for another 5 minutes, followed by another rinsing and drying cycle to form one bilayer (BL). Starting from the second deposition cycle, the remaining layers were deposited using one minute dip times in PEO and PMAA solutions followed by the same rinsing and drying steps. The pH of PEO and PMAA solutions is shown as a subscript next to the abbreviations in the figures and text. For example, one bilayer of PEO(pH=2)/PMAA(pH=2) is abbreviated as 1 BL $PEO_2/PMAA_2$.

5.2.4 Film Characterization

The thickness of the LbL assembled films was measured using a α-SE ellipsometer (J. A. Wollam Co., Inc., Lincoln, NE) in transparent mode. The reported film thickness is the average of three measurements. The mass of each deposited layer was measured using a QCM with a frequency range of 3.8 - 6 MHz. The 5 MHz quartz crystals were plasma treated for 5 min at 10.5 W prior to deposition, then inserted in a QCM holder and dipped

into the corresponding solutions. After each deposition, the crystal was rinsed and dried and then left on the microbalance to stabilize for 5 minutes. The reported film mass is the average of the last ten data points obtained after 5 minutes of measurement. Thermal properties were measured using a TA Instruments Q200 differential scanning calorimeter. All DSC measurements were performed under a nitrogen atmosphere using S5 Tzero aluminum pans and lids. The sample weight ranged between 3 mg and 5 mg. The samples were scanned from -30 °C to 250 °C at heating and cooling rate of 10 °C min^{-1}. A FTIR spectrometer (Nicolet 6700 Series, Thermo Electron Corporation) was used to collect all spectra of the 4 and 10 BL PEO_2/$PMAA_2$ thin films, using a single reflection diamond. All infrared spectra were collected using a liquid nitrogen-cooled mercury-cadmium-telluride (MCT) detector at 32 scans per spectrum and a resolution of 4 cm^{-1}. All spectra were corrected with a background subtraction of the polystyrene spectrum. Samples were clamped onto the surface of a diamond attenuated total reflectance (ATR) crystal with a surface area of 1.8 mm^2 using the anvil from the Quest accessory (Specac Inc.) at a constant load capacity of 18.14 kg.

5.2.5 Gas Permeation System

Gas permeability coefficients of CO_2 and N_2 were measured using the constant-volume, variable-pressure apparatus described in Section 4.2.4. The upstream pressure was varied between 1 and 3 atm and was measured using a pressure transducer. Measurements were carried out at 20 ºC, 35 ºC, and 50 ºC using UHP grade gases. The calibrated downstream volume for these tests was 36 cm^3.

5.3 RESULTS AND DISCUSSION

5.3.1 Multilayer Film Growth

LbL assembly of PEO/PMAA thin films is driven by hydrogen bonding between the carboxylic acid groups of PMAA (as H-bond donors) and the ether groups of PEO (as H-bond acceptors) [261]. Although the ability of PEO to act as a hydrogen bond acceptor is unaffected by the solution pH due to its non-ionic nature, the ability of PMAA to act as a hydrogen bond donor is highly dependent on the assembling pH. As reported by deLongchamp et al. [262], at a pH of 4.5 the repulsive force between COO- groups is large enough to prevent the growth of the PEO/PMAA assembly. Decreasing the assembling pH leads to a greater film thickness, due to the protonation of COO^- groups, which reduces the intensity of the repulsive force and provides more H-bond donor sites. The influence of pH on the film thickness becomes negligible when $pH \leq 2$ due to complete protonation of carboxylic acid groups on PMAA. At a pH between 2 and 4, there is a modulation window in which PMAA is partially ionized, as shown in Figure 50. The thickness of these assemblies was measured as a function of layer pairs deposited at varying pH, as shown in Figure 51. Following an initial nonlinear growth period for the first six bilayers, linear growth was observed for PEO/PMAA assemblies. This type of growth profile is consistent with previous studies [262-264], where a linear growth profile was observed following an "induction period" of exponential growth. This trend is commonly observed in systems that experience significant interdiffusion between the two polymers due to low charge densities.

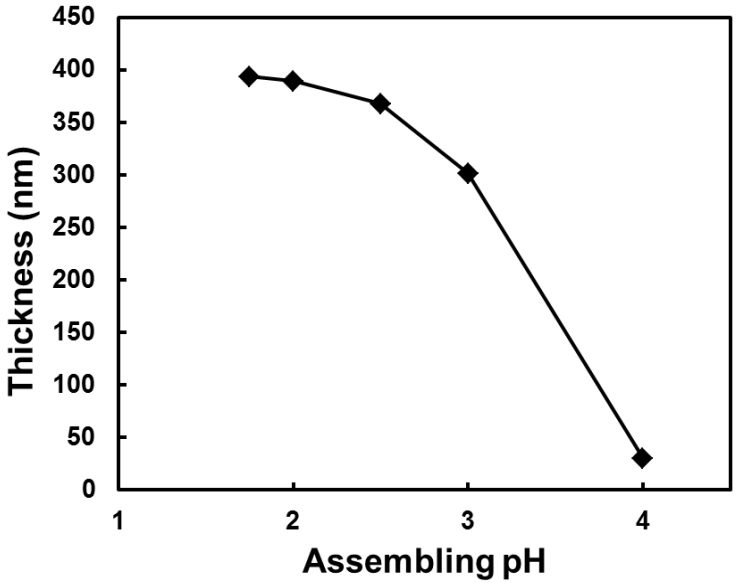

Figure 50. Film thickness as a function of deposition pH for 10 BL PEO/PMAA assemblies.

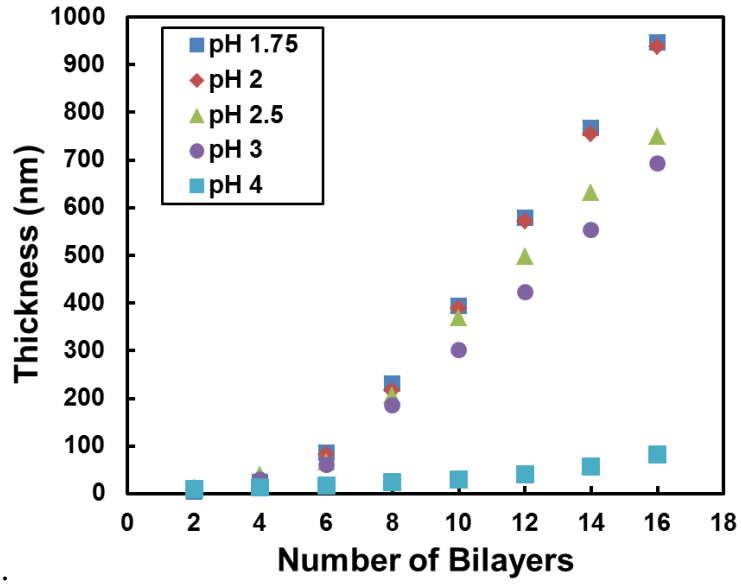

Figure 51. Film thickness as a function of the number of bilayers deposited for PEO/PMAA assemblies made with varying deposition pH.

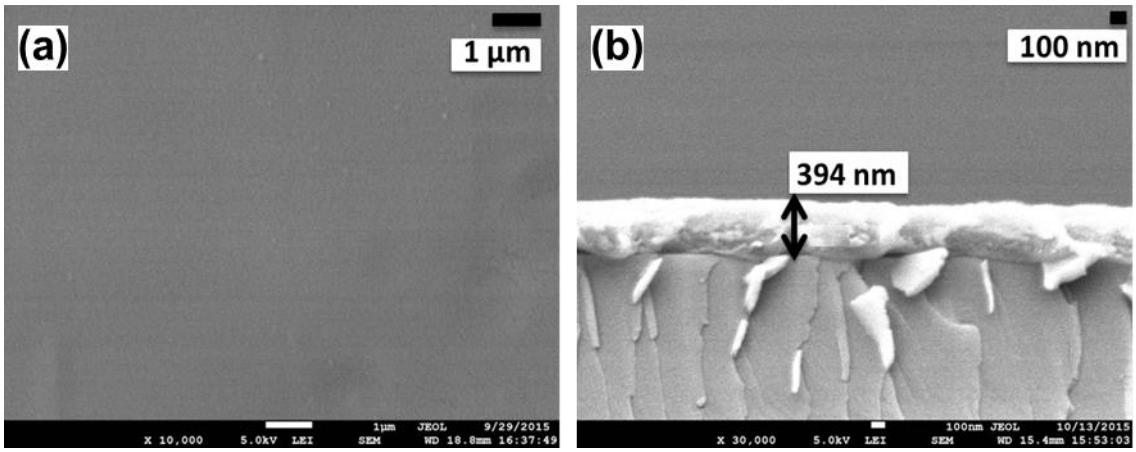

Figure 52. (a) SEM surface image (x10,000) and (b) cross-sectional image (x30,000) of a $PEO_2/PMAA_2$ thin film.

Figure 52a presents a surface SEM image (x10,000) of a 10 BL $PEO_2/PMAA_2$ film deposited on a silicon wafer substrate. The smooth surface indicates that the conformal PEO/PMAA coating is free of macroscopic defects. The cross-sectional image (Figure 52b) confirms the deposition of a ~0.4 µm polymer membrane over the silicon substrate.

Surface morphologies of these PEO/PMAA assemblies were examined using AFM (Figure 53a-d). Root-mean-square (RMS) roughness was measured using AFM over a larger area (30 µm x 30 µm). All films are very smooth surface with roughness below 14 nm. The developed interfacial area ratio (S_{dr}), shown in Figure 53f, represents the percentage of additional surface area contributed by the texture as compared to an ideal plane the size of the measured region. The S_{dr} increased slightly as the number of bilayers increased; however no strong conclusion could be made since some measurements were within the error of each other.

$$S_{dr} = \frac{\text{Texture Surface Area} - \text{Cross-Sectional Area}}{\text{Cross-Sectional Area}} \quad (85)$$

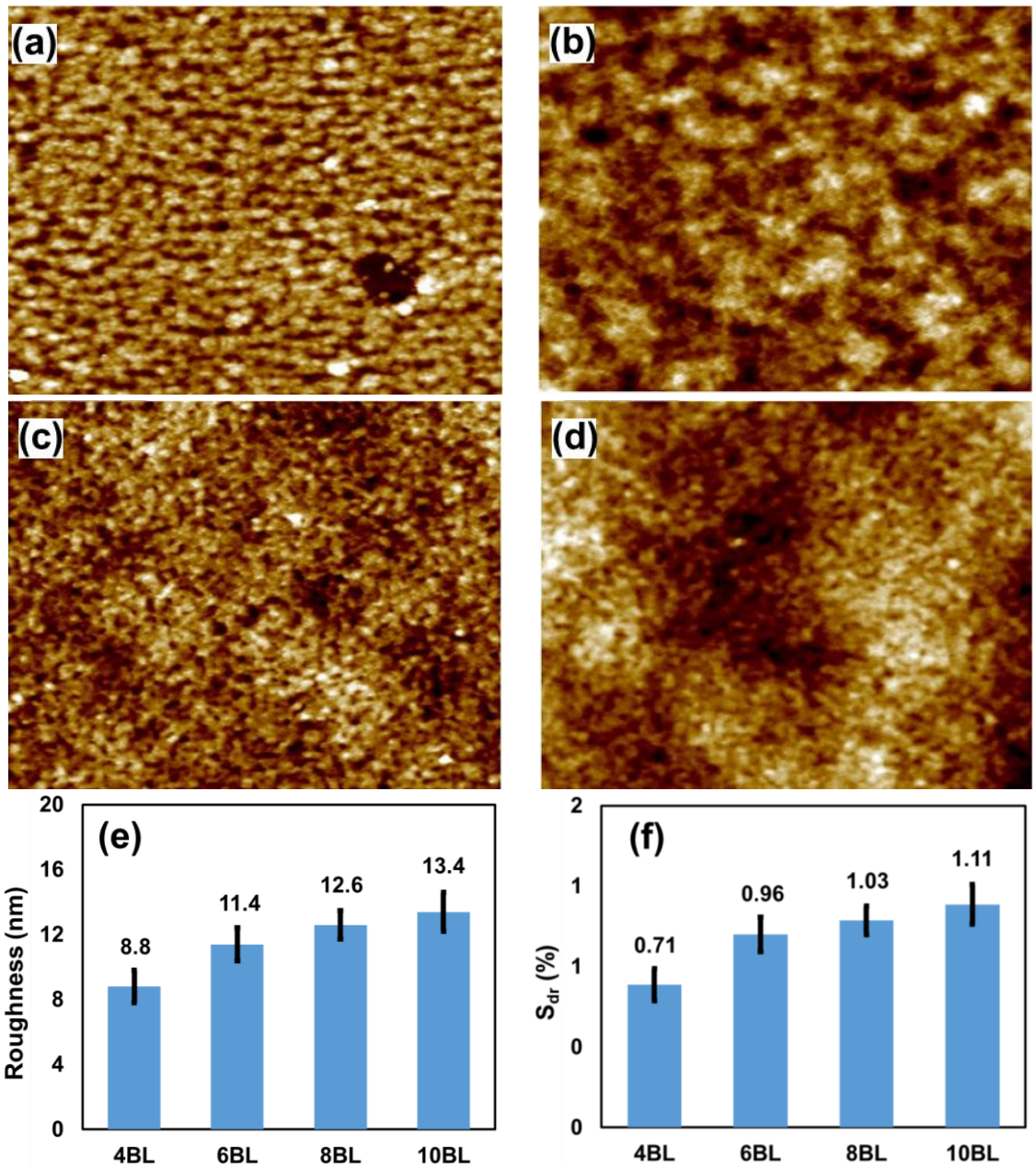

Figure 53. AFM images (3.5 µm x 3.5 µm) of $PEO_2/PMAA_2$ LbL assemblies. (a) 4 BL; (b) 6 BL; (c) 8 BL; (d) 10 BL; (e) Root-mean-square roughness; and (f) Developed interfacial area ratio.

5.3.2 FTIR Spectroscopy Analysis

FTIR spectra of 4 BL and 10 BL $PEO_2/PMAA_2$ thin films were collected to confirm the composition and bonding of these assemblies. From the sample spectra (Figure 54), the presence of PEO and PMAA in the films is clear. Peaks at 820, 1030-1110, and 1120-1170 cm^{-1} are similar to C-O-C stretch and CH_2 peaks reported for PEO in its amorphous state (855, 1107, and 1140 cm^{-1}) [265]. The absorption peaks at 1700-1750 cm^{-1} indicate carbonyl C=O stretching [266, 267] typical of poly(carboxylic acid), such as PMAA. A peak corresponding to intermolecularly bonded COOH will typically grow at ~1750 cm^{-1} at the expense of a peak located at ~1710 cm^{-1} that corresponds to intramolecular bonded COOH. Deconvolution of this absorption peak would provide information about the degree of intra- and intermolecular hydrogen bonds within the assembly. Evidence of hydroxyl-hydrogen bonding is demonstrated by the broad absorption peak at ~3000 cm^{-1} [268, 269].

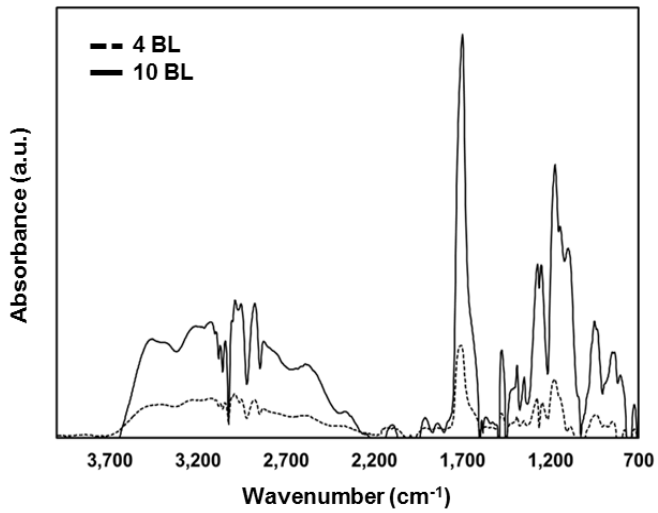

Figure 54. FTIR spectra of 4 BL and 10 BL $PEO_2/PMAA_2$ thin films deposited on a polystyrene substrate.

5.3.3 Thin Film Crystallinity

Table 12 shows the second heating scan results for 20, 30, and 40 BL freestanding $PEO_2/PMAA_2$ films cycled between -50 °C and 250 °C. A single glass transition temperature was observed for all samples, indicating a macroscopically homogeneous structure within the assembly. A high-temperature melting peak around 62 °C was also observed in all samples (associated with PEO). It should be noted that the thermal properties of these assemblies may vary significantly with polymer aging and annealing conditions.

Table 12. Thermal properties of $PEO_2/PMAA_2$ thin films.

	T_m (°C)	ΔH_m (J/g)	T_g (°C)
20BL $PEO_2/PMAA_2$	63.3	38.5	161.5
30BL $PEO_2/PMAA_2$	62.7	30.0	157.3
40BL $PEO_2/PMAA_2$	62.1	26.8	158.5

Polymer crystallinity plays an important role in gas permeability due to the impermeable nature of polymer crystals. For this reason, the crystallinity of PEO within the multilayer assembly is analyzed. The crystallinity (X_c) is calculated based on the following equation [261]:

$$X_C = \frac{\Delta H\, \phi}{\Delta H^{\circ}} \tag{86}$$

where ΔH is the enthalpy of melting of PEO in the LbL film (Table 12), ϕ is the polymer's weight fraction, and ΔH_o is the enthalpy of melting of 100% crystalline PEO (188 J g^{-1}) [270]. Assuming that the weight fraction of PEO within the assembly is 27 wt% (according

to QCM results), the crystallinity of PEO within the assembly is 5.5%, 4.3%, and 3.8%, for 20, 30, and 40 bilayer films, respectively.

5.3.4 Gas Separation Properties

Figure 55 presents the transmission rate of CO_2 and N_2 for PS+PEO_2/$PMAA_2$ films as a function of the number of bilayers. Prior to depositing the PEO/PMAA, gas permeation tests were performed with the neat polystyrene film to characterize the gas permeability through the substrate in the absence of a polymer coating. The CO_2 and N_2 permeabilities through the 25 μm polystyrene substrate were estimated to be 9.0 and 0.4 barrers, respectively. After depositing the PEO/PMAA films, CO_2 and N_2 transmission rates typically decreased by up to two orders of magnitude, while overall film thickness increased by only 1.6% for the 10 BL film and 0.12% for the 4 BL film.

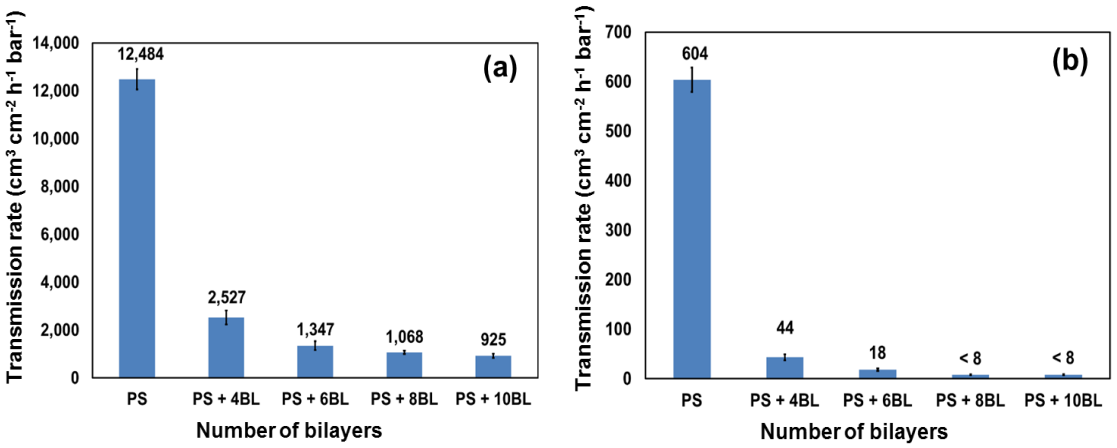

Figure 55. Transmission rate of (a) carbon dioxide and (b) nitrogen as a function of the number of bilayers for PEO_2/$PMAA_2$ thin films. Measurements were performed at 35 ºC and 15 psia differential pressure.

Coating permeability was decoupled from the total (PS+PEO/PMAA) permeability using a method previously described by Roberts et al. [271]. Figure 56 and

Table 13 present CO_2 and N_2 permeabilities as a function of the number of bilayers for $PEO_2/PMAA_2$ thin films. All experiments were performed at 35 ºC and 15 psia differential pressure.

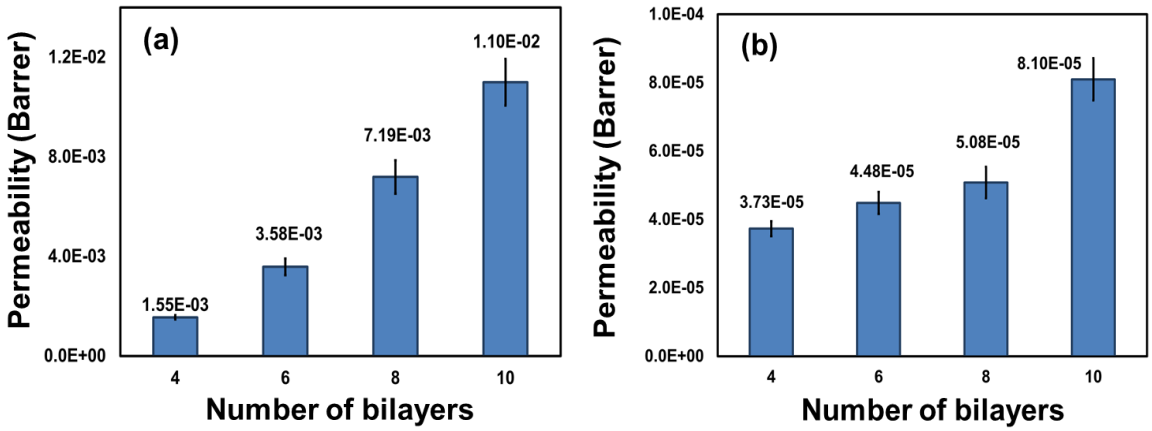

Figure 56. Permeability of (a) carbon dioxide and (b) nitrogen as a function of the number of bilayers deposited for $PEO_2/PMAA_2$ thin films. Measurements were performed at 35 ºC and 15 psia differential pressure.

Table 13. Carbon dioxide and nitrogen permeabilities of $PEO_2/PMAA_2$ thin films.

	Thickness (nm)	CO_2 Permeability	N_2 Permeability	CO_2/N_2 Selectivity
($PEO_2/PMAA_2$) - 4BL	27.98	1.55E-03	3.73E-05	41.55
($PEO_2/PMAA_2$) - 6BL	83.50	3.58E-03	4.48E-05	79.91
($PEO_2/PMAA_2$) - 8BL	217.15	7.19E-03	5.08E-05	141.54
($PEO_2/PMAA_2$) - 10BL	389.23	1.10E-02	8.10E-05	135.80

*Permeability is in Barrer

As film thickness is increased, the permeability of both gases, CO_2 and N_2, increases. This behavior is attributed to a reduction in film's crystallinity as film's thickness increases. Gas selectivity is calculated as the ratio of pure gas permeabilities (P_i/P_j). The CO_2/N_2 selectivity increases as the number of bilayers increase. Given that the

kinetic diameters of N_2 (3.64 A) and CO_2 (3.3 A) are very similar, these results confirm that there is a favorable interaction between the polymer film and CO_2, as reported in the literature for polymer membranes containing ether groups.

Permeability coefficients were measured at 20°C, 35°C, and 50°C to investigate the effect of temperature on the film's permeation properties. Figure 57 presents the natural logarithm of CO_2 and N_2 permeabilities for a 10 BL and a 6 BL $PEO_2/PMAA_2$ film as a function of the temperature inverse. Figure 58, on the other hand, shows the natural logarithm of CO_2 and N_2 permeabilities for a 10 BL $PEO_2/PMAA_2$ film and a 10 BL $PEO_4/PMAA_4$ film as a function of the temperature inverse. Both penetrants exhibit higher permeabilities at higher temperatures. The calculated activation energies are presented in Table 14. The activation energy for CO_2 permeation is not significantly affected by the change in pH or film thickness, however, the activation energy for N_2 permeation decreases with film thickness and deposition pH.

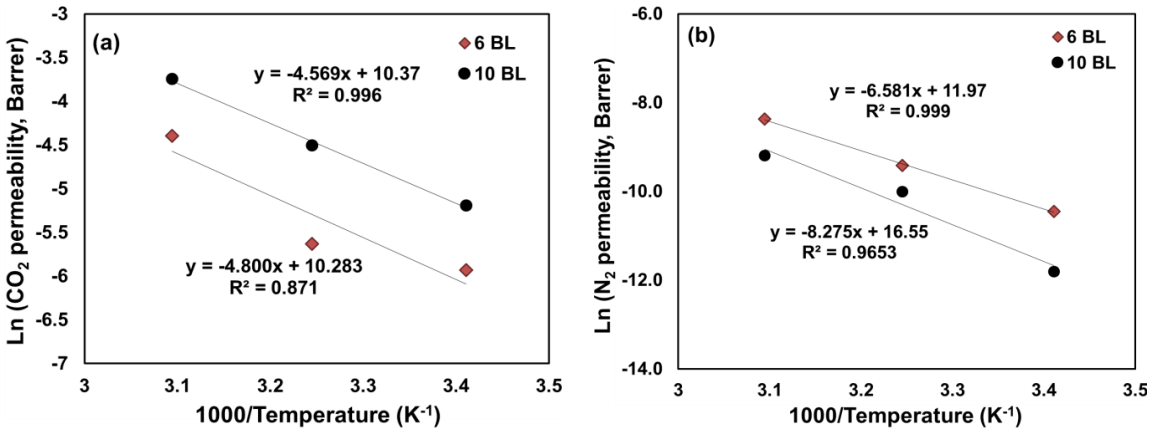

Figure 57. Permeability of (a) carbon dioxide and (b) nitrogen as a function of temperature for 6 BL and 10 BL $PEO_2/PMAA_2$ thin films. Measurements were performed at 15 psia differential pressure.

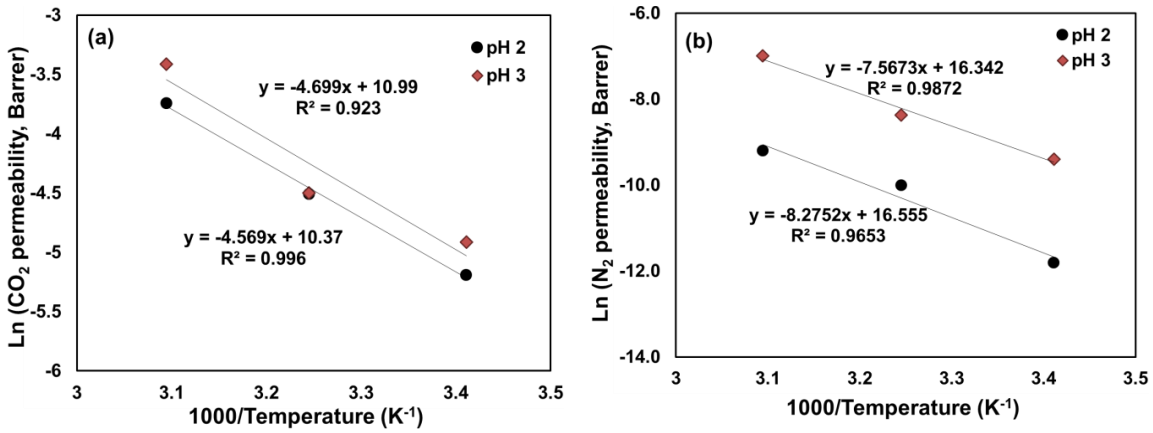

Figure 58. Permeability of (a) carbon dioxide and (b) nitrogen as a function of temperature for 10 BL PEO/PMAA thin films assembled at pH 2 and 3. Measurements were performed at 15 psia differential pressure.

Table 14. Activation energies for carbon dioxide and nitrogen permeation through PEO/PMAA thin films.

	CO_2 (J/mol)	N_2 (J/mol)
$(PEO_2/PMAA_2)_{10}$	37,987	68,800
$(PEO_2/PMAA_2)_6$	39,907	54,718
$(PEO_4/PMAA_4)_{10}$	39,067	62,914

The effect of changing polymer's deposition pH on gas permeability was investigated. Figure 59 and Table 15 present the permeabilities of CO_2 and N_2 for PEO/PMAA films deposited at pH levels of 2, 2.5, and 3. Altering the assembling pH leads to significant changes in N_2 permeability; however, the CO_2 permeability remained almost unaffected. Lowering the deposition pH causes a reduction in N_2 permeability; this behavior could be attributed to a reduction in film's free volume due to a higher degree of intramolecular bonding within the assembly.

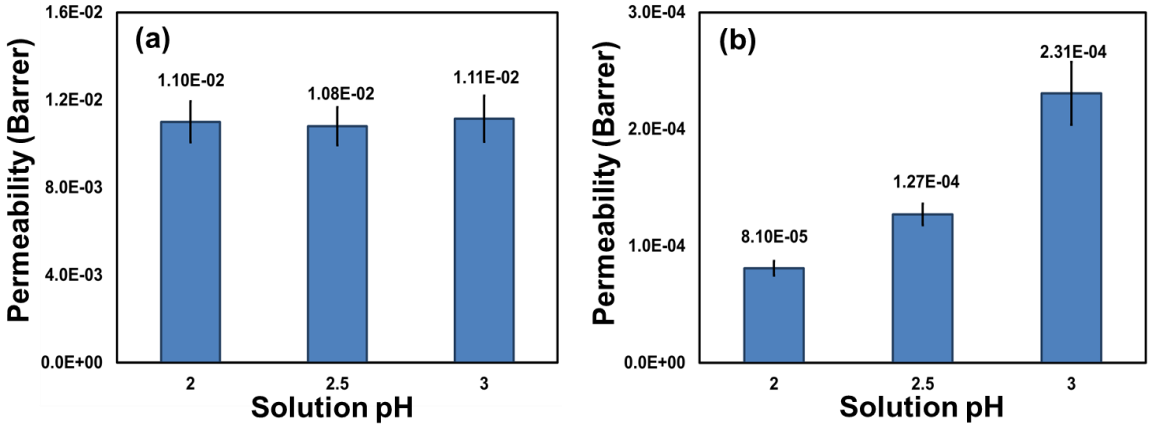

Figure 59. Permeability of (a) carbon dioxide and (b) nitrogen as a function deposition pH for 10 BL PEO/PMAA thin films. Measurements were performed at 35 ºC and 15 psia differential pressure.

Table 15. Carbon dioxide and nitrogen permeabilities of 10 BL PEO/PMAA thin films assembled at varying pH.

pH	Thickness (nm)	CO_2 Permeability	N_2 Permeability	CO_2/N_2 Selectivity
2	389.23	1.10E-02	8.10E-05	135.80
2.5	367.80	1.08E-02	1.27E-04	85.04
3	301.29	1.11E-02	2.31E-04	48.05

PEO molecular weight also influences gas permeability and selectivity. Figure 60 and Table 16 present CO_2 and N_2 permeabilities for PEO molecular weight of 10K g/mol, 100K g/mol, and 4,000K g/mol. The results show that the permeability of both gases increases as the PEO molecular weight increases from 10K to 100K and then decreases as the PEO molecular reaches 4,000K.

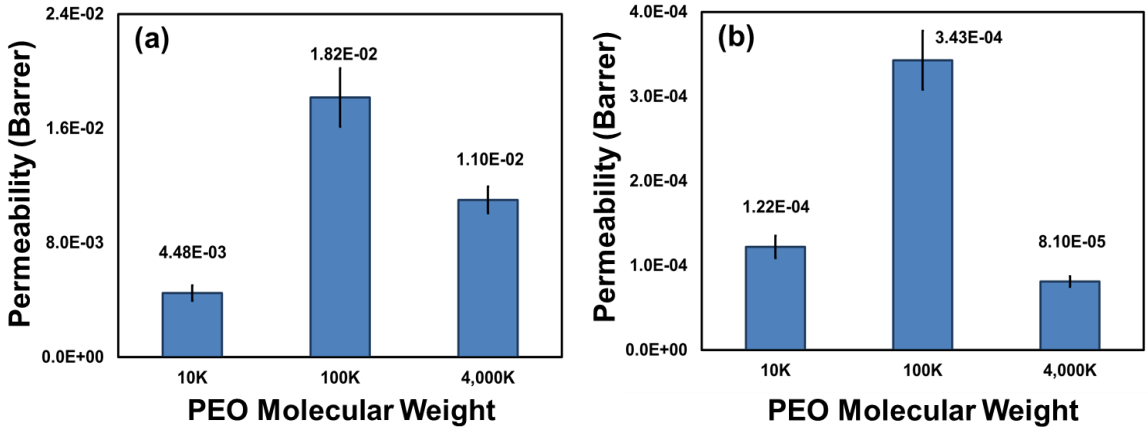

Figure 60. Permeability of (a) carbon dioxide and (b) nitrogen as a function of PEO molecular weight for 10 BL $PEO_2/PMAA_2$ thin films. Measurements were performed at 35 ºC and 15 psia differential pressure.

Table 16. Carbon dioxide and nitrogen permeabilities of 10 BL $PEO_2/PMAA_2$ thin films assembled at varying PEO molecular weights.

PEO Molecular Weight	CO_2 Permeability	N_2 Permeability	CO_2/N_2 Selectivity
10K	4.48E-03	1.22E-04	36.72
100K	1.82E-02	3.43E-04	53.06
4,000K	1.10E-02	8.10E-05	135.80

Figure 61 presents the upper bound limit reported by Robeson [108, 109] for CO_2/N_2 separation with homogeneous polymer membranes. The red squares in Figure 61 represent the LbL PEO/PMAA films studied in this work. The black dashed line corresponds to the highest CO_2/N_2 selectivity previously reported in the literature for homogeneous polymer membranes (86.25) [272]. The 8 BL and 10 BL $PEO_2/PMAA_2$ (green squares) exceed all CO_2/N_2 selectivities (142 and 136, respectively) previously reported.

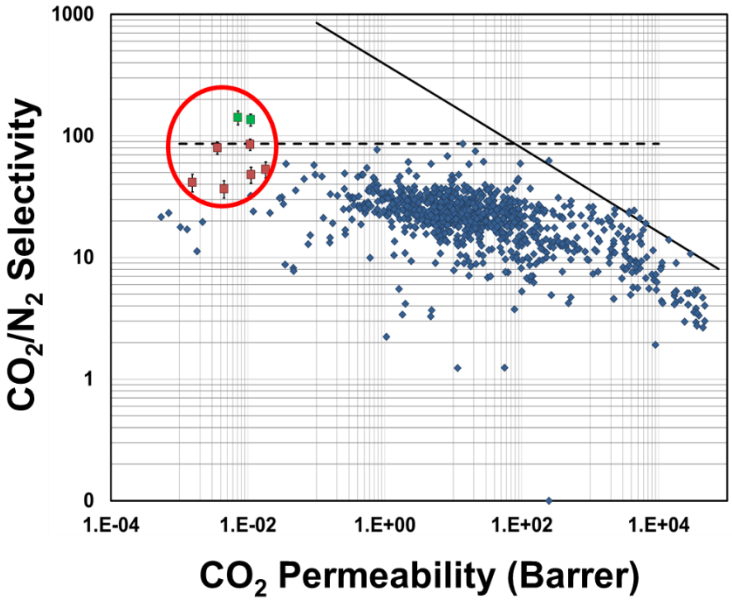

Figure 61. Robenson's upper bound plot showing CO_2 permeability and CO_2/N_2 selectivity of PEO/PMAA films and various other homogeneous polymer membranes (data from Membrane Society of Australasia database) [273].

5.4 CONCLUSIONS

This study demonstrates exceptionally high CO_2/N_2 selectivity in a hydrogen-bonded, LbL assembled PEO/PMAA membrane, which performs better than other similar homogenous polymer materials. The influence of membrane thickness, deposition pH, and PEO molecular weight on membrane's gas transport properties was studied. CO_2 and N_2 permeabilities of $PEO_2/PMAA_2$ assemblies increased as the number of bilayers increased. This behavior is attributed to a reduction in film's crystallinity as film's thickness increases. Maximum selectivities of 142 and 136 were measured for the 8 BL and 10 BL $PEO_2/PMAA_2$ thin films (these are the highest CO_2/N_2 selectivities reported to-date for this gas pair separation with a homogenous polymer film). The film's deposition pH was varied between 2, 2.5, and 3. The CO_2 permeability is unaffected by deposition pH;

however, the N_2 permeability increases with solution pH. PEO molecular weight was also varied between 10K, 100K, and 4,000K. Maximum CO_2 permeability was measured with PEO molecular weight of 100K, but the maximum CO_2/N_2 selectivity was observed at the highest molecular weight (4,000K). These unique thin films overcome the major drawback of common polymeric membranes (i.e., low selectivity), making them a significant milestone in the development of polymer membranes for gas separation.

CHAPTER VI

CONCLUSIONS AND RECOMMENDATIONS

6.1 CONCLUSIONS

Two novel designs for high-purity hydrogen production from hydrocarbon resources were investigated. The hypothesis that optimal patterning of reaction and separation may be used to manipulate local driving forces for product removal to improve catalyst utilization was demonstrated using multifunctional systems with segregated functionalities. This hypothesis was investigated for two designs: 1) a composite catalytic-permselective (CCP) membrane for water-gas shift (WGS) reaction coupled with H_2 or CO_2 removal and 2) a multifunctional catalyst for sorption-enhanced water-gas shift and sorption-enhanced methane steam reforming.

In Chapter II, a two-dimensional steady-state model was developed to describe a composite catalytic-permselective membrane for hydrogen purification from diesel autothermal reforming mixtures. The performance of the CCP membrane design was compared against the gas purification membrane design and the packed-bed membrane reactor design. A parametric analysis is performed varying two dimensionless design parameters: 1) the ratio of initial rate of desired permeate transport through the film to initial water-gas shift reaction rate (ξ) and 2) the ratio of permselective to catalytic film permeances for desired permeate (ζ). The comparison was made over a range of membrane capacities. Isothermal results at 723 K indicated that the CCP design, coupling the WGS reaction with palladium (Pd) membranes, is capable of significant improvements in overall

H_2 recoveries owing to a combination of reduction in CO exposure at the film's retentate surface and increased holdup of H_2 product in close proximity to the permselective film. These improvements were predicted under conditions such that H_2 permeation through the dense Pd membrane remains the limiting phenomenon for H_2 transport (i.e., $\zeta < 1$). For the case of coupling WGS reaction with a moderately CO_2-permselective polymeric film, the results indicated that the CCP design is capable of providing up to a 40% enhancement in CO_2-CO (product-reactant) separation, but at the cost of significant losses in CO_2-H_2 (product-product) separation rates. In the absence of surface inhibition by reactants, the CCP design also limits overall desired permeate recoveries, as compared to the equivalent PBMR design.

In Chapter III, two-dimensional unsteady-state models were developed to describe multifunctional catalyst particles for the application in sorption-enhanced methane steam reforming (SEMSR) and sorption-enhanced water-gas shift (SEWGS) processes. A side-by-side comparison of two multifunctional catalyst designs, core-shell and uniform-distributed, was presented. The comparison was provided in the context of typical adsorbent-to-catalyst volume ratio and dimensions reported in the literature for SEWGS and SEMSR processes. Results showed that the uniform-distributed design always has better adsorbent utilization than the core-shell design and, therefore, is preferable for SEWGS and SEMSR processes. The addition of the outer catalyst layer increases the resistance to CO_2 transport to adsorbent active sites, which translates to lower sorption rates. For the case of an adiabatic SEWGS process, the core-shell design reduced the hot-spot temperature by ~40 K when compared to the uniform-distributed design while

adsorbent utilization at breakthrough was reduced by 20%. Furthermore, as catalyst-shell thickness decreased, the core-shell design performance approached that of the uniform-distributed case. Variations in the adsorbent-to-catalyst volume ratio had no significant effect on the performance of either design.

Chapter IV presented an experimental demonstration of a Layer-by-Layer (LbL) film with low hydrogen and helium permeabilities. Quadlayers of polyethylenimine (PEI)/poly(acrylic acid)(PAA)/PEI/montmorillonite (MMT) were deposited on a polystyrene substrate to create transparent gas barrier assemblies. The impermeable clay platelets (MMT), together with highly interdiffused PEI and PAA mortar, formed a nanobrick wall structure that imparts significant light gas barrier. Permeability of both hydrogen and helium decreased as the number of quadlayers increased, showing two to three orders of magnitude improvement compared to commercial barriers. However, increasing the number of quadlayers from 5 to 10 did not improve the barrier properties. This lack of improvement is attributed to the expanded clay spacing and associated concentration reduction. The excellent performance of these thin films, combined with the simplicity of the LbL deposition method, makes these light gas barrier coatings an exciting opportunity for several packaging and protective applications.

In Chapter V, an experimental investigation of a highly selectivity LbL poly(ethylene oxide) (PEO)/poly(methacrylic acid) (PMAA) assembly for the separation of CO_2 and N_2 gases was presented. The influence of film thickness, deposition pH, and PEO molecular weight on film's gas transport properties was investigated. The results showed that CO_2 and N_2 permeability of $PEO_2/PMAA_2$ assemblies increased as the

number of bilayers increased. This behavior is attributed to a reduction in film's crystallinity as film's thickness increases. A maximum selectivity of 141.8 was measured for the 8 BL PEO_2/$PMAA_2$ film. The film's deposition pH was varied between 2, 2.5 and 3. The CO_2 permeability is unaffected by solution pH; however, N_2 permeability increases with solution pH. The molecular weight of PEO was also varied between 10K, 100K and 4,000K. Maximum CO_2 permeability measured with PEO molecular weight of 100K, but the maximum CO_2/N_2 selectivity was observed for the highest molecular weight (4,000K). This work demonstrates that LbL assembly technique can be used to fabricate gas purification membranes with good transport properties due to the ability to tune overall film's properties by varying different deposition parameters.

6.2 RECOMMENDATIONS

Further work is recommended for extending the concepts proven by the present work to other applications. In Chapter II, the hypothesis was demonstrated using a two-dimensional model with uniform temperature and pressure to facilitate a first system-level comparison of the CCP design. This model could be extended to include non-isothermal and external pressure gradient effects. Additionally, for the case of a moderately CO_2-permselective polymer film, permeation models were assumed to follow a first-order dependence upon driving force with constant selectivity and permeability values. More accurate gas permeation models of individual species could be developed for a range of driving forces and temperatures. The resulting permeation models can be implemented in the two-dimensional model to determine the optimal catalyst and membrane thicknesses necessary to achieve permeation and permselectivity enhancement via CCP design for a

specific set of membrane properties and feed conditions. Experimental validation of modeling results (Section 2.6.2) can be performed, following the CCP preparation procedure published by Kim et al. [167].

Experimental demonstration of the results presented in Chapter III is recommended. Synthesis of the core-shell design can be achieved following established experimental procedures published by Satrio et al. [200]. Adsorbent particles of optimum diameter can be fabricated using a small-scale drum-pelletizer and catalyst shells can be applied via dip-coating of particles in a slurry catalyst powder. Finally, the catalyst coating can be calcined in air between 800 ºC - 900 ºC for several hours. A cross-section scanning electron microscope could be employed to confirm core and shell thicknesses. For synthesizing the uniform-distributed design, adsorbent particles of optimum diameter can be impregnated with appropriate quantities of catalyst following the procedure established by Chanburanasiri et.al. [274]. After the catalyst is impregnated in the adsorbent support, the particle can be dried overnight and calcined for several hours.

Reaction-sorption experiments can be performed using a laboratory scale packed-bed reactor. The gas composition exiting the reactor can be analyzed via mass spectrometry or gas chromatography. Reaction experiments using a packed-bed of catalyst pellets can be performed to validate the kinetics employed in this theoretical study. Similarly, CO_2-sorption experiments using a packed-bed of adsorbent particles can be performed to validate the CO_2 uptake kinetics employed. Lastly, SEWGS and SEMSR experiments can be performed using 1) a packed-bed of core-shell multifunctional pellets, 2) a packed-bed of uniform-distributed multifunctional pellets, and 3) an equivalent mixed

bed of catalyst and adsorbent particles. The latter will provide the basis for experimental comparison between the one-pellet designs against the conventional two-pellet design.

Finally, owing to the versatility of the LbL method, there are many areas of study that can be pursued with regards to the gas transport properties of these films. Future work with these LbL systems could involve the investigation of the stability of gas transport properties over time. Several films can be made and then tested at different points in time to check if there are variations in these properties. The stability of gas transport properties in the presence of reformate mixtures could also be studied by monitoring the permeability and selectivity under different gas concentrations and moisture levels. Lastly, studying the impact of film morphology on these properties could be accomplished by changing the length of deposition time or the type of LbL deposition method employed for film fabrication (e.g., spray LbL or spin-coating LbL techniques).

REFERENCES

1. Au, S.S., J.S. Dranoff, and J.B. Butt, *Nonuniform activity distribution in catalyst particles: Benzene hydrogenation on supported nickel in a single pellet diffusion reactor*. Chemical Engineering Science, 1995. **50**(23): p. 3801-3812.

2. Dougherty, R.C. and X.E. Verykios, *Nonuniformly activated catalysts.* Catalysis Reviews Science and Engineering, 1987. **29**(1): p. 101-150.

3. Gavriilidis, A., A. Varma, and M. Morbidelli, *Optimal distribution of catalyst in pellets.* Catalysis Reviews—Science and Engineering, 1993. **35**(3): p. 399-456.

4. Verykios, X.E., R.W. Kluck, and D.L. Johnson, *Fixed-bed reactor simulation with nonuniformly activated catalyst pellets.* Modeling and simulation in engineering, 1983: p. 3-10.

5. Becker, E.R. and J. Wei, *Nonuniform distribution of catalysts on supports: I. Bimolecular Langmuir reactions.* Journal of Catalysis, 1977. **46**(3): p. 365-371.

6. James, W. and B. E. Robert, *The Optimum Distribution of Catalytic Material on Support Layers in Automotive Catalysis*, in *Catalysts for the Control of Automotive Pollutants*. 1975, American Chemical Society. p. 116-132.

7. Dietrich, W., et al., *Theoretical studies on multifunctional catalysts with integrated adsorption sites.* Chemical Engineering Journal, 2005. **107**(1–3): p. 103-111.

8. Baratti, R., et al., *Optimal catalyst activity profiles in Pellets—X. The role of catalyst loading.* Chemical Engineering Science, 1993. **48**(10): p. 1869-1881.

9. Lee, C.K., M. Morbidelli, and A. Varma, *Optimal catalyst activity profiles in pellets. 6. Optimization of the isothermal fixed-bed reactor with multiple zones.* Industrial & Engineering Chemistry Research, 1987. **26**(1): p. 167-170.

10. Szegner, J., K.L. Yeung, and A. Varma, *Effect of catalyst distribution in a membrane reactor: experiments and model.* AIChE Journal-American Institute of Chemical Engineers, 1997. **43**(8): p. 2059-2072.

11. Bell, A.T., et al., *Nonuniform catalyst distribution for inorganic membrane reactors: Theoretical considerations and preparation techniques.* Chemical Engineering Science, 1994. **49**(24): p. 4823-4838.

12. Johnson, J.B. and A. Pinto, *Ammonia synthesis process*. 1987, Google Patents.

13. Ramachandran, R. and R.K. Menon, *An overview of industrial uses of hydrogen.* International Journal of Hydrogen Energy, 1998. **23**(7): p. 593-598.

14. Rifkin, J., *The hydrogen economy: the creation of the worldwide energy web and the redistribution of power on earth Tarcher.* Putnam, New York, 2002.

15. Holladay, J.D., et al., *An overview of hydrogen production technologies.* Catalysis Today, 2009. **139**(4): p. 244-260.

16. Renzi, S. and R. Crawford, *Powering the next generation automobile: DaimlerChrysler's venture into fuel cell technology.* Corporate Environmental Strategy, 2000. **7**(1): p. 38-50.

17. Chalk, S.G., J.F. Miller, and F.W. Wagner, *Challenges for fuel cells in transport applications.* Journal of Power Sources, 2000. **86**(1): p. 40-51.

18. Stolten, D., *Hydrogen and fuel cells: fundamentals, technologies and applications*. 2010: John Wiley & Sons.

19. Armaroli, N. and V. Balzani, *The hydrogen issue.* ChemSusChem, 2011. **4**(1): p. 21-36.

20. Mazloomi, K. and C. Gomes, *Hydrogen as an energy carrier: prospects and challenges.* Renewable and Sustainable Energy Reviews, 2012. **16**(5): p. 3024-3033.

21. Badwal, S.P.S., S. Giddey, and C. Munnings, *Hydrogen production via solid electrolytic routes.* Wiley Interdisciplinary Reviews: Energy and Environment, 2013. **2**(5): p. 473-487.

22. Adamson, K.-A., *2008 Large Stationary Survey.* Fuel Cell Today, www. fuelcelltoday. com, August, 2008.

23. Chaubey, R., et al., *A review on development of industrial processes and emerging techniques for production of hydrogen from renewable and sustainable sources.* Renewable and Sustainable Energy Reviews, 2013. **23**: p. 443-462.

24. Erisman, J.W., et al., *How a century of ammonia synthesis changed the world.* Nature Geoscience, 2008. **1**(10): p. 636-639.

25. Maxwell, G.R., *Uses of Ammonia.* Synthetic Nitrogen Products: A Practical Guide to the Products and Processes, 2004: p. 199-203.

26. Jennings, J., *Catalytic ammonia synthesis: fundamentals and practice*. 2013: Springer Science & Business Media.

27. Lloyd, L., *Ammonia and methanol synthesis,* in *Handbook of Industrial Catalysts*. 2011, Springer. p. 397-437.

28. Hallale, N. and F. Liu, *Refinery hydrogen management for clean fuels production.* Advances in Environmental Research, 2001. **6**(1): p. 81-98.

29. Alves, J.J. and G.P. Towler, *Analysis of refinery hydrogen distribution systems.* Industrial & Engineering Chemistry Research, 2002. **41**(23): p. 5759-5769.

30. Gary, J.H., G.E. Handwerk, and M.J. Kaiser, *Petroleum refining: technology and economics*. 2007: CRC press.

31. Mohanty, S., D. Kunzru, and D. Saraf, *Hydrocracking: A review.* Fuel, 1990. **69**(12): p. 1467-1473.

32. Topsøe, H., B.S. Clausen, and F.E. Massoth, *Hydrotreating catalysis*. 1996: Springer.

33. Speight, J.G., *The chemistry and technology of petroleum*. 2014: CRC press.

34. Courty, P.R. and A. Chauvel, *Catalysis, the turntable for a clean future.* Catalysis today, 1996. **29**(1): p. 3-15.

35. Liu, F. and N. Zhang, *Strategy of purifier selection and integration in hydrogen networks.* Chemical Engineering Research and Design, 2004. **82**(10): p. 1315-1330.

36. Mapiour, M., *Kinetics and effects of H2 partial pressure on hydrotreating of heavy gas oil*. 2009, University of Saskatchewan Saskatoon.

37. Habashi, F., *Recent trends in extractive metallurgy*. Journal of Mining and Metallurgy, Section B: Metallurgy, 2009. **45**(1): p. 1-13.

38. Matthews, J., *Epitaxial growth*. 2012: Elsevier.

39. Gupta, R.B., *Hydrogen fuel: production, transport, and storage*. 2008: CRC Press.

40. Council, N.R., *The Hydrogen Economy: Opportunities, Costs, Barriers, and R&D Needs*. 2004, The National Academies Press Washington, DC.

41. Moreno, A.M., *Thermally integrated ceramic microreactors for hydrogen production.* 2010.

42. Brunetti, A., G. Barbieri, and E. Drioli, *A PEMFC and H< sub> 2</sub> membrane purification integrated plant.* Chemical Engineering and Processing: Process Intensification, 2008. **47**(7): p. 1081-1089.

43. kumar, J.A., P. Kalyani, and R. Saravanan, *Studies on PEM fuel cells using various alcohols for low power applications.* International Journal of Electrochemical Science, 2008. **3**(8): p. 961-969.

44. Vielstich, W., A. Lamm, and H.A. Gasteiger, *Handbook of Fuel Cells: Fundamentals Technology and Applications. Vol. 3, Fuel Cell Technology and Applications*. 2003: Wiley.

45. de Bruijn, F., *The current status of fuel cell technology for mobile and stationary applications.* Green chemistry, 2005. **7**(3): p. 132-150.

46. Kirubakaran, A., S. Jain, and R. Nema, *A review on fuel cell technologies and power electronic interface.* Renewable and Sustainable Energy Reviews, 2009. **13**(9): p. 2430-2440.

47. Larminie, J., A. Dicks, and M.S. McDonald, *Fuel cell systems explained*. Vol. 2. 2003: Wiley Chichester.

48. Zagoria, A. and R. Huycke, *Refinery hydrogen management: the big picture: Clean fuels.* Hydrocarbon processing, 2003. **82**(2): p. 41-46.

49. Kothari, R., D. Buddhi, and R.L. Sawhney, *Comparison of environmental and economic aspects of various hydrogen production methods.* Renewable and Sustainable Energy Reviews, 2008. **12**(2): p. 553-563.

50. Bossel, U., B. Eliasson, and G. Taylor, *The future of the hydrogen economy: bright or bleak?* Cogeneration and Distributed Generation Journal, 2003. **18**(3): p. 29-70.

51. Zoulias, E., et al., *A review on water electrolysis.* TCJST, 2004. **4**(2): p. 41-71.

52. Santos, D.M., C.A. Sequeira, and J.L. Figueiredo, *Hydrogen production by alkaline water electrolysis.* Química Nova, 2013. **36**(8): p. 1176-1193.

53. Zeng, K. and D. Zhang, *Recent progress in alkaline water electrolysis for hydrogen production and applications.* Progress in Energy and Combustion Science, 2010. **36**(3): p. 307-326.

54. Turner, J.A., *A realizable renewable energy future.* Science, 1999. **285**(5428): p. 687-689.

55. Conte, M., et al., *Hydrogen economy for a sustainable development: state-of-the-art and technological perspectives.* Journal of Power Sources, 2001. **100**(1): p. 171-187.

56. Haryanto, A., et al., *Current status of hydrogen production techniques by steam reforming of ethanol: a review.* Energy & Fuels, 2005. **19**(5): p. 2098-2106.

57. Shoko, E., et al., *Hydrogen from coal: production and utilisation technologies.* International Journal of Coal Geology, 2006. **65**(3): p. 213-222.

58. O'Hayre, R.P., et al., *Fuel cell fundamentals*. 2006: John Wiley & Sons New York.

59. Ockwig, N.W. and T.M. Nenoff, *Membranes for hydrogen separation.* Chemical Reviews, 2007. **107**(10): p. 4078-4110.

60. Shao, L., et al., *Polymeric membranes for the hydrogen economy: contemporary approaches and prospects for the future.* Journal of membrane science, 2009. **327**(1): p. 18-31.

61. Collot, A.-G., *Prospects for hydrogen from coal*. 2003: IEA Clean Coal Centre London.

62. Agrawal, R., M. Offutt, and M.P. Ramage, *Hydrogen economy-an opportunity for chemical engineers?* AIChE Journal, 2005. **51**(6): p. 1582-1589.

63. Sircar, S. and T. Golden, *Purification of hydrogen by pressure swing adsorption.* Separation Science and Technology, 2000. **35**(5): p. 667-687.

64. Yang, S.-I., et al., *Hydrogen separation by multi-bed pressure swing adsorption of synthesis gas.* Adsorption, 2008. **14**(4-5): p. 583-590.

65. Ruthven, D.M., S. Farooq, and K.S. Knaebel, *Pressure swing adsorption*. Vol. 480. 1994: VCH publishers New York.

66. Hinchliffe, A. and K. Porter, *A comparison of membrane separation and distillation.* Chemical Engineering Research and Design, 2000. **78**(2): p. 255-268.

67. Adhikari, S. and S. Fernando, *Hydrogen membrane separation techniques.* Industrial & Engineering Chemistry Research, 2006. **45**(3): p. 875-881.

68. Yang, J., C.-H. Lee, and J.-W. Chang, *Separation of Hydrogen Mixtures by a Two-Bed Pressure Swing Adsorption Process Using Zeolite 5A.* Industrial & Engineering Chemistry Research, 1997. **36**(7): p. 2789-2798.

69. Strathmann, H., *Membrane separation processes: current relevance and future opportunities.* AIChE Journal, 2001. **47**(5): p. 1077-1087.

70. Baker, R.W., *Future directions of membrane gas separation technology.* Industrial & Engineering Chemistry Research, 2002. **41**(6): p. 1393-1411.

71. Bernardo, P., E. Drioli, and G. Golemme, *Membrane gas separation: a review/state of the art.* Industrial & Engineering Chemistry Research, 2009. **48**(10): p. 4638-4663.

72. Kim, D., *Pure Hydrogen from Ethanol via Integrated Micro-Membrane Networks.* 2010.

73. Gallucci, F., et al., *Recent advances on membranes and membrane reactors for hydrogen production.* Chemical Engineering Science, 2013. **92**: p. 40-66.

74. McBride, R.B., and D. L. McKinley, *A New Hydrogen Recovery Route.* Chemical Engineering Progress, 1965. **61**(3): p. 81.

75. Mardilovich, P.P., et al., *Defect-free palladium membranes on porous stainless-steel support.* American Institute of Chemical Engineers. AIChE Journal, 1998. **44**(2): p. 310.

76. Deshpande, K., et al., *SOI-supported microdevice for hydrogen purification using palladium–silver membranes.* Microelectromechanical Systems, Journal of, 2010. **19**(2): p. 402-409.

77. Nair, B.K.R. and M.P. Harold, *Pd encapsulated and nanopore hollow fiber membranes: synthesis and permeation studies.* Journal of membrane science, 2007. **290**(1): p. 182-195.

78. Ayturk, M.E., et al., *Synthesis of composite Pd-porous stainless steel (PSS) membranes with a Pd/Ag intermetallic diffusion barrier.* Journal of membrane science, 2006. **285**(1): p. 385-394.

79. Yun, S. and S. Ted Oyama, *Correlations in palladium membranes for hydrogen separation: A review.* Journal of Membrane Science, 2011. **375**(1–2): p. 28-45.

80. Zhang, X., G. Xiong, and W. Yang, *A modified electroless plating technique for thin dense palladium composite membranes with enhanced stability.* Journal of Membrane Science, 2008. **314**(1): p. 226-237.

81. Paglieri, S. and J. Way, *Innovations in palladium membrane research.* Separation & Purification Reviews, 2002. **31**(1): p. 1-169.

82. Hurlbert, R. and J. Konecny, *Diffusion of hydrogen through palladium.* The Journal of Chemical Physics, 1961. **34**(2): p. 655-658.

83. Caravella, A., G. Barbieri, and E. Drioli, *Modelling and simulation of hydrogen permeation through supported Pd-alloy membranes with a multicomponent approach.* Chemical Engineering Science, 2008. **63**(8): p. 2149-2160.

84. Yan, S., et al., *Thin palladium membrane formed in support pores by metal-organic chemical vapor deposition method and application to hydrogen separation.* Industrial & engineering chemistry research, 1994. **33**(3): p. 616-622.

85. Ayturk, M.E. and Y.H. Ma, *Electroless Pd and Ag deposition kinetics of the composite Pd and Pd/Ag membranes synthesized from agitated plating baths.* Journal of Membrane Science, 2009. **330**(1): p. 233-245.

86. Ye, J., G. Dan, and Q. Yuan. *The preparation of ultrathin palladium membrane*. in *Key Engineering Materials*. 1992. Trans Tech Publ.

87. Mattox, D.M., *Handbook of physical vapor deposition (PVD) processing*. 2010: William Andrew.

88. Hsieh, H., *Inorganic membranes for separation and reaction*. 1996: Elsevier.

89. Shu, J., et al., *Catalytic palladium-based membrane reactors: A review*. The Canadian Journal of Chemical Engineering, 1991. **69**(5): p. 1036-1060.

90. Gryaznov, V., *Hydrogen permeable palladium membrane catalysts.* Platinum Metals Rev, 1986. **30**(2): p. 68-72.

91. Miller, J.B., B.D. Morreale, and A.J. Gellman, *The effect of adsorbed sulfur on surface segregation in a polycrystalline Pd 70 Cu 30 alloy.* Surface Science, 2008. **602**(10): p. 1819-1825.

92. Kulprathipanja, A., et al., *Pd and Pd–Cu membranes: inhibition of H 2 permeation by H 2 S.* Journal of Membrane Science, 2005. **254**(1): p. 49-62.

93. Perry, J.D., K. Nagai, and W.J. Koros, *Polymer membranes for hydrogen separations.* MRS bulletin, 2006. **31**(10): p. 745-749.

94. Baker, R.W., *Gas separation.* Membrane Technology and Applications, Third Edition, 2012: p. 325-378.

95. Ismail, A.F., T. Matsuura, and K.C. Khulbe, *Gas Separation Membranes : Polymeric and Inorganic*. 2015, Cham: Springer.

96. Baker, R.W., *Membrane technology*. 2000: Wiley Online Library.

97. Li, N.N., et al., *Advanced membrane technology and applications*. 2011: John Wiley & Sons.

98. Wijmans, J. and R. Baker, *The solution-diffusion model: a review*. Journal of membrane science, 1995. **107**(1): p. 1-21.

99. Stern, S.A., *Polymers for gas separations: the next decade.* Journal of Membrane Science, 1994. **94**(1): p. 1-65.

100. Koros, W. and G. Fleming, *Membrane-based gas separation.* Journal of membrane science, 1993. **83**(1): p. 1-80.

101. Park, H.B. and Y.M. Lee, *Polymeric membrane materials and potential use in gas separation.* Advanced Membrane Technology and Applications, 2008: p. 633-669.

102. Graham, T., *LV. On the absorption and dialytic separation of gases by colloid septa.* The London, Edinburgh, and Dublin Philosophical Magazine and Journal of Science, 1866. **32**(218): p. 401-420.

103. Koros, W., et al., *Polymeric membrane materials for solution-diffusion based permeation separations.* Progress in Polymer Science, 1988. **13**(4): p. 339-401.

104. Matteucci, S., et al., *Transport of gases and vapors in glassy and rubbery polymers.* Materials science of membranes for gas and vapor separation, 2006. **1**: p. 47.

105. Behling, R., et al., *The separation of hydrocarbons from waste vapor streams*, in *Membrane separations in chemical engineering*. 1989.

106. Van Amerongen, G.J., *The permeability of different rubbers to gases and its relation to diffusivity and solubility.* Journal of Applied Physics, 1946. **17**(11): p. 972-985.

107. Lin, H., et al., *Plasticization-enhanced hydrogen purification using polymeric membranes.* Science, 2006. **311**(5761): p. 639-642.

108. Robeson, L.M., *Correlation of separation factor versus permeability for polymeric membranes.* Journal of Membrane Science, 1991. **62**(2): p. 165-185.

109. Robeson, L.M., *The upper bound revisited.* Journal of Membrane Science, 2008. **320**(1–2): p. 390-400.

110. Freeman, B.D., *Basis of Permeability/Selectivity Tradeoff Relations in Polymeric Gas Separation Membranes.* Macromolecules, 1999. **32**(2): p. 375-380.

111. Mano, E.B. and L.A. Durao, *Review of laboratory methods for the preparation of polymer films.* Journal of Chemical Education, 1973. **50**(3): p. 228.

112. Mohr, J. and D. Paul, *Effect of casting solvent on the permeability of poly (4-methyl-1-pentene).* Polymer, 1991. **32**(7): p. 1236-1243.

113. Czichos, H., et al., *Springer Handbook of Materials Measurement Methods*. 2006: Springer.

114. Decher, G. and J.B. Schlenoff, *Multilayer thin films: sequential assembly of nanocomposite materials*. 2006: John Wiley & Sons.

115. Jan, C.S.J., *Layer-by-layer assembly of electrically conductive polymer thin films*. 2007, Texas A&M University.

116. Decher, G., J. Hong, and J. Schmitt, *Buildup of ultrathin multilayer films by a self-assembly process: III. Consecutively alternating adsorption of anionic and cationic polyelectrolytes on charged surfaces.* Thin solid films, 1992. **210**: p. 831-835.

117. Decher, G., *Fuzzy nanoassemblies: toward layered polymeric multicomposites.* science, 1997. **277**(5330): p. 1232-1237.

118. Ferreira, M. and M. Rubner, *Molecular-level processing of conjugated polymers. 1. Layer-by-layer manipulation of conjugated polyions.* Macromolecules, 1995. **28**(21): p. 7107-7114.

119. Shiratori, S.S. and M.F. Rubner, *pH-dependent thickness behavior of sequentially adsorbed layers of weak polyelectrolytes.* Macromolecules, 2000. **33**(11): p. 4213-4219.

120. Tzeng, P., C.R. Maupin, and J.C. Grunlan, *Influence of polymer interdiffusion and clay concentration on gas barrier of polyelectrolyte/clay nanobrick wall quadlayer assemblies.* Journal of Membrane Science, 2014. **452**(0): p. 46-53.

121. Tan, H.L., et al., *Temperature dependence of polyelectrolyte multilayer assembly.* Langmuir, 2003. **19**(22): p. 9311-9314.

122. Sui, Z., D. Salloum, and J.B. Schlenoff, *Effect of molecular weight on the construction of polyelectrolyte multilayers: stripping versus sticking.* Langmuir, 2003. **19**(6): p. 2491-2495.

123. Podsiadlo, P., et al., *Exponential growth of LBL films with incorporated inorganic sheets.* Nano letters, 2008. **8**(6): p. 1762-1770.

124. Kim, D., et al., *Highly Size-Selective Ionically Crosslinked Multilayer Polymer Films for Light Gas Separation.* Advanced Materials, 2014. **26**(5): p. 746-751.

125. Tzeng, P., et al., *Super Hydrogen and Helium Barrier with Polyelectolyte Nanobrick Wall Thin Film.* Macromolecular rapid communications, 2015. **36**(1): p. 96-101.

126. Priolo, M.A., et al., *Super gas barrier of transparent polymer− clay multilayer ultrathin films.* Nano letters, 2010. **10**(12): p. 4970-4974.

127. Dvoracek, C.M., et al., *Antimicrobial behavior of polyelectrolyte− surfactant thin film assemblies.* Langmuir, 2009. **25**(17): p. 10322-10328.

128. Hiller, J.A., J.D. Mendelsohn, and M.F. Rubner, *Reversibly erasable nanoporous anti-reflection coatings from polyelectrolyte multilayers.* Nature materials, 2002. **1**(1): p. 59-63.

129. Fu, J., et al., *Construction of antibacterial multilayer films containing nanosilver via layer-by-layer assembly of heparin and chitosan-silver ions complex.* Journal of Biomedical Materials Research Part A, 2006. **79**(3): p. 665-674.

130. Tiarks, F., K. Landfester, and M. Antonietti, *Encapsulation of carbon black by miniemulsion polymerization.* Macromolecular Chemistry and Physics, 2001. **202**(1): p. 51-60.

131. Tang, Z., et al., *Biomedical applications of layer-by-layer assembly: from biomimetics to tissue engineering.* Advanced Materials, 2006. **18**(24): p. 3203.

132. Phillips, C.A., *Review: modified atmosphere packaging and its effects on the microbiological quality and safety of produce.* International Journal of Food Science & Technology, 1996. **31**(6): p. 463-479.

133. Bhattacharya, S. and R. Tummala, *Integral passives for next generation of electronic packaging: application of epoxy/ceramic nanocomposites as integral capacitors.* Microelectronics Journal, 2001. **32**(1): p. 11-19.

134. Paul, D. and L. Robeson, *Polymer nanotechnology: nanocomposites.* Polymer, 2008. **49**(15): p. 3187-3204.

135. Ebina, T. and F. Mizukami, *Flexible Transparent Clay Films with Heat-Resistant and High Gas-Barrier Properties.* Advanced Materials, 2007. **19**(18): p. 2450-2453.

136. Krug, T., R. Ludwig, and G. Steiniger. *New developments in transparent barrier coatings*. in *Proceedings of The Annual Technical Conference-Society of Vacuum Coaters*. 1993. Society of Vacuum Coaters.

137. Jamieson, E. and A. Windle, *Structure and oxygen-barrier properties of metallized polymer film.* Journal of Materials Science, 1983. **18**(1): p. 64-80.

138. Roberts, A., et al., *Gas permeation in silicon-oxide/polymer (SiO x/PET) barrier films: role of the oxide lattice, nano-defects and macro-defects.* Journal of Membrane Science, 2002. **208**(1): p. 75-88.

139. Kalaitzidou, K., H. Fukushima, and L.T. Drzal, *Multifunctional polypropylene composites produced by incorporation of exfoliated graphite nanoplatelets.* Carbon, 2007. **45**(7): p. 1446-1452.

140. Carwford, G.P., *Flexible Flat Panel Displays*. 2005: John Wiley & Sons, Ltd.

141. Basu, S., et al., *Membrane-based technologies for biogas separations.* Chemical Society Reviews, 2010. **39**(2): p. 750-768.

142. Zhou, J., et al., *Mechanistic insight into highly efficient gas permeation and separation in a shape-persistent ladder polymer membrane.* Physical Chemistry Chemical Physics, 2014. **16**(13): p. 6075-6083.

143. Joseph, N., et al., *Layer-by-layer preparation of polyelectrolyte multilayer membranes for separation.* Polymer Chemistry, 2014. **5**(6): p. 1817-1831.

144. Stroeve, P., et al., *Gas transfer in supported films made by molecular self-assembly of ionic polymers.* Thin Solid Films, 1996. **284**: p. 708-712.

145. Alexandre, M. and P. Dubois, *Polymer-layered silicate nanocomposites: preparation, properties and uses of a new class of materials.* Materials Science and Engineering: R: Reports, 2000. **28**(1): p. 1-63.

146. Mittal, V., *Polymer layered silicate nanocomposites: a review.* Materials, 2009. **2**(3): p. 992-1057.

147. Biswas, M. and S.S. Ray, *Recent progress in synthesis and evaluation of polymer-montmorillonite nanocomposites*, in *New polymerization techniques and synthetic methodologies*. 2001, Springer. p. 167-221.

148. Lan, T., P.D. Kaviratna, and T.J. Pinnavaia, *Mechanism of clay tactoid exfoliation in epoxy-clay nanocomposites.* Chemistry of Materials, 1995. **7**(11): p. 2144-2150.

149. Priolo, M.A., D. Gamboa, and J.C. Grunlan, *Transparent Clay-Polymer Nano Brick Wall Assemblies with Tailorable Oxygen Barrier.* Acs Applied Materials & Interfaces, 2010. **2**(1): p. 312-320.

150. Takahashi, S., et al., *Gas barrier properties of butyl rubber/vermiculite nanocomposite coatings.* Polymer, 2006. **47**(9): p. 3083-3093.

151. Cussler, E., et al., *Barrier membranes.* Journal of Membrane Science, 1988. **38**(2): p. 161-174.

152. DeRocher, J.P., et al., *Barrier membranes with different sizes of aligned flakes.* Journal of membrane science, 2005. **254**(1): p. 21-30.

153. Fredrickson, G.H. and J. Bicerano, *Barrier properties of oriented disk composites.* The Journal of chemical physics, 1999. **110**(4): p. 2181-2188.

154. Leväsalmi, J.-M. and T.J. McCarthy, *Poly (4-methyl-1-pentene)-Supported Polyelectrolyte Multilayer Films: Preparation and Gas Permeability 1.* Macromolecules, 1997. **30**(6): p. 1752-1757.

155. Sullivan, D.M. and M.L. Bruening, *Ultrathin, Gas-Selective Polyimide Membranes Prepared from Multilayer Polyelectrolyte Films.* Chemistry of Materials, 2003. **15**(1): p. 281-287.

156. Stankiewicz, A.I. and J.A. Moulijn, *Process intensification: transforming chemical engineering.* Chemical Engineering Progress, 2000. **96**(1): p. 22-34.

157. Satterfield, C.N., *Heterogeneous catalysis in industrial practice.* 1991.

158. Uemiya, S., et al., *The water gas shift reaction assisted by a palladium membrane reactor.* Industrial & Engineering Chemistry Research, 1991. **30**(3): p. 585-589.

159. Fogler, H.S., *Elements of Chemical Reaction Engineering*. Fourth Edition ed. 2005, New York: Prentice-Hall.

160. Zou, J. and W.W. Ho, *Hydrogen purification for fuel cells by carbon dioxide removal membrane followed by water gas shift reaction.* Journal of Chemical Engineering of Japan, 2007. **40**(11): p. 1011-1020.

161. Kikuchi, E., *Membrane reactor application to hydrogen production.* Catalysis Today, 2000. **56**(1): p. 97-101.

162. Wieland, S., T. Melin, and A. Lamm, *Membrane reactors for hydrogen production.* Chemical Engineering Science, 2002. **57**(9): p. 1571-1576.

163. Brunetti, A., et al., *Simulation study of water gas shift reaction in a membrane reactor.* Journal of membrane science, 2007. **306**(1): p. 329-340.

164. Dixon, A.G., *Innovations in Catalytic Inorganic membrane reactors*, in *Catalysis: Volume 14*. 1999, The Royal Society of Chemistry. p. 40-92.

165. Huang, J., L. El-Azzami, and W. Ho, *Modeling of CO< sub> 2</sub>-selective water gas shift membrane reactor for fuel cell.* Journal of membrane science, 2005. **261**(1): p. 67-75.

166. Romero, E.L. and B.A. Wilhite, *Composite Catalytic-Permselective Membranes: Modeling Analysis for H< sub> 2</sub> Purification Assisted by Water-Gas-Shift Reaction.* Chemical Engineering Journal, 2012.

167. Kim, D., K. Barnett, and B.A. Wilhite, *Experimental demonstration of enhanced hydrogen permeation in palladium via a composite catalytic-permselective membrane.* AIChE Journal, 2012: p. n/a-n/a.

168. Wilhite, B.A., *Composite Catalytic-Permselective Membranes: A Strategy for Enhancing Selectivity and Permeation Rates via Reaction and Diffusion.* Industrial & Engineering Chemistry Research, 2011. **50**(17): p. 10185-10193.

169. Wilhite, B.A., et al., *High-Purity Hydrogen Generation in a Microfabricated 23 wt% Ag–Pd Membrane Device Integrated with 8: 1 LaNi0. 95Co0. 05O3/Al2O3 Catalyst.* Advanced Materials, 2006. **18**(13): p. 1701-1704.

170. Stevens, R.W., et al., *Sorption-enhanced water gas shift reaction by sodium-promoted calcium oxides.* Fuel, 2010. **89**(6): p. 1280-1286.

171. Ochoa-Fernández, E., et al., *Process design simulation of H 2 production by sorption enhanced steam methane reforming: evaluation of potential CO 2 acceptors.* Green Chemistry, 2007. **9**(6): p. 654-662.

172. Barelli, L., et al., *Hydrogen production through sorption-enhanced steam methane reforming and membrane technology: a review.* Energy, 2008. **33**(4): p. 554-570.

173. Harrison, D.P., *Sorption-enhanced hydrogen production: a review.* Industrial & engineering chemistry research, 2008. **47**(17): p. 6486-6501.

174. Abanades, J.C. and D. Alvarez, *Conversion limits in the reaction of CO2 with lime.* Energy & Fuels, 2003. **17**(2): p. 308-315.

175. Stendardo, S. and P.U. Foscolo, *Carbon dioxide capture with dolomite: A model for gas–solid reaction within the grains of a particulate sorbent.* Chemical Engineering Science, 2009. **64**(10): p. 2343-2352.

176. Huijgen, W.J.J. and R.N.J. Comans, *Carbon dioxide sequestration by mineral carbonation: Literature review*. 2003: Energy research Centre of the Netherlands ECN.

177. Jang, H.M., W.R. Kang, and K.B. Lee, *Sorption-enhanced water gas shift reaction using multi-section column for high-purity hydrogen production.* International Journal of Hydrogen Energy, 2013.

178. Jang, H.M., et al., *High-purity hydrogen production through sorption enhanced water gas shift reaction using K< sub> 2</sub> CO< sub> 3</sub>-promoted hydrotalcite.* Chemical Engineering Science, 2012. **73**: p. 431-438.

179. Van Selow, E., et al., *Improved sorbent for the sorption-enhanced water-gas shift process.* Energy Procedia, 2011. **4**: p. 1090-1095.

180. Han, C. and D.P. Harrison, *Simultaneous shift reaction and carbon dioxide separation for the direct production of hydrogen.* Chemical Engineering Science, 1994. **49**(24): p. 5875-5883.

181. Hufton, J., et al. *Sorption enhanced reaction process (SERP) for the production of hydrogen*. in *Proceedings of the 2000 US DOE Hydrogen Program Review*. 2000.

182. Balasubramanian, B., et al., *Hydrogen from methane in a single-step process.* Chemical Engineering Science, 1999. **54**(15): p. 3543-3552.

183. Lopez Ortiz, A. and D.P. Harrison, *Hydrogen production using sorption-enhanced reaction.* Industrial & Engineering Chemistry Research, 2001. **40**(23): p. 5102-5109.

184. Grünewald, M. and D.W. Agar, *Enhanced catalyst performance using integrated structured functionalities.* Chemical Engineering Science, 2004. **59**(22): p. 5519-5526.

185. Mizsey, P., et al., *The kinetics of methanol decomposition: a part of autothermal partial oxidation to produce hydrogen for fuel cells.* Applied Catalysis A: General, 2001. **213**(2): p. 233-237.

186. Geankoplis, C., *Transport processes and separation process principles (includes unit operations)*. 2003: Prentice Hall Press.

187. Neurock, M., S.M. Stark, and M.T. Klein, *Molecular simulation of kinetic interactions in complex mixtures.* Chemical Industries-New York-Marcel Dekker, 1993: p. 55-55.

188. Perry, R.H., D.W. Green, and J.O. Maloney, *Perry's chemical engineers' handbook.* Vol. 7. 2008: McGraw-Hill New York.

189. Israni, S.H. and M.P. Harold, *Methanol Steam Reforming in Pd− Ag Membrane Reactors: Effects of Reaction System Species on Transmembrane Hydrogen Flux.* Industrial & Engineering Chemistry Research, 2010. **49**(21): p. 10242-10250.

190. Kim, D., et al., *Toward an integrated ceramic micro-membrane network: effect of ethanol reformate on palladium membranes.* Industrial & Engineering Chemistry Research, 2010. **49**(21): p. 10254-10261.

191. Aris, R., *Communication. Normalization for the Thiele Modulus.* Industrial & Engineering Chemistry Fundamentals, 1965. **4**(2): p. 227-229.

192. Carberry, J.J., *The micro-macro effectiveness factor for the reversible catalytic reaction.* AIChE Journal, 1962. **8**(4): p. 557-558.

193. Harold, M., et al., *catalysis with Inorganic.* MRS bulletin, 1994.

194. Moon, W.S. and S.B. Park, *Design guide of a membrane for a membrane reactor in terms of permeability and selectivity.* Journal of membrane science, 2000. **170**(1): p. 43-51.

195. Davis, T.A., *A column pre-ordering strategy for the unsymmetric-pattern multifrontal method.* ACM Transactions on Mathematical Software (TOMS), 2004. **30**(2): p. 165-195.

196. Albrecht, K.O., et al., *Application of a combined catalyst and sorbent for steam reforming of methane.* Industrial & Engineering Chemistry Research, 2010. **49**(9): p. 4091-4098.

197. Solsvik, J. and H.A. Jakobsen, *A Two Property Catalyst/Sorbent Pellet Design for the Sorption-Enhanced Steam–Methane Reforming Process: Mathematical Modeling and Numerical Analysis.* Energy Procedia, 2012. **26**: p. 31-40.

198. Rout, K., et al., *A numerical study of multicomponent mass diffusion and convection in porous pellets for the sorption-enhanced steam methane reforming and desorption processes.* Chemical Engineering Science, 2011. **66**(18): p. 4111-4126.

199. Morbidelli, M., A. Gavriilidis, and A. Varma, *Catalyst design: optimal distribution of catalyst in pellets, reactors, and membranes*. 2005: Cambridge University Press.

200. Satrio, J.A., B.H. Shanks, and T.D. Wheelock, *A combined catalyst and sorbent for enhancing hydrogen production from coal or biomass.* Energy & Fuels, 2007. **21**(1): p. 322-326.

201. Solsvik, J. and H.A. Jakobsen, *A numerical study of a two property catalyst/sorbent pellet design for the sorption-enhanced steam–methane reforming process: Modeling complexity and parameter sensitivity study.* Chemical Engineering Journal, 2011. **178**: p. 407-422.

202. Jackson, R., *Transport in porous catalysts*. 1977: Elsevier Scientific Publishing Company The Netherlands.

203. Hla, S.S., et al., *Kinetics of high-temperature water-gas shift reaction over two iron-based commercial catalysts using simulated coal-derived syngases.* Chemical Engineering Journal, 2009. **146**(1): p. 148-154.

204. Atwood, K., M. Arnold, and E. Appel, *Water-Gas Shift Reaction. Effect of Pressure on Rate over an Iron-Oxide-Chromium Oxide Catalyst.* Industrial & Engineering Chemistry, 1950. **42**(8): p. 1600-1602.

205. Xu, J. and G.F. Froment, *Methane steam reforming, methanation and water‐gas shift: I. Intrinsic kinetics.* AIChE Journal, 1989. **35**(1): p. 88-96.

206. Stanmore, B. and P. Gilot, *Review—calcination and carbonation of limestone during thermal cycling for CO< sub> 2</sub> sequestration.* Fuel Processing Technology, 2005. **86**(16): p. 1707-1743.

207. Neufeld, P.D., A.R. Janzen, and R.A. Aziz, *Empirical Equations to Calculate 16 of the Transport Collision Integrals Ω(l, s)* for the Lennard-Jones (12–6) Potential.* The Journal of Chemical Physics, 1972. **57**(3): p. 1100-1102.

208. Hirschfelder J O, C.C.F., Bird R B., *Molecular theory of gases and liquids*. 2nd Ed. ed. 1964, New York: Wiley.

209. Bird, R.B., W.E. Stewart, and E.N. Lightfoot, *Transport phenomena*. 2007: Wiley. com.

210. Damodharan, S., B.V.R. Kuncharam, and B.A. Wilhite, *Design of Cartridge-Based Ceramic Heat-Exchanger Microchannel Reformers for Process Intensification: Experiments and Simulations.* Energy & Fuels, 2013. **27**(8): p. 4411-4422.

211. Wakao, N. and T. Funazkri, *Effect of fluid dispersion coefficients on particle-to-fluid mass transfer coefficients in packed beds: correlation of Sherwood numbers.* Chemical Engineering Science, 1978. **33**(10): p. 1375-1384.

212. Seo, Y.-S., A. Shirley, and S. Kolaczkowski, *Evaluation of thermodynamically favourable operating conditions for production of hydrogen in three different reforming technologies.* Journal of Power Sources, 2002. **108**(1): p. 213-225.

213. Butcher, H., et al., *Design of an annular microchannel reactor (AMR) for hydrogen and/or syngas production via methane steam reforming.* International Journal of Hydrogen Energy, (0).

214. Edwards, M. and J. Richardson, *Gas dispersion in packed beds.* Chemical Engineering Science, 1968. **23**(2): p. 109-123.

215. Yagi, S., D. Kunii, and N. Wakao, *Studies on axial effective thermal conductivities in packed beds.* AIChE Journal, 1960. **6**(4): p. 543-546.

216. Satrio, J.A., B.H. Shanks, and T.D. Wheelock, *Development of a novel combined catalyst and sorbent for hydrocarbon reforming.* Industrial & Engineering Chemistry Research, 2005. **44**(11): p. 3901-3911.

217. Bieder, A., A. Gruniger, and R. von Rohr, *Deposition of SiO x diffusion barriers on flexible packaging materials by PECVD.* Surface and Coatings Technology, 2005. **200**(1): p. 928-931.

218. Duttagupta, S., et al., *Excellent surface passivation of heavily doped p+ silicon by low-temperature plasma-deposited SiO x/SiN y dielectric stacks with optimised*

antireflective performance for solar cell application. Solar Energy Materials and Solar Cells, 2014. **120**: p. 204-208.

219. Sothornvit, R., et al., *Effect of clay content on the physical and antimicrobial properties of whey protein isolate/organo-clay composite films.* LWT-Food Science and Technology, 2010. **43**(2): p. 279-284.

220. Tetsuka, H., et al., *Highly transparent flexible clay films modified with organic polymer: structural characterization and intercalation properties.* Journal of Materials Chemistry, 2007. **17**(33): p. 3545-3550.

221. Hagen, D.A., et al., *High gas barrier imparted by similarly charged multilayers in nanobrick wall thin films.* Rsc Advances, 2014. **4**(35): p. 18354-18359.

222. Xiang, F.M., et al., *Improving the Gas Barrier Property of Clay-Polymer Multi layer Thin Films Using Shorter Deposition Times.* Acs Applied Materials & Interfaces, 2014. **6**(9): p. 6040-6048.

223. Rajasekar, R., et al., *Electrostatically assembled layer-by-layer composites containing graphene oxide for enhanced hydrogen gas barrier application.* Composites Science and Technology, 2013. **89**: p. 167-174.

224. Svagan, A.J., et al., *Transparent Films Based on PLA and Montmorillonite with Tunable Oxygen Barrier Properties.* Biomacromolecules, 2012. **13**(2): p. 397-405.

225. Woodtli, J. and R. Kieselbach, *Damage due to hydrogen embrittlement and stress corrosion cracking.* Engineering Failure Analysis, 2000. **7**(6): p. 427-450.

226. Gupta, R.B., *Hydrogen fuel: production, transport, and storage.* CRC Press: 2008.

227. Schlapbach, L. and A. Zuttel, *Hydrogen-storage materials for mobile applications.* Nature, 2001. **414**(6861): p. 353-358.

228. Edwards, P.P., et al., *Hydrogen and fuel cells: Towards a sustainable energy future.* Energy Policy, 2008. **36**(12): p. 4356-4362.

229. Bley, W.G., *Helium leak detectors: from a laboratory device to dedicated industrial leak test units.* Vacuum, 1993. **44**(5): p. 627-632.

230. Burger, H.D., *Method of leak testing a test container with a tracer gas*. 1991, Google Patents.

231. Jönsson, P., T. Eagar, and J. Szekely, *Heat and metal transfer in gas metal arc welding using argon and helium.* Metallurgical and Materials Transactions B, 1995. **26**(2): p. 383-395.

232. Huheey, J.E., et al., *Inorganic chemistry: principles of structure and reactivity.* Pearson Education India, 2006.

233. Cho, A., *Helium-3 shortage could put freeze on low-temperature research.* Science, 2009. **326**(5954): p. 778-779.

234. Linner, M., *Hydrogen and Helium.* ChemMatters, 1985: p. 4.

235. News, N.

236. McDaniels, K., et al., *High strength-to-weight ratio non-woven technical fabrics for aerospace applications.* Cubic Tech Corp, 2009: p. 1-9.

237. McKeen, L.W., *Permeability properties of plastics and elastomers*. 2011: William Andrew.

238. Leterrier, Y., *Durability of nanosized oxygen-barrier coatings on polymers.* Progress in Materials Science, 2003. **48**(1): p. 1-55.

239. EVAL, *Hydrogen Fuel Cell Systems*. 2007, Kuraray Co. p. 1-6.

240. Sinha Ray, S. and M. Okamoto, *Polymer/layered silicate nanocomposites: a review from preparation to processing.* Progress in polymer science, 2003. **28**(11): p. 1539-1641.

241. Tsai Boh, C. and A. Wachtel James, *Barrier Properties of Ethylene-Vinyl Alcohol Copolymer in Retorted Plastic Food Containers*, in *Barrier Polymers and Structures*. 1990, American Chemical Society. p. 192-202.

242. Podsiadlo, P., et al., *Exponential growth of LBL films with incorporated inorganic sheets.* Nano Letters, 2008. **8**(6): p. 1762-1770.

243. Holder, K.M., et al., *Stretchable Gas Barrier Achieved with Partially Hydrogen-Bonded Multilayer Nanocoating.* Macromolecular Rapid Communications, 2014. **35**(10): p. 960-964.

244. Veerabadran, N.G., et al., *Organized Shells on Clay Nanotubes for Controlled Release of Macromolecules.* Macromolecular Rapid Communications, 2009. **30**(2): p. 99-103.

245. Li, Y.C., et al., *Intumescent All-Polymer Multilayer Nanocoating Capable of Extinguishing Flame on Fabric.* Advanced Materials, 2011. **23**(34): p. 3926-3931.

246. Jang, W.-S., I. Rawson, and J.C. Grunlan, *Layer-by-layer assembly of thin film oxygen barrier.* Thin Solid Films, 2008. **516**(15): p. 4819-4825.

247. Cussler, E., et al., *Barrier membranes.* Journal of Membrane Science, 1988. **38**(2): p. 161-174.

248. Ploehn, H.J. and C.Y. Liu, *Quantitative analysis of montmorillonite platelet size by atomic force microscopy.* Industrial & Engineering Chemistry Research, 2006. **45**(21): p. 7025-7034.

249. Gamboa, D., et al., *Note: Influence of rinsing and drying routines on growth of multilayer thin films using automated deposition system.* Review of Scientific Instruments, 2010. **81**(3).

250. Jang, W.S. and J.C. Grunlan, *Robotic dipping system for layer-by-layer assembly of multifunctional thin films.* Review of Scientific Instruments, 2005. **76**(10).

251. Yang, Y.-H., et al., *Super Gas Barrier of All-Polymer Multilayer Thin Films.* Macromolecules, 2011. **44**(6): p. 1450-1459.

252. Ladam, G., et al., *In Situ Determination of the Structural Properties of Initially Deposited Polyelectrolyte Multilayers.* Langmuir, 1999. **16**(3): p. 1249-1255.

253. Priolo, M.A., et al., *Influence of Clay Concentration on the Gas Barrier of Clay-Polymer Nanobrick Wall Thin Film Assemblies.* Langmuir, 2011. **27**(19): p. 12106-12114.

254. Schmitt, J., et al., *Internal Structure of Layer-By-Layer Adsorbed Polyelectrolyte Films - A Neutron and X-Ray Reflectivity Study.* Macromolecules, 1993. **26**(25): p. 7058-7063.

255. Bhide, B.D. and S.A. Stern, *Membrane processes for the removal of acid gases from natural gas. I. Process configurations and optimization of operating conditions.* Journal of Membrane Science, 1993. **81**(3): p. 209-237.

256. McKetta, J., W. Cunningham, and V. Luedeke, *Encyclopedia of Chemical Processing and Design*. 1978, Marcel Dekker, New York. p. 292–310.

257. Ghosal, K., et al., *Effect of Basic Substituents on Gas Sorption and Permeation in Polysulfone.* Macromolecules, 1996. **29**(12): p. 4360-4369.

258. Lin, H. and B.D. Freeman, *Gas solubility, diffusivity and permeability in poly(ethylene oxide).* Journal of Membrane Science, 2004. **239**(1): p. 105-117.

259. Ariga, K., J.P. Hill, and Q. Ji, *Layer-by-layer assembly as a versatile bottom-up nanofabrication technique for exploratory research and realistic application.* Physical Chemistry Chemical Physics, 2007. **9**(19): p. 2319-2340.

260. Bertrand, P., et al., *Ultrathin polymer coatings by complexation of polyelectrolytes at interfaces: suitable materials, structure and properties.* Macromolecular Rapid Communications, 2000. **21**(7): p. 319-348.

261. Xiang, F., et al., *Structural tailoring of hydrogen-bonded poly (acrylic acid)/poly (ethylene oxide) multilayer thin films for reduced gas permeability.* Soft matter, 2015. **11**(5): p. 1001-1007.

262. DeLongchamp, D.M. and P.T. Hammond, *Highly Ion Conductive Poly(ethylene oxide)-Based Solid Polymer Electrolytes from Hydrogen Bonding Layer-by-Layer Assembly.* Langmuir, 2004. **20**(13): p. 5403-5411.

263. Sukhishvili, S.A. and S. Granick, *Layered, erasable polymer multilayers formed by hydrogen-bonded sequential self-assembly.* Macromolecules, 2002. **35**(1): p. 301-310.

264. Gu, X., et al., *Local thermal-mechanical analysis of ultrathin interfacially mixed poly (ethylene oxide)/poly (acrylic acid) layer-by-layer electrolyte assemblies.* Thin Solid Films, 2011. **519**(18): p. 5955-5961.

265. Bailey, J., *FE; Koleske, JV Poly (ethylene Oxide)*. 1976, Academic Press: San Francisco, CA.

266. Painter, P., B. Brozoski, and M. Coleman, *FTIR studies of calcium and sodium ionomers derived from an ethylene–methacrylic acid copolymer.* Journal of Polymer Science: Polymer Physics Edition, 1982. **20**(6): p. 1069-1080.

267. Lu, X. and R. Weiss, *Phase behavior of blends of poly (ethylene glycol) and partially neutralized poly (acrylic acid).* Macromolecules, 1995. **28**(9): p. 3022-3029.

268. Nishi, S. and T. Kotaka, *Complex-forming poly (oxyethylene): poly (acrylic acid) interpenetrating polymer networks. 1. Preparation, structure, and viscoelastic properties.* Macromolecules, 1985. **18**(8): p. 1519-1525.

269. Lee, J.Y., P.C. Painter, and M.M. Coleman, *Hydrogen bonding in polymer blends. 3. Blends involving polymers containing methacrylic acid and ether groups.* Macromolecules, 1988. **21**(2): p. 346-354.

270. Cimmino, S., et al., *Evaluation of the equilibrium melting temperature and structure analysis of poly(ethylene oxide)/poly(methyl methacrylate) blends.* Die Makromolekulare Chemie, 1990. **191**(10): p. 2447-2454.

271. Roberts, A., et al., *Gas permeation in silicon-oxide/polymer (SiO< sub> x</sub>/PET) barrier films: role of the oxide lattice, nano-defects and macro-defects.* Journal of Membrane Science, 2002. **208**(1): p. 75-88.

272. Polotskaya, G.A., et al., *Gas transport and structural features of sulfonated poly(phenylene oxide).* Journal of Applied Polymer Science, 1997. **66**(8): p. 1439-1443.

273. Thornton, A., *Membrane Society of Australasia*. 2012.

274. Chanburanasiri, N., et al., *Hydrogen production via sorption enhanced steam methane reforming process using Ni/CaO multifunctional catalyst.* Industrial & Engineering Chemistry Research, 2011. **50**(24): p. 13662-13671.

APPENDIX A

A.1 INTRODUCTION

The classical reaction-diffusion analysis of Thiele [1], Aris [2], and others assumes Ficks Law equimolar counter-diffusion, which while mathematically facile a solution, fails to account for multi-component diffusional effects of viscous- and Knudsen-diffusion phenomena. The Dusty-Gas Model (DGM) of species transport in a porous catalyst represents a modified Maxwell-Stefan model, incorporating viscous- (or pressure-driven) and Knudsen-diffusion, which is capable of greater accuracy in describing reaction-transport in a porous media. The derivation of the DGM assumes that the action of the porous material to be similar to that of a number of particles, fixed in space and obstructing the motion of the moving particles. In effect, the n-gaseous species present in the diffusing mixture are supplemented by an $(n+1)^{th}$ "dummy" species (also known as the "dust") of very massive molecules, constrained by unspecified external forces to have zero drift in velocity at all times [3]. The interaction of the gas with the dust molecules simulates their interaction with the immobile solid matrix of a porous medium. This assumption enables derivation of the following flux-composition relationship following momentum analysis of each species:

$$\sum_{j=1,\ j\neq i}^{n} \frac{x_i N_j - x_j N_i}{D_{ij}} - \frac{N_i}{D_{i,k}} = \frac{P}{RT}\nabla x_i + \frac{x_i}{RT}\left(1 + \frac{B_0 P}{\mu D_{i,k}}\right)\nabla P \qquad \text{A-1}$$

where:

B_0 permeability coefficient (m^2)

D_{ij} binary diffusion coefficient of a mixture *i* and *j* ($m^2\ s^{-1}$)

$D_{i,k}$ Knudsen diffusion coefficient of component *i* ($m^2\ s^{-1}$)

N_i flux of component *i* (mol $m^{-2}\ s^{-1}$)

P total pressure (Pa)

R universal gas constant (=8.314 J $mol^{-1}\ K^{-1}$)

T temperature (K)

μ dynamic viscosity (Pa s)

x_i mole fraction of component *i* (-)

A.2 ANALYTICAL SOLUTION OF DMG FOR QUATERNARY MIXTURE

The primary challenge to implementing this transport model (as is for Maxwell-Stefan diffusion in an unconfined fluid) is that equations are implicit in relating flux (N_i) to composition. In order to obtain an explicit analytical equation for each species molar flux, the following analysis is performed.

For *i* = 1

$$\sum_{j=2}^{4}\frac{x_1N_j-x_jN_1}{D_{1j}}-\frac{N_1}{D_{1,k}}=\frac{x_1N_2-x_2N_1}{D_{12}}+\frac{x_1N_3-x_3N_1}{D_{13}}+\frac{x_1N_4-x_4N_1}{D_{14}}-\frac{N_1}{D_{1,k}}=\frac{P}{RT}\nabla x_1+\frac{x_1}{RT}\left(1+\frac{B_0P}{\mu D_{1,k}}\right)\nabla P \quad \text{A-2a}$$

For *i* = 2

$$\sum_{j=1}^{4}\frac{x_2N_j-x_jN_2}{D_{2j}}-\frac{N_2}{D_{2,k}}=\frac{x_2N_1-x_1N_2}{D_{21}}+\frac{x_2N_3-x_3N_2}{D_{23}}+\frac{x_2N_4-x_4N_2}{D_{24}}-\frac{N_2}{D_{2,k}}=\frac{P}{RT}\nabla x_2+\frac{x_2}{RT}\left(1+\frac{B_0P}{\mu D_{2,k}}\right)\nabla P \quad \text{A-2b}$$

For *i* = 3

$$\sum_{j=1}^{4}\frac{x_3N_j-x_jN_3}{D_{3j}}-\frac{N_3}{D_{3,k}}=\frac{x_3N_1-x_1N_3}{D_{31}}+\frac{x_3N_2-x_2N_3}{D_{32}}+\frac{x_3N_4-x_4N_3}{D_{34}}-\frac{N_3}{D_{3,k}}=\frac{P}{RT}\nabla x_3+\frac{x_3}{RT}\left(1+\frac{B_0P}{\mu D_{3,k}}\right)\nabla P \quad \text{A-2c}$$

For *i* = 4

$$\sum_{j=1}^{4}\frac{x_4N_j-x_jN_4}{D_{4j}}-\frac{N_4}{D_{4,k}}=\frac{x_4N_1-x_1N_4}{D_{41}}+\frac{x_4N_2-x_2N_4}{D_{42}}+\frac{x_4N_3-x_3N_4}{D_{43}}-\frac{N_4}{D_{4,k}}=\frac{P}{RT}\nabla x_4+\frac{x_4}{RT}\left(1+\frac{B_0P}{\mu D_{4,k}}\right) \quad \text{A-2d}$$

These four implicit flux equations may be rearranged in terms of f(N_i) = scalar as follows:

For *i* = 1

$$-N_1\left(\frac{1}{D_{1,k}}+\frac{x_2}{D_{12}}+\frac{x_3}{D_{13}}+\frac{x_4}{D_{14}}\right)+x_1\left(\frac{N_2}{D_{12}}+\frac{N_3}{D_{13}}+\frac{N_4}{D_{14}}\right)=\frac{P}{RT}\nabla x_1+\frac{x_1}{RT}\left(1+\frac{B_0P}{\mu D_{1,k}}\right)\nabla P$$

A-3a

For *i* = 2

$$-N_2\left(\frac{1}{D_{2,k}}+\frac{x_1}{D_{21}}+\frac{x_3}{D_{23}}+\frac{x_4}{D_{24}}\right)+x_2\left(\frac{N_1}{D_{21}}+\frac{N_3}{D_{23}}+\frac{N_4}{D_{24}}\right)=\frac{P}{RT}\nabla x_2+\frac{x_2}{RT}\left(1+\frac{B_0P}{\mu D_{2,k}}\right)\nabla P$$

A-3b

For *i* = 3

$$-N_3\left(\frac{1}{D_{3,k}}+\frac{x_1}{D_{31}}+\frac{x_2}{D_{32}}+\frac{x_4}{D_{34}}\right)+x_3\left(\frac{N_1}{D_{31}}+\frac{N_2}{D_{32}}+\frac{N_4}{D_{34}}\right)=\frac{P}{RT}\nabla x_3+\frac{x_3}{RT}\left(1+\frac{B_0P}{\mu D_{3,k}}\right)\nabla P$$

A-3c

For *i* = 4

$$-N_4\left(\frac{1}{D_{4,k}}+\frac{x_1}{D_{41}}+\frac{x_2}{D_{42}}+\frac{x_3}{D_{43}}\right)+x_4\left(\frac{N_1}{D_{41}}+\frac{N_2}{D_{42}}+\frac{N_3}{D_{43}}\right)=\frac{P}{RT}\nabla x_4+\frac{x_4}{RT}\left(1+\frac{B_0P}{\mu D_{4,k}}\right)\nabla P$$

A-3d

Define

$$A_{11}=\frac{1}{D_{1,k}}+\frac{x_2}{D_{12}}+\frac{x_3}{D_{13}}+\frac{x_4}{D_{14}}\quad\text{and}\quad C_1=\frac{P}{RT}\nabla x_1+\frac{x_1}{RT}\left(1+\frac{B_0P}{\mu D_{1,k}}\right)\nabla P$$

A-4a

$$A_{22}=\frac{1}{D_{2,k}}+\frac{x_1}{D_{21}}+\frac{x_3}{D_{23}}+\frac{x_4}{D_{24}}\quad\text{and}\quad C_2=\frac{P}{RT}\nabla x_2+\frac{x_2}{RT}\left(1+\frac{B_0P}{\mu D_{2,k}}\right)\nabla P$$

A-4b

$$A_{33}=\frac{1}{D_{3,k}}+\frac{x_1}{D_{31}}+\frac{x_2}{D_{32}}+\frac{x_4}{D_{34}}\quad\text{and}\quad C_3=\frac{P}{RT}\nabla x_3+\frac{x_3}{RT}\left(1+\frac{B_0P}{\mu D_{3,k}}\right)\nabla P$$

A-4c

$$A_{44}=\frac{1}{D_{4,k}}+\frac{x_1}{D_{41}}+\frac{x_2}{D_{42}}+\frac{x_3}{D_{43}}\quad\text{and}\quad C_4=\frac{P}{RT}\nabla x_4+\frac{x_4}{RT}\left(1+\frac{B_0P}{\mu D_{4,k}}\right)\nabla P$$

A-4d

And

$$B_{ij} = \frac{N_i}{D_{ij}} \qquad \text{A-5}$$

Therefore, the above equations can be simplified as:

$$\begin{aligned}
-N_1A_{11} + (B_{12}N_2 + B_{13}N_3 + B_{14}N_4) &= C_1 \\
-N_2A_{22} + (B_{21}N_1 + B_{23}N_3 + B_{24}N_4) &= C_2 \\
-N_3A_{33} + (B_{31}N_1 + B_{32}N_2 + B_{34}N_4) &= C_3 \\
-N_4A_{44} + (B_{41}N_1 + B_{42}N_2 + B_{43}N_1) &= C_4
\end{aligned} \qquad \text{A-6}$$

Writing equations in matrix form (AN=C) yields

$$\begin{bmatrix} -A_{11} & B_{12} & B_{13} & B_{14} \\ B_{21} & -A_{22} & B_{23} & B_{24} \\ B_{31} & B_{32} & -A_{33} & B_{34} \\ B_{41} & B_{42} & B_{34} & -A_{44} \end{bmatrix} \begin{bmatrix} N_1 \\ N_2 \\ N_3 \\ N_4 \end{bmatrix} = \begin{bmatrix} C_1 \\ C_2 \\ C_3 \\ C_4 \end{bmatrix} \qquad \text{A-7}$$

This may then be solved via matrix inversion for explicit equations describing the molar fluxes:

$$\begin{bmatrix} N_1 \\ N_2 \\ N_3 \\ N_4 \end{bmatrix} = \begin{bmatrix} H_{11} & H_{12} & H_{13} & H_{14} \\ H_{21} & H_{22} & H_{23} & H_{24} \\ H_{31} & H_{32} & H_{33} & H_{34} \\ H_{41} & H_{42} & H_{34} & H_{44} \end{bmatrix} \begin{bmatrix} C_1 \\ C_2 \\ C_3 \\ C_4 \end{bmatrix} \qquad \text{A-8}$$

where $H = \begin{bmatrix} -A_{11} & B_{12} & B_{13} & B_{14} \\ B_{21} & -A_{22} & B_{23} & B_{24} \\ B_{31} & B_{32} & -A_{33} & B_{34} \\ B_{41} & B_{42} & B_{34} & -A_{44} \end{bmatrix}^{-1}$

This may be solved symbolically using MATLAB via the following commands:

```
//
syms A11 B12 B13 B14 B21 A22 B23 B24 B31 B32 A33 B34 B41 B42 B43 A44
A = [A11,B12,B13,B14;B21,A22,B23,B24;B31,B32,A33,B34;B41,B42,B43,A44]
H=inv(A)
//
```

This yields analytical expressions in terms of variables A_{ij}, B_{ij}, C_{ij} which may be directly programmed into COMSOL Multiphysics for a numerical solution via finite elements. For example, position [1,1] of the inverse matrix will be:

H(1,1)=(A22*A33*A44-A22*B34*B43-A33*B24*B42-A44*B23*B32+B23*B34*B42 +B24*B32*B43)/(A11*A22*A33*A44-A11*A22*B34*B43-A11*A33*B24*B42 - A11*A44*B23*B32 - A22*A33*B14*B41 - A22*A44*B13*B31 - A33*A44*B12*B21 +A11*B23*B34*B42+A11*B24*B32*B43+A22*B13*B34*B41 + A22*B14*B31*B43 +A33*B12*B24*B41+A33*B14*B21*B42+A44*B12*B23*B31 + A44*B13*B21*B32 +B12*B21*B34*B43- B12*B23*B34*B41 - B12*B24*B31*B43 - B13*B21*B34*B42 +B13*B24*B31*B42- B13*B24*B32*B41 - B14*B21*B32*B43 - B14*B23*B31*B42 + B14*B23*B32*B41)

Once every position of the H matrix is solved, the flux N_i can be calculated as:

$$N_1 = H_{11}C_1 + H_{12}C_2 + H_{13}C_3 + H_{14}C_4$$

References:

[1] Thiele, E.W., Relation between Catalytic Activity and Size of Particle. Industrial & Engineering Chemistry, 1939. 31(7): p. 916-920.

[2] Aris, R., *Communication. Normalization for the Thiele Modulus.* Industrial & Engineering Chemistry Fundamentals, 1965. **4**(2): p. 227-229.
[3] Jackson, R., *Transport in porous catalysts*. 1977: Elsevier Scientific Publishing Company The Netherlands.

APPENDIX B

B.1 PERMEABILITY DATA OF PEO/PMAA LBL ASSEMBLIES

Gas permeability coefficients of CO_2 and N_2 were measured using the constant-volume, variable-pressure apparatus. The reported gas permeability is the average of three measurements. CO_2/N_2 Selectivity was calculated as the ratio of pure gas permeabilities. Table B.1 present the average gas permeabilities and their standard deviations (δ). Error propagation equation (B.2) was used to determine the uncertainty in the calculated selectivity values.

$$\alpha_{CO_2/N_2} = \frac{P_{CO_2}}{P_{N_2}} \tag{B.1}$$

$$\delta\alpha_{CO_2/N_2} = \alpha_{CO_2/N_2}\sqrt{\left(\frac{\delta P_{CO_2}}{P_{CO_2}}\right)^2 + \left(\frac{\delta P_{N_2}}{P_{N_2}}\right)^2} \tag{B.2}$$

Table B.1. Carbon dioxide and nitrogen permeabilities and selectivity values.

Number of BLs	PEO MW	pH	CO_2 Permeability		N_2 Permeability		CO_2/N_2 Selectivity	Error
			Average	St. Dev.	Average	St. Dev.		
4	400k	2	1.55E-03	1.91E-04	3.73E-05	4.17E-06	41.6	6.9
6	400k	2	3.58E-03	3.29E-04	4.48E-05	3.21E-06	79.9	9.3
8	400k	2	7.19E-03	6.73E-04	5.08E-05	4.57E-06	141.5	18.4
10	400k	2	1.10E-02	9.33E-04	8.10E-05	6.19E-06	135.8	15.5
10	400k	2.5	1.08E-02	8.64E-04	1.27E-04	9.17E-06	85.0	9.2
10	400k	3	1.11E-02	1.05E-03	2.31E-04	2.68E-05	48.3	7.2
10	10k	2	4.48E-03	5.36E-04	1.22E-04	1.31E-05	36.7	5.9
10	100k	2	1.82E-02	2.04E-03	3.43E-04	3.47E-05	53.0	8.0

BLs: Bilayers

MW: Molecular Weight

St. Dev.: Standard Deviation